FEMTOSECOND LASER-INDUCED BREAKDOWN OF MONOLAYER MOLYBDENUM DISULFIDE

by

Joel M. Solomon

A dissertation submitted to the faculty of
The University of North Carolina at Charlotte
in partial fulfillment of the requirements
for the degree of Doctor of Philosophy in
Optical Science and Engineering

Charlotte

2022

Approved by:

Dr. Tsing-Hua Her

Dr. HaiTao Zhang

Dr. Tino Hofmann

Dr. Yong Zhang

ABSTRACT

JOEL M. SOLOMON. Femtosecond laser-induced breakdown of monolayer molybdenum disulfide. (Under the direction of DR. TSING-HUA HER)

Two-dimensional materials such as graphene and transition metal dichalcogenides (TMDs) have been extensively studied due to their extraordinary electronic and optoelectronic properties. In particular, monolayer semiconductor TMDs such as MoS_2, WS_2, and $MoSe_2$ are of great interest due their direct band gap and strong excitonic resonances. Due to its reduced dimensionality, MoS_2 exhibits many strong optical nonlinearities including high harmonic generation and giant multiphoton absorption, making it an excellent candidate for attosecond photonics, mode locking, optical limiting, and multi-photon detectors. Given the multitude of applications, understanding the optical limitations of MoS_2 under intense excitation is essential to optimize its performance. Accordingly, we investigate the femtosecond laser induced breakdown of monolayer MoS_2 with a variety of techniques. In this study, the substrate is discovered to have a profound effect where the ablation threshold itself can vary by more than one order of magnitude due to a simple interference phenomenon within the monolayer. Via substrate engineering, the ablation threshold can be reduced such that laser patterning using pulse energies less than 100 pJ is possible. Similar to many other optical nonlinearities, absorption measurements and theoretical modeling reveal that avalanche ionization is also enhanced where more than 75% of the generated free carriers at breakdown are due to avalanche ionization. Finally, multi-shot studies demonstrate that MoS_2 is one of the most optically robust materials with very weak incubation effects. Notably, the onset of optical damage results in the formation of nano-voids where clusters of atoms are removed while the overall integrity of the monolayer remains intact. These nano-voids are found to strongly influence the optical properties of the MoS_2 monolayer due to the presence of mid-gap states introduced by dangling bonds. The study shows that these nano-voids only form for fluences within 80% of the ablation threshold. All of these findings help establish MoS_2 as a promising candidate for strong field devices and provides foundational knowledge regarding the strong field physics of two-dimensional materials.

ACKNOWLEDGEMENTS

Throughout my academic career, I have been fortunate to be surrounded by great people who have provided an immense amount of support and assistance. Firstly, I would to thank my advisor Dr. Tsing-Hua Her for his support and input in designing experiments and drafting papers. The time I have spent in your lab has driven me to be a better researcher and academic. Likewise, I would like to thank my committee members, Dr. HaiTao Zhang, Dr. Tino Hofmann, and Dr. Yong Zhang, for their insightful questions and feedback. I would also like to recognize our collaborators from NCTU and NTHU in Taiwan for their feedback and support. Specifically, I would like to acknowledge Dr. Li-Syuan Lu for diligently preparing and characterizing all the materials used in this study.

Secondly, I would like to extend my sincere thanks to Dr. Angel Flores and my fellow colleagues at AFRL/RDL for supporting me through the SMART Scholarship. The annual summer internships provided invaluable experience and connections to be a successful researcher. Furthermore, I am extremely grateful for the opportunity to perform world class research and look forward to continue to do so in the future.

Moreover, I am very thankful for my fellow lab mates Arpit Dave, Joseph Obeid, and Emmanuel Sarpong for their help in building experimental setups and with data collection. Additionally, I am extremely grateful to have worked alongside my great friend and colleague Sabeeh Irfan Ahmad. Your enthusiasm and charisma made late night experiments not just bearable but enjoyable. For that I am forever indebted to you. I must also thank all of the friends I have made during my time at UNCC. The countless game nights together provided a much-needed reprieve from my graduate studies and will always be treasured.

Furthermore, I would like to extend my deepest appreciation to my parents, Denise and Dan Solomon, and my brother, Danny for their tireless support during my academic pursuit and encouraging my interests in the sciences since the day I was born.

In addition, I would like to thank my cat, Grace Ann, who would not except anything but my best work and pushed me to be a better human. I would also like to thank my bird, Galileo, who was always by my side and critiquing every word in this dissertation.

Finally, and most importantly, I cannot begin to express my deepest gratitude for my wife, Victoria. Without your endless, unwavering support, I would never have been able to push through the darkest times. You are the foundation upon which I have built everything.

TABLE OF CONTENTS

LIST OF TABLES

LIST OF FIGURES

LIST OF ABBREVIATIONS

1PA	One-photon absorption
2D	Two-dimensional
2DM	Two-dimensional material
2PA	Two-photon absorption
AFM	Atomic force microscopy
AI	Avalanche ionization
CB	Conduction band
CVD	Chemical vapor deposition
FCA	Free carrier absorption
FDTD	Finite-difference time-domain
FWHM	Full width at half maximum
HR-TEM	High resolution transmission electron microscopy
IR	Infrared
MPA	Multi-photon absorption
MPI	Multi-photon ionization
NA	Numerical aperture
ODB	Optical dielectric breakdown
OM	Optical microscopy
PI	Photoionization

PL	Photoluminescence
RGB	Red, green, and blue
SEM	Scanning electron microscopy
SH	Second harmonic
SHG	Second harmonic generation
TEM	Transmission electron microscopy
TI	Tunneling ionization
TMD	Transition metal dichalcogenide
TMM	Transfer matrix method
VB	Valence band
ZTA	Zero-thickness approximation
Al_2O_3	Aluminum(III) oxide (a.k.a. alumina or sapphire)
h-BN	hexagonal boron nitride
MoO_3	Molybdenum trioxide
MoS_2	Molybdenum disulfide
$MoSe_2$	Molybdenum diselenide
NH_4OH	Ammonium hydroxide
PMMA	polymethyl methacrylate
SiO_2	Silicon dioxide
WS_2	Tungsten disulfide

WSe_2	Tungsten diselenide
BBO	Barium borate
Ti:S	titanium:sapphire

CHAPTER 1: INTRODUCTION

Two-dimensional (2D) materials are a class of materials that consist of a single atomic layer and possess extraordinary physical and chemical properties due to effects of quantum confinement. These materials often occur naturally, consisting of layered structures with graphene as the most famous example. Since the first demonstration of mechanical exfoliation and graphene-based field effect transistor in 2004 [1], research has expanded to include a multitude of 2D materials. Graphene has led this research where it has been applied in electronics, optics, and chemistry. Despite the promising results, graphene-based devices are often limited by the semi-metallic nature of graphene. Since graphene is a zero band gap material, there is a need of non-zero band gap 2D materials to push the future of nanoelectronics. This need led to the research of transition metal dichalcogenides (TMDs) with molybedenum disulfide (MoS_2) being one of the most popular materials.

To promote the development and production of nanoelectronics, lasers provide a chemical free route to modify, manipulate, or pattern 2D materials for device fabrication. Much research has already been performed regarding this application for graphene, but little has been investigated for TMDs. The scope of this dissertation is to investigate the ultrafast ablation of MoS_2 and to fill the knowledge gap between the ablation of graphene and TMDs. Additionally, 2D materials in general offer a unique opportunity to study the effects of reduced dimensionality on strong field physics. In the following sections, the importance of TMDs and ultrafast ablation will be reviewed and summarized in order to better understand the motivation of the studies presented here. Finally, the objectives and scope of this dissertation will be outlined.

1.1 Transition Metal Dichalcogenides

Transition metal dichalcogenides or TMDs is a group of 2D materials that possess the generalized chemical formula MX_2 where M is a transition metal and X is a chalcogen, i.e., S, Se, and Te. Many of these TMDs form layered structures with individual layer thicknesses of about 0.65 nm. An individual monolayer consists of hexagonal plane of transition metal atoms sandwiched between two hexagonal planes of chalcogen atoms. The bonds between the transition metal and chalcogen atoms are generally covalent in nature whereas individual layers are bound together by weak van der Waals forces. In their bulk form, they follow one of three polytypes or stacking structures: hexagonal (2H), rhombohedral (3R), or trigonal (1T) [2, 3]. The polytype strongly determines the physical properties of the TMD which can range from insulators, semiconductors, metals, and even superconductors. The TMDs that form layered structures are highlighted in Figure 1.1.

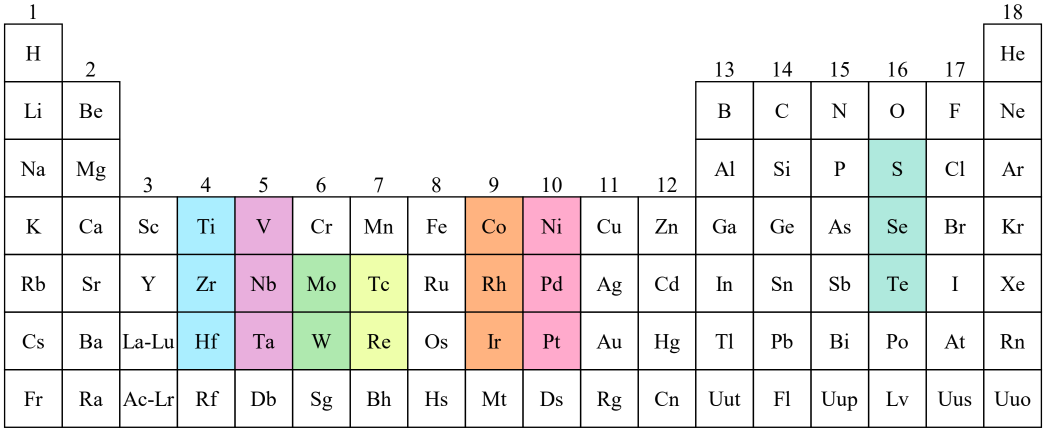

Figure 1.1: Periodic Table of Elements. The highlighted elements show which TMDs can form layered structures.

In particular, semiconducting TMDs such as $MoSe_2$, MoS_2, and WS_2 are of great interest due to their transitions from indirect to direct band gap in their monolayer form. For example, bulk 2H-MoS_2 has an indirect band gap of 1.2 eV; however, as the number layers is reduced to a monolayer, the optical band gap increases to about 1.8 eV and transitions from indirect to direct [2–4]. This transition occurs because of reduced dielectric screening and strong quantum confinement in the monolayer limit, resulting in the formation of excitons that are stable at room temperature and have large binding energies that are greater than 0.5 eV. This transition is also accompanied by a strong increase in photoluminescence (PL), which makes these materials promising candidates for optoelectronic applications.

Monolayer semiconducting TMDs exhibit many novel properties. MoS_2 has high field mobilities that are comparable to graphene, but with low turn-on voltages and high on/off ratios reaching up to 10^8 which are ideal for transistor applications [2, 5]. They also demonstrate great mechanical stability where MoS_2 has a Young's modulus of 270 GPa which is larger than that of stainless steel (205 GPa) [6]. Additionally, the breaking strength of MoS_2 is about 10% of its Young's modulus which is more than an order of magnitude larger compared to steel. Due to their mechanical stability, TMDs have also demonstrated strong reversible photoexcitation that is not sustainable in bulk media. MoS_2 has shown to retain its crystal structure at fluences up to 70% of its ablation threshold wheres bulk materials will undergo amorphization at these fluences [7–9]. Due to the strong, reversible photoexcitation, TMDs have demonstrated strong nonlinear optical responses in the monolayer limit such as high harmonic generation [10].

2D materials in general, including graphene, h-BN, and TMDs, have been studied since the 1960s where they were first used as solid lubricants for applications in tribology [4, 11]. These materials though have only been recently studied as atomically thin materials for electronic and optoelectronic applications due to the mechanical exfoliation of graphene in 2004 [1]. For these materials to be promising candidates for future nanoelectronics, reliable methods of producing high-quality monolayer films needed to be developed. Few-layer and monolayer TMD flakes can be cleaved and transferred from bulk crystals by using scotch tape due to the weak van der Waals forces binding the individual layers together. This technique is referred to as mechanical exfoliation and generally produces the best quality monolayer samples but is not scalable due to lack of control on flakes thickness and size [2, 3]. Liquid exfoliation can be used for production of large quantities of monolayer films. This technique consists of submerging a bulk crystal in an ionic solution for an extended time. Once the ions intercalate between the crystal layers, the bulk crystal is exposed to water which results in a volatile reaction that separates the individual layers. For some 2D materials such as graphene, liquid exfoliation allows for efficient, scalable production of monolayers, but this method does not extend for all materials. For example, the liquid exfoliation of MoS_2 can alter the Mo atom coordination from trigonal prismatic (2H-MoS_2) to octahedral (1T-MoS_2), changing its properties from a semiconductor to a metal [2].

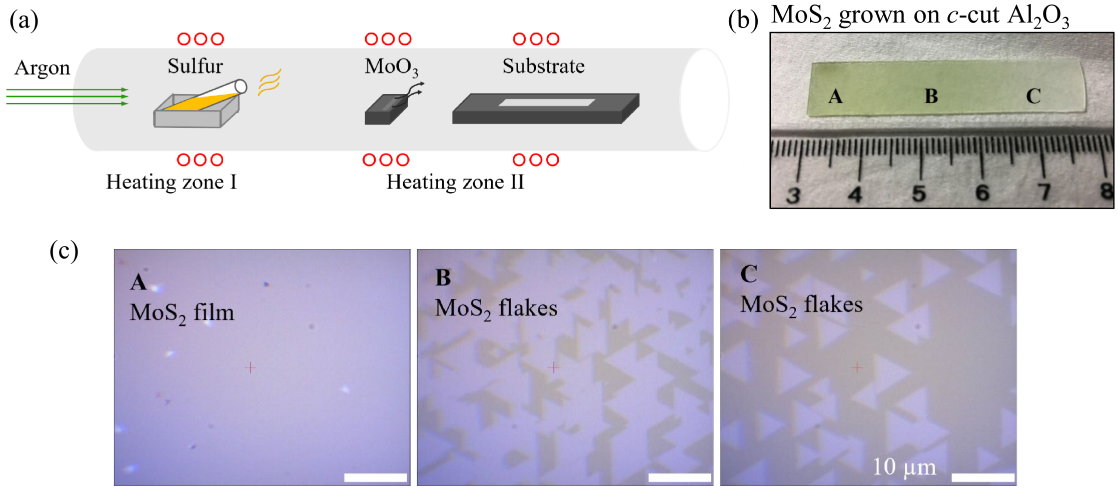

Figure 1.2: (a) Schematic for the CVD growth of MoS_2. (b) Image of monolayer MoS_2 grown on *c*-cut Al_2O_3. (c) Optical images showing change in MoS_2 density from a continuous film in A to single crystal flakes in C. The images A, B and C correspond to the points A, B, and C in (b).

Chemical vapor deposition (CVD) offers a bottom-up approach to growing both monolayer flakes and films on large scales. Figure 1.2a illustrates the CVD growth process of MoS_2. Sulfur and MoO_3 powder are used as precursors which are heated in ceramic boats in a hot-wall CVD chamber. Under an argon flow, the sulfur vapor is carried from heating zone I to heating zone II where it reduces the MoO_3 vapors, forming a MoO_{3-x} suboxide. The suboxide is deposited on the *c*-cut sapphire (Al_2O_3) substrate where it further reacts with the sulfur gas to grow monolayer MoS_2 flakes [12–14]. The density of the flakes is determined based on the substrates position in the chamber. The end of the substrate closest to the sulfur and MoO_3 powder yields the highest density growth, resulting in a continuous monolayer MoS_2 film. The edge of the substrate furthest from the reactants gives single crystal, monolayer flakes. Figure 1.2b shows an example of MoS_2 grown on Al_2O_3 where the point A was closest to the reactants. Optical microscope images of the points A, B, and C are shown in Figure 1.2c, highlighting the difference in density from that of a continuous film to individual flakes. Single crystal flakes can vary in size with side lengths ranging from 5 μm to 100 μm. The size of the flake can be tuned based on the growth conditions. Other TMDs such as $MoSe_2$ and WS_2 follow a similar growth process.

Using *c*-cut Al_2O_3 is important to obtained what is known as highly-oriented MoS_2. Unlike CVD grown graphene or h-BN, a CVD grown MoS_2 film is not a single crystal. It consists of multiple crystals growing into each other which results in local variation in crystal orientation. When MoS_2 is grown on *c*-cut Al_2O_3, the MoS_2 crystal domains preferentially grow along those of the Al_2O_3 substrate. As a result, MoS_2 grows at 0° and 60° orientations on *c*-cut Al_2O_3 which are rotationally equivalent. If MoS_2 was grown on an SiO_2/Si substrate, the MoS_2 crystals will grow in random orientations due to the amorphous nature of the SiO_2 film [15, 16].

There are only a couple limitations of CVD. Currently, CVD growth of TMDs is limited in cases where monolayers are desired. Conditions can easily be controlled to ensure monolayer growth, but controlled growth of multi-layer films has yet to be realized. Additionally, MoS_2 is the only TMD that has been successfully grown as a highly-oriented, continuous film. Other TMDs such as $MoSe_2$ and WS_2 are grown as single crystal flakes. CVD growth of 2D materials may be limited to a single or couple of substrates. To overcome this limitation, techniques to transfer monolayer flakes and films to any number of substrates have been developed. One such technique uses polymethyl methacrylate (PMMA). For example, CVD grown MoS_2 films on Al_2O_3 are often covered or coated with a layer of PMMA. The PMMA coated MoS_2 is then submerged in a NH_4OH solution heated up to 100 °C for 20 minutes which allows the PMMA-MoS_2 composite to be removed from the Al_2O_3 substrate and transferred to another substrate. Once transferred, the PMMA layer is then dissolved with acetone and cleaned with isopropanol, leaving behind the MoS_2 on the new substrate [14].

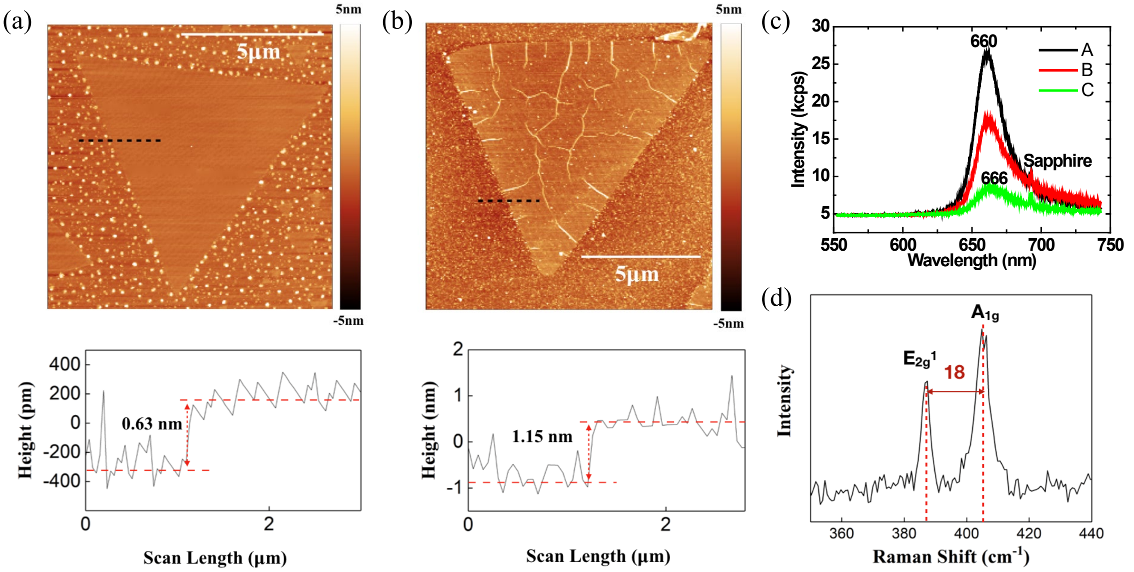

Figure 1.3: (a) AFM scan of as-grown MoS_2 on Al_2O_3. (b) AFM scan of transferred MoS_2 on Al_2O_3. (c) Photoluminescence spectra of as-grown MoS_2 on Al_2O_3. The lines A, B, and C correspond to the image in Figure 1.2b. (d) Raman spectra of as-grown MoS_2 on Al_2O_3.

For the work considered in this dissertation, all TMDs are CVD grown and then transferred following the procedures listed above. Additionally, TMDs are characterized by Raman spectroscopy, PL spectroscopy, and atomic force microscopy (AFM) to ensure monolayer growth with examples shown for MoS_2 in Figure 1.3. The term "as-grown" is used to refer to TMDs that were CVD grown on their current substrate (e.g., Al_2O_3) and have not been transferred. Conversely, "transferred" refers to TMDs that were CVD grown on Al_2O_3 and subsequently transferred to a new substrate. From Figure 1.3a, AFM easily confirms the pristine MoS_2 flake is a monolayer where a step height of 0.63 nm is measured. Due to the transfer process, monolayer flakes can be damaged, developing cracks and wrinkles as shown in Figure 1.3b. In extreme cases, parts of the flake can be completely destroyed, resulting in large holes which may leave the flakes unusable for experiments. Since many semiconductor TMDs have a direct band gap in their monolayer form, they have strong PL signatures which can also be used to confirm the presence of monolayers. The number of layers can also be measured using Raman spectroscopy. The Raman spectra of MoS_2 is characterized by two peaks labeled as E^1_{2g} and A_{1g} in Figure 1.3d, which represent the in-plane and out-of-plane vibrational modes of the S atoms, respectively. The frequency spacing for these modes is about 18 cm^{-1} for monolayer MoS_2. As the number of layers increase, the frequency separation also increases up to 25 cm^{-1} for bulk MoS_2 [17, 18].

1.2 Femtosecond Laser Ablation

Since the invention of the first laser in 1960, researchers have using lasers to control, modify, and ablate materials. As early as 1963, researchers were using lasers to treat tumors [19, 20]. In 1965, the deposition of thin films through laser controlled vaporization was demonstrated [21]. Shortly after, the first picosecond laser was built in 1966, with the first femtosecond laser being developed in 1981 [22, 23]. Since then, femtosecond lasers have been used to study laser-induced material modification and ablation. Due to the high electric field strengths obtainable with femtosecond pulses, nonlinear ionization mechanisms could now be probed in transparent materials. This section serves as brief introduction for the ionization mechanisms that are prevalent in femtosecond ablation and outlines how these ionization rates may be estimated.

1.2.1 Ionization Mechanisms

Femtosecond laser ablation is also commonly referred to as ultrashort or ultrafast laser ablation. All three terms refer to the same process which is the removal of material with optical pulses with pulse durations of a few hundred femtoseconds or less. Studying femtosecond ablation is important for a number of reasons. For practical purposes, femtosecond ablation has shown to have better controllability and precision for micromachining and nanopatterning. From a theoretical perspective, femtosecond ablation offers an opportunity to investigate light-matter interaction in the strong field regime where thermodynamic and electrical responses can easily be separated due to the timescale of the excitation process.

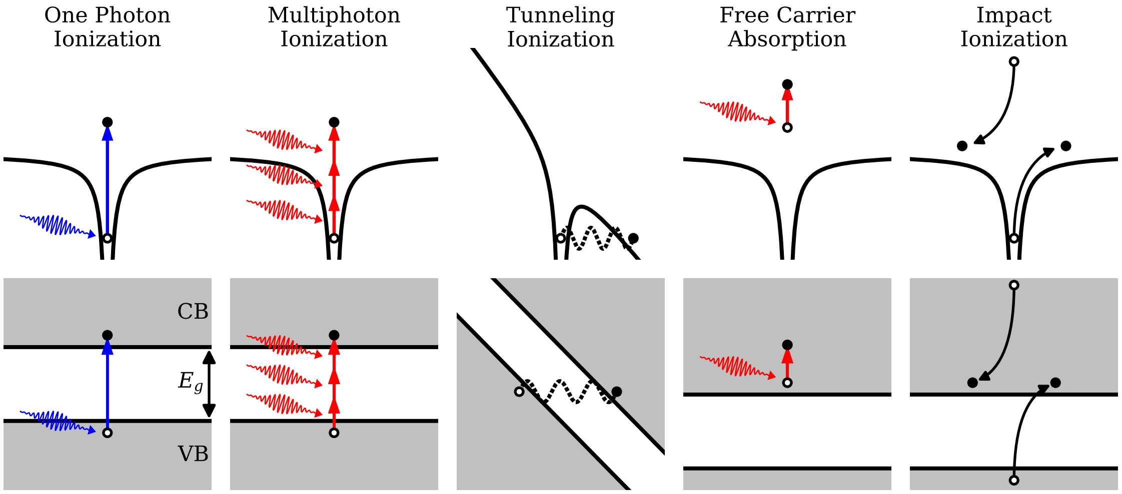

Figure 1.4: Photoionization mechanisms for atoms (top row) and for semiconductors and insulators (bottom row).

For laser ablation to occur, optical energy must be deposited in the material. For opaque materials, the energy of a photon of visible light is sufficient to excite an electron through one-photon absorption (1PA); however, many materials, such as dielectrics and some semiconductors, are transparent in the visible and near infrared (IR) part of the spectrum. Optical ablation for these materials requires high electric field strengths to induce nonlinear excitation or photoionization (PI) to deposit energy into the material.

Figure 1.4 illustrates possible PI mechanisms for both atoms and solids. Multi-photon absorption (MPA) or multi-photon ionization (MPI) requires the simultaneous absorption of multiple photons to excite an electronic transition. For MPI, an electron must absorb enough photons such that total absorbed photon energy is greater than or equal to ionization potential or band gap. For tunneling ionization (TI), the presence of the high electric field strength is enough to suppress, screen, or skew the Coulomb potential binding the electron to the atom or valence band (VB). If electric field is strong enough, the Coulomb potential can be skewed enough to allow the electron to tunnel through the barrier and become a free electron.

Once a free electron has been created, other absorption or ionization mechanisms can take place. The first one is free carrier absorption (FCA), which is a specific case of 1PA. For solids, a free electron in the conduction band (CB) can absorb a single photon and be excited further up into the CB. This process is also known as inverse bremsstrahlung. If a free carrier is excited sufficiently high in the CB, it can collide with a bound electron in the VB. The free electron imparts some of its energy to the bound electron where it falls to the base of the CB and the bound electron is excited to the base of the CB. This process further ionizes the atom, leaving two free electrons in the CB. This mechanism is the opposite of Auger recombination and is known as impact ionization. Given a number of initial free electrons in an optical field, a FCA and impact ionization can occur simultaneously and feed into each other. This runaway process is known as avalanche ionization (AI) and can potentially generate large numbers of free carriers.

1.2.2 Keldysh's Theory for Ionization of Solids

One of the first steps to understanding the ablation dynamics or the optical dielectric breakdown (ODB) of a material is identifying and quantifying which ionization mechanisms are dominate. There are generally two approaches in predicting the strength of MPI or TI: perturbative or nonperturbative. The perturbative approach uses time-dependent perturbation theory to describe the probability of MPI or TI in a crystalline solid and was originally developed by Göppert-Mayer in 1931 [24]. For the specific case of two-photon absorption (2PA), the electronic transition from the VB, v, to the CB, c, can be expressed as

$$W_{2PA} = \frac{2\pi}{\hbar} \int \left| \sum_i \frac{\langle \Psi_c | H | \Psi_i \rangle \langle \Psi_i | H | \Psi_v \rangle}{(E_i - E_v - \hbar\omega)} \right|^2 \delta \left[E_c(\mathbf{k}) - E_v(\mathbf{k}) - 2\hbar\omega \right] \frac{\mathrm{d}^3\mathbf{k}}{(2\pi)^3} \tag{1.1}$$

where W_{2PA} is the 2PA transition probability rate per unit volume and Ψ_i are the Bloch wave functions describing electrons in the i^{th} band with energy E_i. The delta function describes the energy convservation requirements. The integration covers the first Brillouin zone in $\mathbf{k}$ space and H is the interaction Hamiltonian [25]. Equation (1.1) is simple to comprehend. The transition probabilities from all states are summed and integrated over all space in the crystal to determine the probability of a transition. The difficulty in evaluating this expression arises from the fact that all of the possible states and their transitions and interactions need to be well documented in order to obtain an accurate evaluation of W_{2PA}.

The other nonpertubative approach was originally developed in 1965 by L. V. Keldysh [26]. He developed a set of expressions to describe MPI and TI for nonresonant excitation for both atoms and solids. By describing the electron states with modified Houston functions in a simple harmonic electric field ($\boldsymbol{\mathcal{E}}(t) = \boldsymbol{\mathcal{E}}_0 \cos(\omega t)$), Keldysh derived a general formula describing the ionization rate W_{PI} of a solid which is given by

$$W_{PI} = \frac{2\pi}{\hbar} \int \frac{\mathrm{d}\mathbf{p}}{(2\pi\hbar)^3} |\mathcal{L}_{cv}(\mathbf{p})|^2 \sum_i \delta(\overline{E_{cv}(\mathbf{p})} - i\hbar\omega). \tag{1.2}$$

$E_{cv}(\mathbf{p})$ represents the energy gap between an initial state in the valence band to a final state in the conduction band, and $\overline{E_{cv}(\mathbf{p})}$ represents the cycle-average energy of the transition expressed by

$$\overline{E_{cv}(\mathbf{p})} = \frac{1}{2\pi} \int_{-\pi}^{\pi} E_{cv} \left(\mathbf{p} + \frac{e\boldsymbol{\mathcal{E}}_0}{\omega} \sin(x) \right) \, \mathrm{d}x, \tag{1.3}$$

where $x = \omega t$. $\mathcal{L}_{cv}(\mathbf{p})$ is a matrix element that describes the strength of the amplitude and is often referred as the ionization amplitude where

$$\mathcal{L}_{cv}(\mathbf{p}) = \frac{1}{2\pi} \oint \mathcal{V}_{cv} \left(\mathbf{p} + \frac{e\boldsymbol{\mathcal{E}}_0}{\omega} u \right) e^{jS(u)} \, \mathrm{d}u, \tag{1.4}$$

$u = \sin(\omega t)$, $\mathcal{V}_{cv}(\mathbf{p}) = j\hbar \int u_{\mathbf{p}}^{c*}(\mathbf{r}) e\boldsymbol{\mathcal{E}}_0 \nabla_{\mathbf{p}} u_{\mathbf{p}}^{v}(\mathbf{r}) \, \mathrm{d}\mathbf{r}$ is the optical matrix element, and $u_{\mathbf{p}}^{c,v}$ are periodic functions describing the lattice. $S(u)$ is the classical action given by

$$S(u) = \frac{1}{\hbar\omega} \int_0^u E_{cv} \left(\left| \mathbf{p} + \frac{e\boldsymbol{\mathcal{E}}_0}{\omega} v \right| \right) \frac{\mathrm{d}v}{\sqrt{1 - v^2}} \tag{1.5}$$

with $v = \sin(\omega t)$. To evaluate Equation (1.2), knowledge of the band structure is needed much like in the perturbative case. Fortunately, analytical solutions can be obtained when simple two-band models are used. The two most commonly used band structures are a parabolic model and Kane's model [27]. Occasionally, a cosine band structure model has also been used [28–30]. The equations for the models are listed below:

$$\text{parabolic}: \qquad E_{cv}(\mathbf{p}) = E_g + \frac{p^2}{2m_r}, \tag{1.6}$$

$$\text{Kane}: \qquad E_{cv}(\mathbf{p}) = E_g \sqrt{1 + \frac{p^2}{m_r E_g}}, \tag{1.7}$$

$$\text{cosine}: \qquad E_{cv}(\mathbf{p}) = E_g + \frac{\hbar^2}{m_r d^2} - \frac{\hbar^2}{m_r d^2} \cos^3\left(\frac{pd}{\hbar}\right), \tag{1.8}$$

where d is the lattice constant and m_r is the reduced mass. The reduced mass is given by

$$\frac{1}{m_r} = \frac{1}{|m_{cb}|} + \frac{1}{|m_{vb}|} \tag{1.9}$$

where m_{cb} and m_{vb} are the effective masses of an electron in the CB and a hole in the VB, respectively. The above expressions for the energy structure have been simplified for the case of isotropic crystals.

Using Kane's model from Equation (1.7), the ionization rate W_{PI} from Equation (1.2) becomes

$$W_{PI} = \frac{2\omega}{9\pi}\left(\frac{m_r\omega}{\hbar\gamma\gamma_f}\right)^{3/2} Q\left(\gamma, \frac{\tilde{\Delta}}{\hbar\omega}\right) \exp\left\{-\pi\left\lfloor\frac{\tilde{\Delta}}{\hbar\omega}+1\right\rfloor\frac{\mathcal{K}_\gamma-\mathcal{E}_\gamma}{\mathcal{E}_1}\right\} \tag{1.10}$$

where $\lfloor x \rfloor$ is the floor operator in which only the integer part of x is used. The function $Q(\gamma, \tilde{\Delta}/\hbar\omega)$ is defined as

$$Q(\gamma, x) = \sqrt{\frac{\pi}{2\mathcal{K}_\gamma}}\sum_{\ell=0}^{\infty}\exp\left\{-\pi\ell\frac{\mathcal{K}_\gamma-\mathcal{E}_\gamma}{\mathcal{E}_1}\right\}\Phi\left(\sqrt{\frac{\pi^2\left(2\lfloor x+1\rfloor-2x+\ell\right)}{2\mathcal{K}_1\mathcal{E}_1}}\right) \tag{1.11}$$

where Φ is the Dawson integral. Much of the notation used above has been adopted from [31] where

$$\begin{aligned} \gamma_f &= \frac{1}{\sqrt{1+\gamma^2}}, \\ \mathcal{K}_1 &= \mathcal{K}(\gamma_f), \qquad \mathcal{K}_\gamma = \mathcal{K}(\gamma\gamma_f), \\ \mathcal{E}_1 &= \mathcal{E}(\gamma_f), \qquad \mathcal{E}_\gamma = \mathcal{E}(\gamma\gamma_f), \end{aligned} \tag{1.12}$$

where $\mathcal{K}(x)$ and $\mathcal{E}(x)$ are the complete elliptic integrals of the first and second kind, respectively. Using the same notation, the effective band gap $\tilde{\Delta}$ can be written as

$$\tilde{\Delta} = \frac{2\mathcal{E}_1}{\pi\gamma\gamma_f}E_g. \tag{1.13}$$

This quantity is the energy that an electron needs in order to be excited from the valance band to the conduction band. An electron in an optical field will oscillate with the incident electric field, changing the energy of the electron. This oscillating energy is known as the quiver energy. The cycle-average of the quiver energy is known as the ponderomotive energy.

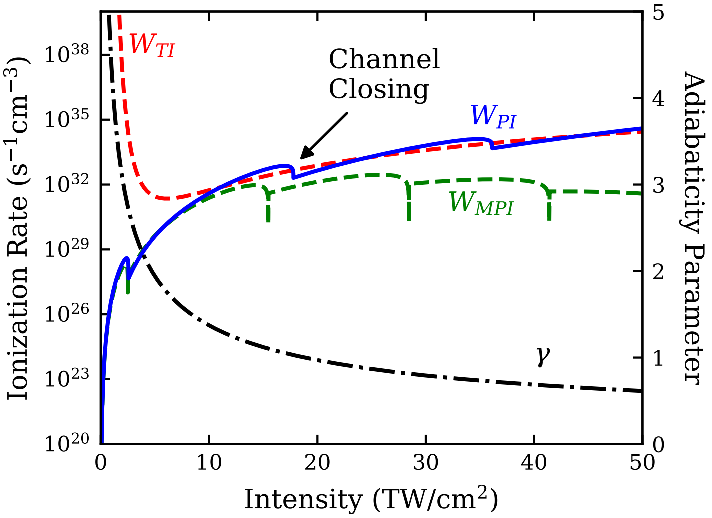

Figure 1.5: Calculated photoionization rates based on the Keldysh equations for SiO_2 ($E_g = 9\,\text{eV}$, $m_r = 0.5m_e$) excited at 800 nm .

The most important parameter for the previous equations is the dimensionless quantity γ, which is known as the adiabaticity parameter. For solids,

$$\gamma = \frac{\omega\sqrt{m_r E_g}}{e\mathcal{E}_0}. \tag{1.14}$$

Besides containing the field strength $\mathcal{E}$, the adiabaticity parameter provides an indicator on the relative strengths of MPI and TI. The ionization rate in Equation (1.10) includes both MPI and TI. There are two limits of interest. For $\gamma \gg 1$, MPI is the dominant mechanism. For $\gamma \ll 1$, TI is the dominant ionization mechanism. In the

MPI limit, Equation (1.10) can be reduced to give

$$W_{MPI} = \frac{2\omega}{9\pi}\left(\frac{m_r\omega}{\hbar}\right)^{3/2}\Phi\left(\sqrt{2\left\lfloor\frac{\tilde{\Delta}}{\hbar\omega}+1\right\rfloor-\frac{2\tilde{\Delta}}{\hbar\omega}}\right) \times \exp\left\{2\left\lfloor\frac{\tilde{\Delta}}{\hbar\omega}+1\right\rfloor\left(1-\frac{1}{4\gamma^2}\right)\left(\frac{1}{16\gamma^2}\right)^{\left\lfloor\tilde{\Delta}/\hbar\omega+1\right\rfloor}\right\} \tag{1.15}$$

where the effective band gap $\tilde{\Delta}$ is

$$\tilde{\Delta} = E_g + \frac{e^2\mathcal{E}^2}{4m_r\omega^2}. \tag{1.16}$$

In the MPI limit, one can easily see that the energy necessary for ionization is simply the sum of the intrinsic band gap of the material plus the ponderomotive energy of the electron. In the tunneling limit, Equation (1.10) becomes

$$W_{TI} = \frac{2}{9\pi}\frac{E_g}{\hbar}\left(\frac{m_rE_g}{\hbar^2}\right)^{3/2}\left(\frac{\hbar\omega}{E_g}\frac{1}{\gamma}\right)^{5/2}\exp\left\{-\frac{\pi}{2}\frac{E_g}{\hbar\omega}\gamma\left(1-\frac{1}{8}\gamma^2\right)\right\}. \tag{1.17}$$

Equations (1.10), (1.15), and (1.17) are plotted in Figure 1.5 for SiO_2 excited at 800 nm. The ionization rates are plotted on the left vertical scale while the adiabaticity parameter γ is plotted on the right vertical scale. As mentioned previously, for $\gamma \gg 1$, W_{MPI} matches well with W_{PI} whereas W_{TI} agrees well with W_{PI} for $\gamma \ll 1$. Another important feature to point out is the step-like behavior that is seen for the W_{MPI} and W_{PI} curves. This step is known as channel closing and occurs when the MPA order changes. For example, if SiO_2 ($E_g = 9\,\text{eV}$) is excited by 800 nm ($E = 1.55\,\text{eV}$) light, then absorption can only occur by a six photon absorption process. As the intensity of the light increases, so does the ponderomotive energy of the electrons as well. Given a sufficiently strong optical field, the ponderomotive energy can increase enough to switch the MPA order from six- to seven-photon absorption. This effect gives rise to the channel closing phenomenon.

1.2.3 Avalanche Ionization

Avalanche ionization (AI) refers to the rapid multiplication of free carriers through the combination of FCA followed by impact ionization in the presence of a strong optical field. These two process feed into each hence the term avalanche. In order for AI to generate carriers, seed electrons must first be excited typically through processes such as MPI or TI (Figure 1.6). Avalanche ionization has always been considered when the ultrafast laser ablation of transparent materials is investigated, but the relative importance and strength of AI is still debated to this day.

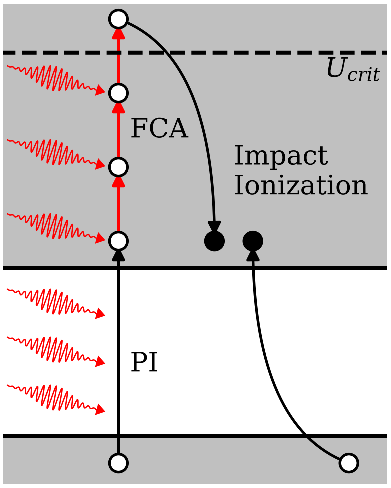

Figure 1.6: Illustration of PI seeding AI for solids. The combination of FCA and impact ionization is AI.

Since AI is still actively researched, there have been multiple models proposed to predict AI rates in materials ranging from semiconductors to insulators [32–39]. Conceptually, one of the simplest models to understand was proposed by Stuart *et al.* where he used a single-rate equation (SRE) of the form

$$\frac{dN}{dt} = W_{PI} + \gamma_{AI} I(t) N(t) \tag{1.18}$$

where N is the free electron population density and γ_{AI} is known as the avalanche coefficient [34, 35]. The second term on the right accounts for both FCA and impact ionization and represents the carriers generated by AI. At its simplest, AI depends on the intensity of the incident pulse and the number of free carriers in the CB. This proportionality is reasonable on the surface. As the intensity increases, FCA should also increase. Additionally, as population density increases, both FCA and impact ionization should increase since more free electrons are available to absorb incident photons or to collide with electrons in the VB.

Though Equation (1.18) is simple and straight forward to understand, it does not directly highlight another important factor for AI. In order for AI to occur, the energy of a free electron must be above a critical energy U_{crit} such that enough energy can be imparted during a collision to excite a bound electron such that both electrons remain in the CB after energy conservation is considered. On the surface, one would expect U_{crit} to simply be $2E_g$ or twice the energy of the band gap; however, the pondoromotive energy of the electron and momentum conservation needs to be considered during the collision. Accounting for these conditions, the critical energy becomes

$$U_{crit} = \left(2 + \frac{m_r}{m_{cb}}\right)\left(E_g + \frac{e^2\mathcal{E}_0^2}{4m_r\omega^2}\right). \tag{1.19}$$

The first term containing m_r/m_{cb} appears due to momentum conservation [40]. The second term which matches Equation (1.16) is the effective band gap which includes the ponderomotive energy. Only free electrons, with energy U_{crit}, can partake in impact ionization.

1.3 Overview and Objectives

2D materials such as graphene, TMDs, and h-BN have been extensively studied due to their extraordinary electronic and optoelectronic properties [2, 41–43]. Specifically, monolayer semiconductor TMDs such as MoS_2, WS_2, $MoSe_2$, and WSe_2 are of particular interest since they exhibit strong excitonic resonances and possess a direct band gap in their monolayer form due to effects of quantum confinement [3, 44]. These semiconducting TMDs have already been utilized for nanoelectronics such as field effect transistors [5, 45, 46], phototransistors [47, 48], LEDs [49, 50], and chemical sensors [51, 52]. Moreover, TMDs have demonstrated strong optical nonlinearities including high harmonic generation [10], saturable absorption [53, 54], and giant multi-photon absorption [55–57] which make them excellent candidates for attosecond photonics, optical limiting, and multi-photon detectors. Many of these TMD-based devices are developed from natural crystals where single atomic layers are extracted through mechanical exfoliation which is time consuming and yields low densities of monolayer films. Conversely, single crystal and large, highly-oriented MoS_2 films can be synthesized through CVD which can then be easily transferred and patterned for rapid device development and manufacturing. Many studies regarding laser patterning and ablation of graphene have been reported for this application but little has been discussed regarding TMDs [58–64].

A few studies have investigated the response of monolayer MoS_2 to intense femtosecond excitation near the ablation threshold but provide little information on the ablation process itself [7, 65]. Paradisanos *et al.* demonstrates that the Raman modes of both bulk and monolayer MoS_2 flakes slowly decrease after multiple exposures to ultrafast pulses. They showed that monolayer flakes were more resistanct to degradation than its bulk counterpart where they believed damage occurred through sublimation, resulting in a decrease in the Mo-S bond density [65]. Pan *et al.* studied the ultrafast ablation of bulk MoS_2 and determined breakdown can either result through sublimation at low fluences or the material can form a superheated liquid at higher fluences [66]. While their results are insightful, the excitation dynamics of bulk and monolayer MoS_2 differ significantly. Therefore, studying and quantifying the ablation process and features of TMDs is important in order to understand how these materials respond to intense excitation and to optimize the laser patterning process.

Moreover, 2D materials provide a unique opportunity to study strong field physics due to their reduced dimensionality. The intense excitation and laser-induced breakdown of bulk metals, semiconductors, and dielectrics have been thoroughly researched where the role of MPI, TI, and AI have been analyzed, discussed, and modeled. Although much of this literature can be utilized, certain effects such as spatial-temporal beam propagation, self-limiting and intensity clamping, self focusing, and longitudinal carrier diffusion, which are important in the ablation of bulk materials, are negligible for 2D materials due to their thinness. Additionally, the quantum confinement effects introduced by the reduced dimensionality can significantly impact the energy coupling, energy distribution, and carrier densities in monolayer TMDs, leading to enhanced or mitigated processes compared to those observed for bulk materials with MPA providing a perfect example.

This research aims to study the dielectric breakdown of TMDs, specifically MoS_2 since it is a promising candidate for future nanoelectronics. Hereto, multiple experiments have been designed and performed to investigate and characterize the ablation of MoS_2 when exposed to ultrafast pulses. This dissertation is broken down into four main chapters. Chapters 2, 3, and 4 are written such that each chapter may stand on its own as a research article with their own introductions and conclusions. Specifically, Chapter 4 is based on my publication in *AIP Advances* [67]. Although, these chapters are ordered in the most logical progression of the research that is presented, one does not have to read Chapters 2, 3, and 4 in sequential order to understand their important messages. Alternately, the content in Chapter 5 depends on the material presented in the previous chapters, requiring the reader to have read the previous content. The body of the dissertation is summarized in the following:

- *Ultrafast Laser Ablation, Intrinsic Threshold, and Nanopatterning of Monolayer Molybdenum Disulfide.* The optical excitation of 2D materials is greatly influenced by strong interference effects due to their dielectric surroundings. This etalon effect is systematically investigated in the context of ultrafast ablation of 2D materials using MoS_2 as an example whose ablation threshold is found to vary by more than one order of magnitude across multiple substrates. Given the atomic thickness of 2D materials, simple analytical expressions are developed that predict the excitation enhancement for arbitrary substrates and are universal for all 2D materials. Using these equations, substrates are designed and fabricated to engineer the ablation threshold of MoS_2 such that ultrafast patterning can be conducted using a low-power oscillator.

- *Femtosecond Laser-Induced Breakdown and The Role of Avalanche Ionization in Molybdenum Disulfide.* Monolayer MoS_2 has demonstrated strong optical nonlinearites such as second harmonic generation, high harmonic generation, saturable absorption, and giant two-photon and three-photon absorption. Given its strong nonlinear absorption, one may expect that multi-photon absorption to dominate carrier generation at optical excitations intense enough to result in ablation; however, research has shown that Auger recombination is enhanced in MoS_2 as well. Since avalanche ionization is the inverse of Auger recombination, the avalanche process may also be enhanced in MoS_2. As such, the femtosecond ablation of MoS_2 is investigated with strong emphasis on the characterization of the ablation features and development of a theoretical model that predicts the carrier dynamics at ablation.

- *Ultrafast Multi-Shot Ablation and Defect Generation in Monolayer Molybdenum*

Disulfide. In practice, ultrafast ablation is generally studied as an intended consequence of laser patterning or an unintended consequence of laser-induced damage to an optical device. In either case, ablation or damage typically results from exposure to several pulses where incubation effects reduce the ablation threshold before material is ultimately removed. Considering incubation, the multi-shot ablation of MoS_2 is studied and compared to a variety of materials. Specifically, the generation of laser-induced defects in MoS_2 is investigated where a separate damage threshold is found that is below the ablation threshold. These defects are found to have a profound effect on the optical properties of MoS_2 [67].

- *Additional Experiments and Challenges.* Experiments that do not directly contribute to the previous chapters above are presented here. Much of the research presented here is still ongoing but their potential contribution may be deserving of its own thesis or dissertation. Thus, only the initial investigations are reported. Additionally, challenges that were encountered are presented as a resource for future experiments.

A number of appendices are also included that help explain or outline many experimental designs or practices that are useful for femtosecond-based experiments in general. Many of these appendices also serve as supporting information for Chapters 2, 3, and 4. The results of all the performed experiments are summarized and presented in Chapter 6. Potential future projects are also outlined and presented to provide additional direction for this work.

CHAPTER 2: ULTRAFAST LASER ABLATION, INTRINSIC THRESHOLD, AND NANOPATTERNING OF MONOLAYER MOLYBDENUM DISULFIDE

2.1 Introduction

Single atomic layer materials such as graphene, transition metal dichalcogenides (TMDs), and hexagonal boron nitride have been studied extensively for their novel electronic and optical properties and for their applications in optoelectronic devices [2, 42]. Graphene exhibits strong wavelength-independent absorption of 2.3% and high carrier mobilities reaching $200{,}000\,\mathrm{cm}^2/\mathrm{V\,s}$ [42, 68]. Semiconducting TMDs such as MoS_2 and WS_2 are of great interest because of their transition from indirect to direct band gap and strong excitonic resonances at room temperature as the number of layers is reduced to a monolayer [3, 44]. Both graphene and MoS_2 have demonstrated phenomenal mechanical robustness [6, 69] and optical stability under intense femtosecond excitation [7, 70]. These properties have led to the research and development of 2D material-based electronic and optoelectronic devices such as transistors [5, 42], photodetectors [12, 42], and additional heterostructure devices [71].

For such device applications, reliable patterning techniques are essential to selectively remove 2D materials for specific sizes and geometries. Although electron beam and photolithography have been used extensively to pattern 2D materials, they suffer from high costs, complexity, vacuum operation requirements, and more importantly are prone to leave behind contaminates or polymer residues, causing damage or unwanted doping which can inadvertently degrade their electrical properties [72–78]. In this regard, laser ablation is a promising technique to pattern 2D materials that is *in situ*, resist-free, and maskless. Specifically, the ultrafast laser ablation and patterning of graphene based on oxidative burning has been demonstrated on several substrates

[79]. Scanning rates as high as tens of mm/s can be achieved with a laser fluence of a couple hundred mJ/cm^2 from laser amplifiers [46]. In addition, sub-diffraction-limited ablated features under 100 nm can be obtained with shaped picosecond laser beams [79]. In contrast, little research has been conducted on the femtosecond ablation of TMDs. Paradisanos *et al.* has studied the multi-shot degradation of exfoliated monolayer and bulk $\mathrm{MoS_2}$ and reported single-shot ablation thresholds based on the appearance of submicron-sized distortion [65]. Pan *et al.* investigated ablation mechanisms of bulk $\mathrm{MoS_2}$ under intense femtosecond excitation, and determined that the ablation was mediated by sublimation at weak pumping and melting at strong pumping [66]. Despite these efforts, a rigorous investigation of the threshold fluence and ultrafast laser patterning of monolayer TMDs has not been demonstrated. We note that continuous-wave 532 nm (CW) lasers have been demonstrated to sublimate monolayer $\mathrm{MoS_2}$ on a $\mathrm{SiO_2/Si}$ substrate with a 200 nm spatial resolution, though the patterning speed is slow due to its photothermal nature [80]. The throughput, however, can be substantially increased using a photothermoplasmonic substrate which then requires transfer of the patterned $\mathrm{MoS_2}$ to other substrates [81].

Since many applications require a supporting substrate, understanding its effect on the laser ablation of 2D materials is important. Although ultrafast laser ablation of graphene has been extensively studied, the role of the substrates is still not clear. The reported ablation thresholds from many studies made by similar pulse widths ($\sim$50$-$100 fs) and wavelengths ($\sim$800 nm) differ by one order of magnitude among suspended graphene and graphene supported by borosilicate glass, $\mathrm{Al_2O_3}$, and 285 nm $\mathrm{SiO_2/Si}$ substrates [46, 58, 60, 82–84]. Surprisingly, such differences have never been discussed or understood. Beyond mechanical support, substrates have been routinely claimed to act as a heat sink to explain why CW laser thinning of multi-layer graphene and $\mathrm{MoS_2}$ self-terminates at monolayers [80, 85]. Other groups also observed that the ablation threshold for both femtosecond and CW excitation are lower for suspended

2D materials than those supported on a SiO_2/Si substrate, which was again attributed to heat dissipation through the supporting substrates [82, 86]. Optically, substrates are known to enhance the light outcoupling of 2D materials through the etalon effect. For SiO_2/Si substrates, the Raman scattering was shown to strongly depend on the SiO_2 thickness for graphene [87], which led to the optimization of both the Raman scattering and photoluminescence of WSe_2 by controlling the SiO_2 layer thickness where the largest enhancement occurred for a SiO_2 thickness of about 90 nm for 532 nm excitation [88]. Similar enhancement for Raman scattering, photoluminescence, and second harmonic generation was obtained by using distributed Bragg reflectors (DBR) as a substrate for MoS_2 [89]. Improved optical contrast of graphene and MoS_2 was achieved by designing multilayer heterostructure substrates where an optical contrast of 430% was obtained for monolayer MoS_2 [90, 91]. We note that the etalon effect has been previously shown to modulate the laser thinning efficiency of multilayer graphene, but has never been studied for laser ablation of 2D materials [85].

In this work, we studied the femtosecond laser ablation of monolayer MoS_2 on a variety of common substrates. Notably, we demonstrated this process is both high speed (∼5 mm/s) and high resolution (∼250 nm with a 0.55 NA objective at 800 nm). Moreover, the influence of substrates on the ablation threshold fluence F_{th} was investigated, both in single-shot and line-scan modes. It was shown that femtosecond laser ablation of transferred monolayer MoS_2 is adiabatic where the heat dissipation through the supporting substrates is negligible, and the variation in F_{th} among substrates can be largely explained by the substrates' etalon effect. Based on our finding, an all-dielectric DBR substrate was realized to reduce F_{th} by 7× compared to that of sapphire to enable laser patterning using low-power femtosecond oscillators.

2.2 Zero-Thickness Approximation

Previous studies on the etalon effect of monolayer 2D materials focused on engineering the Raman scattering, photoluminescence, and second-harmonic generation by optimizing the internal field at the excitation wavelength and the outcoupling efficiency at the emission wavelength [89–91]. As a result, the theoretical enhancement can only be calculated computationally. For ablation, only the excitation enhancement is of concern and we show below that the internal field $\mathcal{E}_{2DM}$ at the excitation wavelength has a simple analytical approximation. The substrates used in this study include sapphire (Al_2O_3), borosilicate glass, 70 nm thick gold (Au) film on a glass substrate, 90 nm SiO_2/Si, and two custom designed DBR substrates: one DBR substrate (DBR800(+)) targets maximal intensity enhancement and the other (DBR800(-)) targets maximal intensity suppression. The system can be modeled as an asymmetric etalon composed of air, a 2D material, and a substrate (Figure A.1). If the effective reflection coefficient between the monolayer and the substrate $\tilde{r}_{1s} = r_0 \exp(i\phi)$ is known, then the spatial distribution of the electric field inside the monolayer $\mathcal{E}_{2DM}(x)$ can be rigorously calculated using the Airy formula (see Equation (A.1)). Since monolayer 2D materials are much thinner compared to the wavelength investigated here, we introduce the zero-thickness approximation (ZTA) to simplify the internal field $\mathcal{E}_{2DM}(x)$ to become

$$\mathcal{E}_{2DM} \approx \mathcal{E}_{2DM}^{ZTA} = \mathcal{E}_{inc}\tilde{t}_{01}\left(\frac{1+\tilde{r}_{1s}}{1-\tilde{r}_{1s}\tilde{r}_{10}}\right), \tag{2.1}$$

where $\mathcal{E}_{inc}$ is the incident electric field and $\tilde{t}_{ij}$ and $\tilde{r}_{ij}$ are Fresnel transmission and reflection coefficients from the i^{th} to j^{th} medium, respectively. For single-material substrates such as Al_2O_3, glass, or a thick Au film, $\tilde{r}_{1s}$ is simply the Fresnel reflection coefficient (see Equation (A.3)), and the internal field $\mathcal{E}_{2DM}$ becomes

$$\mathcal{E}_{2DM}^{ZTA} = \mathcal{E}_{inc}\left(\frac{2}{1+\tilde{n}_s}\right), \tag{2.2}$$

where $\tilde{n}_s$ is the complex refractive index of the substrate. For SiO_2/Si substrates with a silica layer thickness of d_2, $\tilde{r}_{1s}$ can be calculated analytically using an asymmetric etalon composed of a TMD, SiO_2, and Si (see Equation (A.4)), and $\mathcal{E}_{2DM}$ becomes approximately

$$\mathcal{E}_{2DM}^{ZTA} = \mathcal{E}_{inc} \left(\frac{2\left[(\tilde{n}_2 + \tilde{n}_s) - (\tilde{n}_s - \tilde{n}_2) e^{i2\beta_2 d_2} \right]}{(1+\tilde{n}_2)(\tilde{n}_2 + \tilde{n}_s) + (\tilde{n}_2 - 1)(\tilde{n}_s - \tilde{n}_2) e^{i2\beta_2 d_2}} \right), \tag{2.3}$$

where $\beta_2 = 2\pi\tilde{n}_2/\lambda_0$, and $\tilde{n}_2$ and $\tilde{n}_s$ are the refractive indices of SiO_2 and Si, respectively. For DBR substrates, an analytical expression of $\mathcal{E}_{2DM}^{ZTA}$ can be found in Equation (A.12). Details about the DBR design and fabrication can be found in Appendix A (Figure A.2). Equations (2.2)-(2.3) and Equation (A.12) clearly show $\mathcal{E}_{2DM}^{ZTA}$ is independent of the 2D material. In fact, this result can be extended to arbitrary stratified substrates with the proof being presented in Appendix A (see Equation (A.9)).

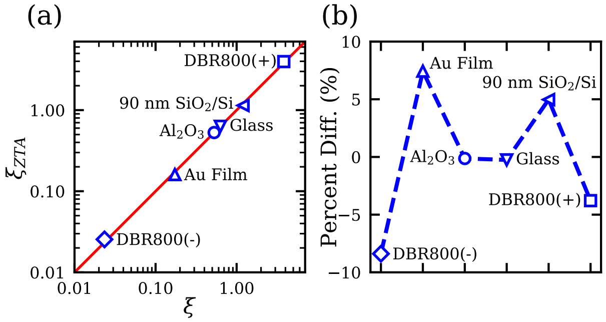

Figure 2.1: (a) Comparison of the internal intensity enhancement factor calculated from the rigorous Airy formula ξ and ZTA ξ_{ZTA} at 800 nm. The red line represents the ideal one-to-one ratio. (b) The percent difference between ξ and ξ_{ZTA} for the substrates in (a). A positive percentage means ξ is larger than ξ_{ZTA}.

Based on Equations (2.1)-(2.3), we can define an internal intensity enhancement factor $\xi = |\mathcal{E}_{2DM}|^2/|\mathcal{E}_{inc}|^2$. Figure 2.1a compares the ξ_{ZTA} based on the ZTA with the rigorous ξ calculated from Equation (A.1). For the latter, the intensity is averaged over the thickness of the 2D material according to Equation (A.2). Figure 2.1a shows excellent agreement between ξ and ξ_{ZTA} for the various substrates under consideration. The red line in Figure 2.1a represents the ideal one-to-one ratio. Interestingly, the 90 nm SiO_2/Si substrate has a ξ close to unity (∼1.14). Figure 2.1b shows that the percent differences for various substrates are all within 5% except the Au film (7.4%) and the DBR800(-) substrate (-8.4%). For the former, the large difference is due to Au's large extinction coefficient (∼5 at 800 nm), while for the latter the DBR800(-) substrate simply has a predicted internal intensity close to zero. The excellent agreement between ξ and ξ_{ZTA} indicates the internal field ξ_{2DM} inside the 2D material is to a very good approximation solely determined by the surrounding media. The result is believed to be very useful for practical applications as ξ_{ZTA} can be applied to all 2D materials.

2.3 Intrinsic Ablation Threshold

To experimentally investigate this etalon effect in femtosecond laser ablation of 2D materials, monolayer MoS_2 is used since it is one of the most widely studied TMDs, but the results here are expected to apply for all 2D materials in general. As outlined in the Materials and Methods section, monolayer MoS_2 films were CVD-grown on Al_2O_3 substrates and transferred to all the substrates used in this work (Figure 2.2a). A single pulse from an ultrafast amplifier operated at 160 fs and 800 nm was focused on the MoS_2 film using a 10× microscope objective with a 0.26 NA. The sample was translated to a fresh spot for subsequent exposures to avoid incubation effects. Figure 2.2a shows optical images of transferred monolayer MoS_2 films on various substrates where single-shot ablated holes with similar diameters are shown in the insets. The fluences ranged from 20 mJ/cm^2 to 400 mJ/cm^2, and no ablation was observed for the MoS_2 on the DBR800(-) substrate before the substrate itself was damaged at a fluence of 660 mJ/cm^2. Overall, Figure 2.2a clearly demonstrates that substrates have a strong influence on the optical contrast of the films and on the ablation fluence required to make holes of similar size. Figure 2.2b shows an atomic force microscope (AFM) image and cross-sectional profile of a typical ablation spot in the MoS_2 film on Al_2O_3, indicating that material has been removed.

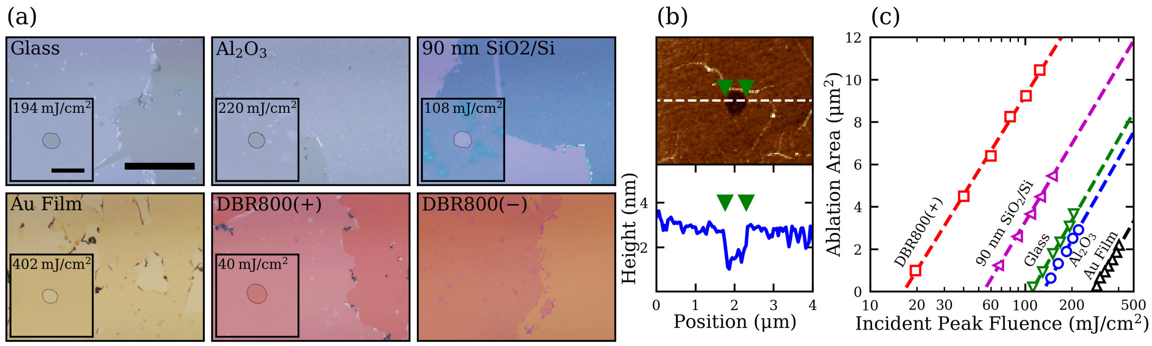

Figure 2.2: (a) Optical images of monolayer MoS_2 films on different substrates, demonstrating the variation in optical contrast. The scale bar is 50 µm. The inset images show ablated holes of similar ablation areas at the indicated laser fluence. The contour of these holes is outlined. The scale bar of the inset images is 4 µm. (b) AFM scan and its cross-sectional profile of a typical ablated hole of MoS_2 on Al_2O_3. (c) The ablation areas as a function of the peak fluence of the incident pulse. The intercept of the fit with the horizontal axis represents the ablation threshold, and the slope is proportional to the laser spot size.

Next, to accurately measure the ablation threshold, the ablation area was measured as a function of the pulse energy, following the method outlined by Liu [92]. Figure 2.2c shows the ablated area as a function of incident peak fluence for different substrates. The experimentally determined threshold fluences F_{th} are approximately 130, 276, 110, 54, and 16 $\mathrm{mJ/cm}^2$, for Al_2O_3, Au film, glass, 90 nm SiO_2/Si, and DBR800(+), respectively. Figure 2.2c clearly shows that F_{th} on various substrates taken by the same laser pulses can differ by an order of magnitude, confirming that substrates have a very strong influence on the laser ablation of 2D materials. According to the theory of dielectric breakdown, the onset of ablation of materials is characterized by a well-defined absorbed energy density required to break atomic bonds, corresponding to a threshold fluence. If the observed variation in F_{th} is purely due to the etalon effect, F_{th} should be inversely proportional to the internal intensity enhancement in MoS_2, that is,

$$F_{th}\xi \approx F_{th}\xi_{ZTA} = \text{constant} = F_{th}^{int}. \tag{2.4}$$

Equation (2.4) defines the intrinsic ablation threshold F_{th}^{int}, which is the ablation threshold fluence for a free-standing 2D material where ξ_{ZTA} equals unity. F_{th}^{int} is a unique threshold parameter for a 2D material that is independent of the underlying substrate. By further defining a normalized ablation threshold $F'_{th} = F_{th}/F_{th}^{int}$, Equation (2.4) is reduced to a more compact form

$$F'_{th}\xi_{ZTA} = 1. \tag{2.5}$$

The experimentally determined ablation thresholds for MoS_2 supported by the Al_2O_3, glass, 90 nm SiO_2/Si, and DBR800(+) substrates in Figure 2.2c are fitted to $F_{th} = F_{th}^{int}/\xi_{ZTA}$ where F_{th}^{int} is used as a fitting parameter (see Appendix A). This fit yields $F_{th}^{int} \approx 66\,\mathrm{mJ/cm^2}$ for monolayer MoS_2. F'_{th} and ξ_{ZTA} for various substrates are shown as solid circles in Figure 2.3, together with the theoretical line of Equation (2.5). The excellent agreement for all these substrates except the Au film (to be discussed below) demonstrates that the dominating effect of these substrates in the single shot ablation of TMDs is the etalon effect, even though their thermal conductivities vary over two orders of magnitudes [93].

This result may not be too surprising, if we consider that the time scale for energy deposition by femtosecond pulses is much shorter than any phonon diffusion time such that there is little time for heat to flow into the substrates during the ablation process. With high-repetition-rate femtosecond lasers, however, quasi-CW laser heating of the substrates is expected to occur such that heat transfer to the substrates may occur during the ablation. To investigate this conjecture, we conduct line-scan experiments where the MoS_2 film is exposed to an 80 MHz pulse train from an ultrafast oscillator while translating at a constant speed. Figures 2.4a-2.4c show respectively an optical microscope (OM) image, AFM height, and AFM cross sectional profile of a line scan with a fluence of $34\,\mathrm{mJ/cm^2}$ and a scan speed of 100 µm/s on the 90 nm SiO_2/Si

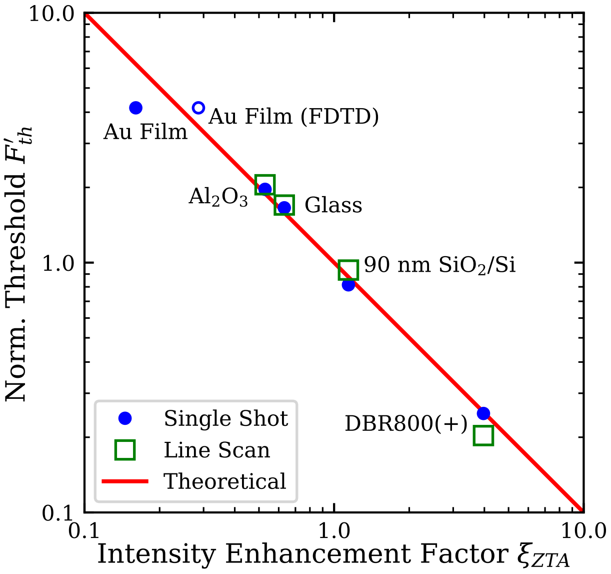

Figure 2.3: Scaling between the normalized ablation threshold and the calculated internal intensity enhancement factor at 800 nm for both single-shot and line-scan ablation. The internal intensity was calculated following the ZTA approximation for all substrate. An additional point for the internal intensity for the Au film was calculated by FDTD. The ablation threshold is normalized to the intrinsic ablation threshold F_{th}^{int}.

substrate. Here, clean removal of monolayer MoS_2 is also observed.

Similar to the single-shot trials in Figure 2.2c, a line-scan ablation threshold F_{th} for the MoS_2 film can be extracted by extrapolating the dependence of the line width squared on the peak incident fluence. Figure 2.4d shows the data and the fits for various substrates, taken with a fixed scan rate of 100 µm/s and a 0.26 NA focusing objective. The extracted line-scan F_{th} of MoS_2 are 54, 49, 25, and 5 mJ/cm^2 for Al_2O_3, glass, 90 nm SiO_2/Si, and DBR800(+) substrates, respectively. Analogous to the single-shot thresholds, the line-scan thresholds are fitted to Equation (2.4) (see Appendix A). This fit yields $F_{th}^{int} \approx 26$ mJ/cm^2 for monolayer MoS_2 at a scanning speed of 100 µm/s. The normalized thresholds F'_{th} for the line-scan trials are then added to Figure 2.3, exhibiting again excellent agreement with Equation (2.5). Given the thermal nature of the quasi-CW excitation, the variation of line-scan F_{th} is still largely governed by the etalon effect of the substrates. We conclude that these sub-

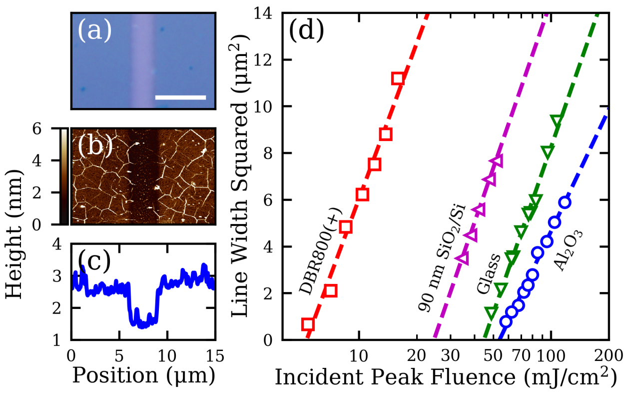

Figure 2.4: (a) An example OM image of a line patterned into a MoS_2 film on 90 nm SiO_2/Si. The scale bar is 5 µm. (b) The corresponding AFM height map to the OM image in (a). (c) An average line profile taken from the AFM height map in (b). (d) Plot the of the line width squared versus the incident peak fluence for lines patterned in a MoS_2 on various substrates. The scan speed was set to 100 µm/s.

strates behave as very poor heat sinks for ultrafast laser ablation of 2D materials, irrespective of the substrates' thermal properties. In other words, the ablation process is adiabatic. We attribute this adiabaticity to the very low thermal boundary conductance (TBC) between MoS_2 and the substrates. Literature has reported TBC values ranging between 0.1-34 MW/m^2/K for MoS_2 on SiO_2/Si substrates [94, 95] and between 19-38 MW/m^2/K on a sapphire substrate [96]. Additionally, mechanically exfoliated and as-grown MoS_2 monolayers on a SiO_2/Si substrate are shown to have similar TBC values [95]. Therefore, we expect that the ultrafast ablation of as-grown films share the same adiabaticity as the transferred films.

Our finding that femtosecond ablation is adiabatic is in sharp contrast to the general belief that the substrates serve as a heat sink for laser processing. For example, Yoo *et al.* reported $F_{th} = 98$ mJ/cm^2 for graphene on 285 nm SiO_2/Si and $F_{th} <$ 43 mJ/cm^2 for suspended graphene in single-shot femtosecond laser ablation [82]. They attributed this difference to the adiabatic condition of suspended graphene where heat dissipation through the substrate is forbidden. Based on our finding here, we offer an alternative interpretation. Considering the etalon effect, ξ_{ZTA} are 0.2 and 1 for 285 nm SiO_2/Si (see Figure A.1d) and air substrates, respectively. Based on $F_{th} = 98$ mJ/cm^2 for graphene on 285 nm SiO$_2$/Si substrate, we can estimate $F_{th} \sim 20\,\text{mJ/cm}^2$ for a suspended graphene, which is consistent with $F_{th} < 43\,\text{mJ/cm}^2$ reported by the authors. Moreover, the knowledge of F_{th}^{int} and ξ_{ZTA} (i.e., Figure 2.1a) makes F_{th} predictable for any substrate, according to Equation (2.5)). For example, given that $F_{th} = 54$ mJ/cm^2 (Figure 2.2c) and $\xi_{ZTA} = 1.14$ (Figure 2.1a) for the 90 nm SiO$_2$/Si substrate, the predicted threshold for the DBR800(+) substrate with $\xi_{ZTA} = 3.97$ (see Figure A.1e) is $F_{th} = 15\,\text{mJ/cm}^2$, which matches very well with the experimental threshold of $16\,\text{mJ/cm}^2$.

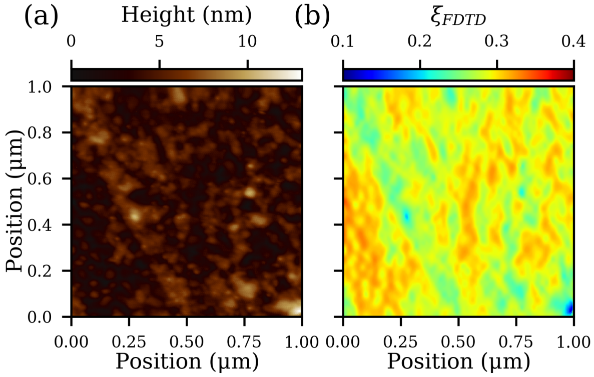

Figure 2.5: (a) AFM height scan of a 1 µm × 1 µm square of the Au surface. (b) Calculated intensity enhancement ξ_{FDTD} across the simulation surface based on the AFM image in (a). See the text for details.

Among the single-shot trials (solid circles) in Figure 2.3, the predicted ablation threshold based on ξ_{ZTA} for a smooth Au film is 40% higher than the experimental value, indicating the presence of an additional enhancement process beyond the etalon effect that increases the internal field. An AFM measurement (Figure 2.5a) revealed that the Au film substrate has a peak-to-peak surface roughness of 13 nm and an RMS value of 1.54 nm. This rough Au surface could lead to a local plasmonic enhancement of the incident field. Figure 2.5b shows a FDTD simulation of the electric field distribution at a fixed height of 0.325 nm (corresponding to half of the monolayer thickness) above the maximum height in Figure 2.5a. The result is only approximate, as the MoS$_2$ film may conform to the Au surface which is unaccounted in the current simulation. Additionally, the MoS_2 film itself is not included in the simulation to ease the computational demand and to comply with the ZTA. Nevertheless, the laterally averaged intensity enhancement factor in Figure 2.5b yields a much better match with F'_{th} for the Au substrate, as indicated by the empty circle in Figure 2.3. More importantly, this result demonstrates that plasmonically active substrates could also be used to enhance the ablation of 2D materials compared to a flat metal surface. With a stronger plasmonically active substrate, even larger enhancements would be possible to further increase the ablation efficiency.

2.4 Ultrafast Laser Patterning

For laser patterning applications, the patterning speed and resolution are important performance metrics. Given that SiO_2/Si substrates are commonly used for field-effect transistors, Figure 2.6a shows the ablated line width in MoS_2 on the 90 nm SiO_2/Si substrate as a function of the scan rate with a constant fluence of about 46 $\mathrm{mJ/cm^2}$ and a 0.26 NA focusing objective [5]. Selected OM images of ablated lines are shown Appendix A. As the scan rate increases from 1 μm/s, the line width decreases from 8.7 μm before leveling off at 2.9 μm at 5 mm/s. The leveling off at high scan rates is due to the mechanical instability of the translation stage used here, where the stage vibrates resulting in larger widths and uneven lines (see Appendix A). Nevertheless, Figure 2.6a clearly demonstrates high-speed line patterning of TMDs. This translates into increased patterning efficiency of an ultrafast source compared to a CW source: with a scan rate of 5 mm/s, material can be removed at a rate greater than 14,000 μm^2/s by ultrafast lasers, whereas CW laser thinning can only pattern monolayers at a rate of 8 μm^2/min [80].

To demonstrate sub-micron patterning resolution, Figures 2.6b-2.6e show an array of ablated lines in a MoS_2 film on the DBR800(+) substrate obtained with a 50×, 0.55 NA focusing objective. The AFM height image has poor quality due to the surface roughness of the DBR800(+) substrate (see Appendix A), while the AFM

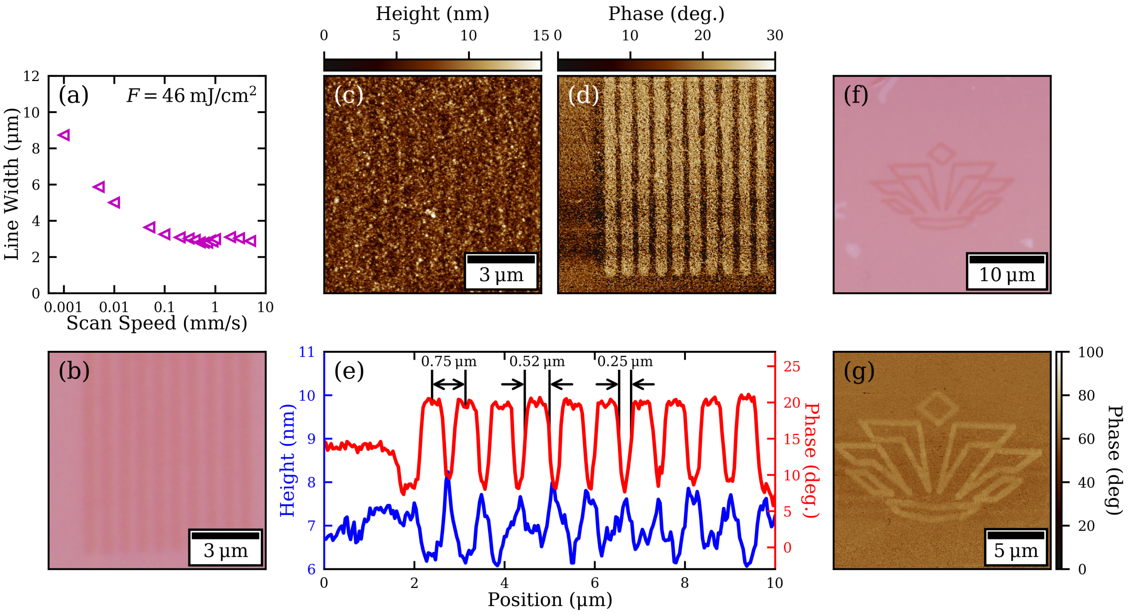

Figure 2.6: (a) A plot of the patterned linewidth in a MoS_2 on a 90 nm SiO_2/Si substrate as a function of the scan speed. (b) OM image of parallel channels patterned in a MoS_2 on the DBR800(+) substrate. The incident fluence was 10 mJ/cm^2 and the scan rate was 5 µm/s. (c) AFM height and (d) phase maps corresponding to the OM image in (b). (e) Averaged cross-sectional profiles of the AFM height and phase maps in (c) and (d). (f) OM image of the UNC Charlotte crown logo patterned into a monolayer MoS2 film on the DBR800(+) substrate. The incident fluence was 10 mJ/cm^2 and the scan rate was 3 µm/s. (g) AFM phase map of the patterned UNC Charlotte crown in (f).

phase image clearly resolves the grating pattern where an average trench width of 0.52 µm and ribbon width of 0.25 µm are measured. To demonstrate laser micropatterning, the UNC Charlotte crown logo was patterned into a MoS_2 film on the DBR800(+) substrate as shown in Figure 2.6f. The total size of the pattern is 20 µm and was engraved using a fluence of 10 mJ/cm^2 and a low feed rate of 3 µm/s to avoid skewing the pattern (see Appendix A). The thicknesses of the lines in the logo were found to be around 0.7 µm as measured by the AFM phase mapping. For practical applications, cost is also an important consideration. Although Figures 2.2c and 2.4d have demonstrated femtosecond ablation and patterning of MoS_2 on several substrates, the large field enhancement of the DBR800(+) substrate only requires pulse energies as low as 1 nJ for single-shot ablation and on the order of 100 pJ for line scans, as demonstrated in Figure 2.6. This pulse energy translates to an average power of 80 mW which is readily available from compact femtosecond oscillators (see Appendix A). With a proper design, the substrate could be engineered to enhance both the patterning process and the light-coupling performance of the resulting device. Alternatively, the patterned film can be transferred to other substrates [81, 97].

2.5 Conclusion

In conclusion, femtosecond laser patterning of monolayer MoS_2 was performed for the first time, where we demonstrated scan rates as high as 5 mm/s and resolutions as low as 250 nm under modest focusing conditions. We observed a nearly 20× variation in the threshold fluence for the femtosecond ablation of transferred MoS_2 monolayer on several substrates. This variation is attributed to the etalon effect where the substrate modulates the internal light intensity within the monolayer. An intrinsic ablation threshold F_{th}^{int} is thereby introduced as a substrate-independent threshold parameter for laser ablation of 2D materials, which were found to be $66\,\mathrm{mJ/cm^2}$ and $26\,\mathrm{mJ/cm^2}$ for single-shot and quasi-CW ablation (80 MHz pulse train at a scanning speed 100 μm/s), respectively, for MoS_2. With this knowledge, we showed that the incident threshold fluence on any substrate is easily predicted. Additionally, we proved that the ablation process is adiabatic due to the very poor thermal boundary conductance between the monolayer and the substrates, which contradicts the common view that substrates serve as heat sink for laser processing. Importantly, we also introduced the zero-thickness approximation for quick and accurate estimation of the etalon effect in monolayers, which is shown to be independent of the 2D materials and applicable for any optical excitation of 2D materials beyond laser ablation. Furthermore, substrate engineering is demonstrated to enhance the ablation efficiency by 7×, enabling future patterning of 2D materials with low-power oscillators. Finally, the notion of the intrinsic threshold fluence highlights the importance of invoking the internal field instead of the incident field for studying strong-field phenomena in monolayers, including nonlinear absorption, saturable absorption, dielectric breakdown, etc., which, as it stands, also have significantly conflicting reported values, largely because they all neglect the etalon effect in their analysis [4, 56]. Although transferred MoS_2 monolayers were studied in this work, we expect our findings can be generalized to other 2D materials, both transferred and as-grown. Our work elucidates the role of substrates and firmly establishes femtosecond laser ablation as a viable route to pattern 2D materials.

2.6 Experimental Methods and Materials

Highly-oriented, monolayer MoS_2 films were grown by CVD on *c*-cut Al_2O_3 following the procedure by Hsu *et al.* and as outline in Chapter 1.1 [14]. All films were transfered to their host substrates which included 70 nm Au film, Al_2O_3, borosilicate glass, 90 nm SiO_2/Si, and two different DBR susbtrates. The transfer process is also outlined in Hsu *et al.* [14]. For single-shot ablation trials, MoS_2 samples were exposed to 160 fs pulses from an amplified Ti:S laser (Coherent RegA 9000) operated at a center wavelength of 800 nm. The laser was operated at a repetition rate of 307 Hz. The pulses were focused onto the sample surface with a microscope objective (Mitutoyo M Plan Apo NIR 10×, 0.26 NA). Each spot on the film was exposed to a single pulse to create an ablation feature while the sample was translated to a fresh spot for each subsequent exposure. For line-scan experiments, a Ti:S oscillator (Spectra-Physics Tsunami) was used which emitted 210 fs pulses at a center wavelength of 800 nm and repetition rate of 80 MHz. Sample positioning and translation was performed using an Aerotech ANT three-axis motorized translation stage. The pulse energy was simultaneously recorded using a calibrated photodiode. More information about the general experimental setup can be found in Appendix D.

CHAPTER 3: FEMTOSECOND LASER-INDUCED BREAKDOWN AND THE ROLE OF AVALANCHE IONIZATION IN MOLYBDENUM DISULFIDE

3.1 Introduction

Two-dimensional materials such as graphene, transition metal dichalcogenides (TMDs), and h-BN have been extensively studied due to their extraordinary electronic and optoelectronic properties [2, 41–43]. In particular, TMDs such as MoS_2, WS_2, and $MoSe_2$ are of great interest since they exhibit strong excitonic resonances and possess a direct band gap in their monolayer form [3, 44]. These semiconducting TMDs are promising candidates for future nanoelectronics such as field effect transistors [5, 45, 46], phototransistors [12, 48], LEDs [49, 50], and chemical sensors [51, 52] which rival similar graphene based devices. Many of these TMD-based devices are developed from natural crystals where single atomic layers are extracted through mechanical exfoliation. For rapid device development and manufacturing, single crystal and large, highly-oriented MoS_2 films can be synthesized through chemical vapor deposition (CVD) which can then be easily transferred and patterned. Many studies regarding the laser patterning and ablation of graphene have been reported for this application but little has been discussed regarding TMDs [58–64].

A couple of studies have investigated how MoS_2 responds under intense femtosecond excitation near the ablation threshold but provide little information on the ablation process itself [7, 65]. Paradisanos *et al.* examined the Raman modes of both bulk and monolayer MoS_2 flakes after multiple exposures to ultrafast pulses. They showed that monolayer flakes were more resistant to degradation than its bulk counterpart and suggest that the onset of damage results in the sublimation of the material. However, further work is necessary to confirm this mechanism. Studying and quantifying the

the ablation process and features of TMDs is important in order to understand how these materials respond to intense excitation and to optimize the laser patterning process.

Due to their reduced dimensionality, 2D materials provide a unique opportunity to study strong field physics. Much research has been performed regarding the intense excitation and optical breakdown of bulk semiconductors and dielectrics where the roles of multi-photon, tunneling, and avalanche ionization have been analyzed and discussed. Effects such as spatial-temporal beam propagation, self-limiting and intensity clamping, and longitudinal carrier diffusion, which play important roles in bulk micromachining, disappear in 2D materials. In addition, the effects of quantum confinement may influence the energy coupling, energy distribution, and carrier densities in monolayer TMDs, leading to enhanced or mitigated processes that differ from their bulk counterparts. In this chapter, a quantitative study is conducted to understand the ablation of CVD grown MoS_2 involving single crystal, monolayer flakes, and the role of avalanche ionization is discussed.

3.2 Characterization of Ablation Features

All monolayer TMDs used here were grown by CVD on a *c*-cut apphire (Al_2O_3) substrate [14]. The TMD flakes are then transferred to a 90 nm SiO_2/Si substrate using a PMMA film. The PMMA is then dissolved with acetone, leaving behind only the flakes. Monolayer growth was verified by Raman spectrscopy and atomic force microscopy (AFM). Monolayer graphene on 90 nm SiO_2/Si was purchased from Graphenea. The TMD and graphene samples are exposed to 170 fs pulses from an amplified Ti:S laser (Coherent RegA 9000) operated at a center wavelength of 800 nm. The pulses were focused down to a spot size less than 5 μm in diameter using a 10× objective with a 0.26 NA. Each spot on a flake was exposed to a single pulse to create an ablation feature while the sample was translated to a fresh spot for each subsequent exposure. The peak fluence was varied between 30-200 mJ/cm^2 and at least five features were made per fluence to ensure repeatability.

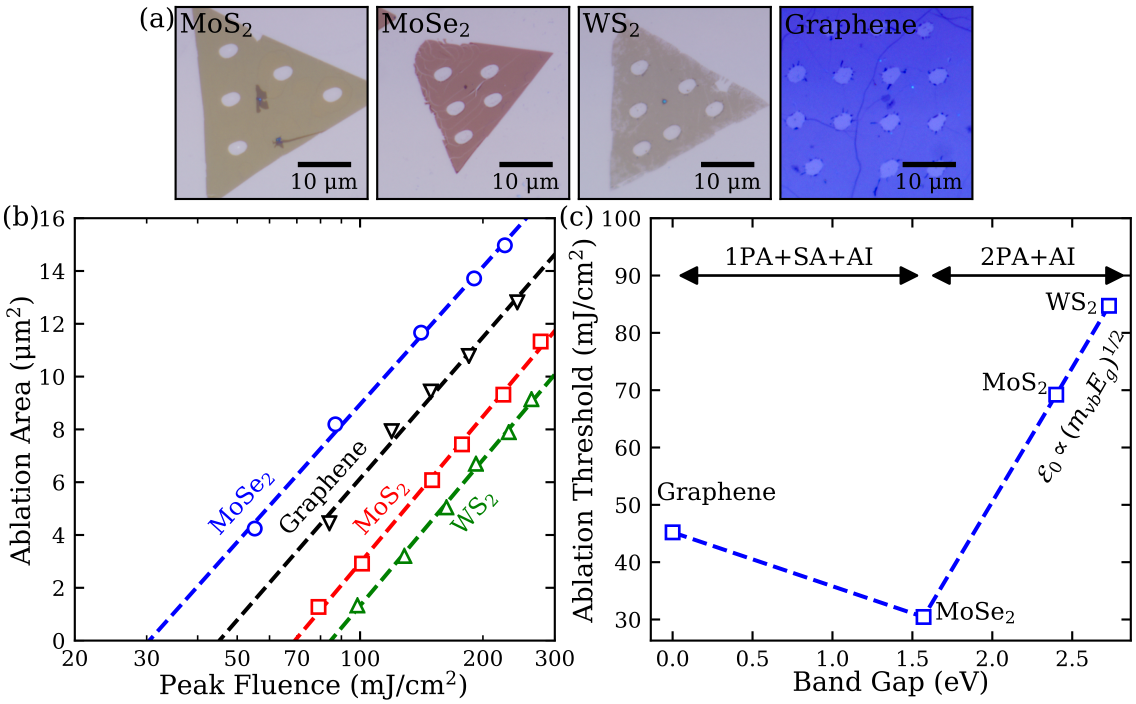

Figure 3.1: (a) Optical images of the ablation of 2D materials. (b) The ablation areas are fitted as a function of the peak fluence of the incident pulse. The intercept with the horizontal axis represents the ablation threshold and the slope if directly proportional to the laser spot size. (c) The ablation thresholds as a function of band gap. The optical band gap is plotted for $MoSe_2$ and the electronic band gap is plotted for MoS_2 and WS_2.

The ablation features are first characterized by optical microscopy (OM) as shown in Figure 3.1a. OM images show clean removal of material with minimal damage to the underlying substrate. The shapes and sizes of the holes are easily repeatable and match the spatial profile of the pulse. Using this property, the ablation area A follows the expression

$$A = \frac{\pi}{2} w_{eff}^2 \ln\left(\frac{F}{F_{th}}\right) \tag{3.1}$$

where $w_{eff} = \sqrt{w_u w_v}$ is the effective spot radius at an intensity of e^{-2}, w_u and w_v represent the major and minor axes for an elliptical spot, F is the peak fluence of the incident pulse, and F_{th} is the peak fluence at the ablation threshold [92]. The areas produced by different fluences can be fitted to this equation to accurately determine the ablation threshold. Equation (3.1) is only true when there is no lateral diffusion of carriers. If a high order multi-photon process is present and carrier diffusion is significant, then the effective spot size measured by the fit may underestimate the real laser spot size [98]. This equation though has shown to hold true experimentally in the case of two-photon absorption for several materials [37, 99]. For all of the ablation experiments conducted here, the spot size measured by the fit matched the spot size measured using a CCD camera to within 5%, allowing this method to accurately determine the spot size *in situ*. For example, the average spot size as determined from the fits in Figure 3.1b was $w_{eff} = 2.23\ \mu\text{m}$ where as the spot size measured by the CCD was $w_{eff} = 2.18\ \mu\text{m}$, which yields a difference of 2.2%. The agreement between the fitted equation and the CCD confirms that the ablation area remains localized to within the laser spot and that carrier diffusion is minimal on the time scale of the ablation. Finally, Figure 3.1c plots the measured ablation thresholds as a function of band gap which will be discuss later.

One discernible difference between the ablation of graphene and MoS_2 is the production of regular hole shapes. When exposed to ultrafast pulses, graphene demonstrates a folding phenomenon at the edges of the hole which can often result in irregular hole shapes and sizes [82, 83, 100]. This same phenomena was observed for graphene in this work but is not apparent from OM for MoS_2. To quantify the regularity of the hole, the spatial profile of the pulse was matched to the ablation features of both MoS_2 and graphene as outline in Figure 3.2. By positioning, rotating, scaling, and setting the laser profile intensity level or clip level, the laser spot can be fitted to the ablation area to measure how well the laser spot matches the ablation features. To quantify this fit, the difference between the fitted laser spot profile and a thresholded ablation profile were taken, resulting in an image whose pixels do not overlap either the laser spatial profile or the ablation profile as shown in Figures 3.2a-3.2d.

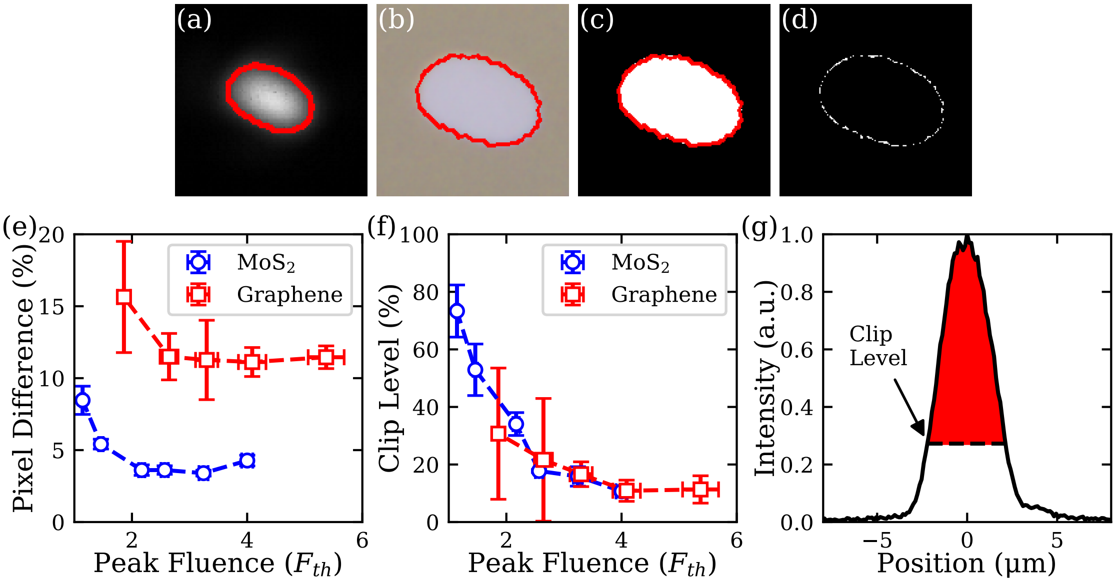

Figure 3.2: (a) The spatial profile of the laser spot at focus. The red outline represents the level of constant intensity. (b) Ablation hole on a MoS_2 flake with the spatial profile of the laser matched to the ablation hole. (c) A thresholded image of the ablation hole with the matched laser profile. (d) A thresholded image of the ablation hole showing the difference in pixels between the hole itself and the matched spatial profile of the laser. (e) Pixel difference between the ablation hole and the spatial profile for the different hole sizes. (f) The intensity profile clip level that best fits the ablation hole. (g) The intensity level of the spatial profile that matches the ablation hole shown in images (a)-(d).

The pixel difference was then normalized to the number of pixels that make up the ablation feature and plotted as a function of fluence in Figure 3.2e. The pixel difference for graphene is found to be 2× larger than compared to MoS_2, illustrating the stochastic, explosive nature of ablation for graphene compared to the deterministic ablation of MoS_2. The explosive nature of graphene is further emphasized at fluences $F < 3F_{th}$. In this fluence range, the uncertainty in pixel difference and clip level for graphene increase significantly. For graphite, experiments have shown that Coulomb explosion dominates ablation at fluences near threshold [101–103]. The presence of folds and irregular hole shapes may be evidence of Coulomb explosion in the ablation of graphene. The stark contrast in the ablation features of MoS_2 and graphene suggest very different ablation dynamics and provide further motivation to study the ablation of MoS_2.

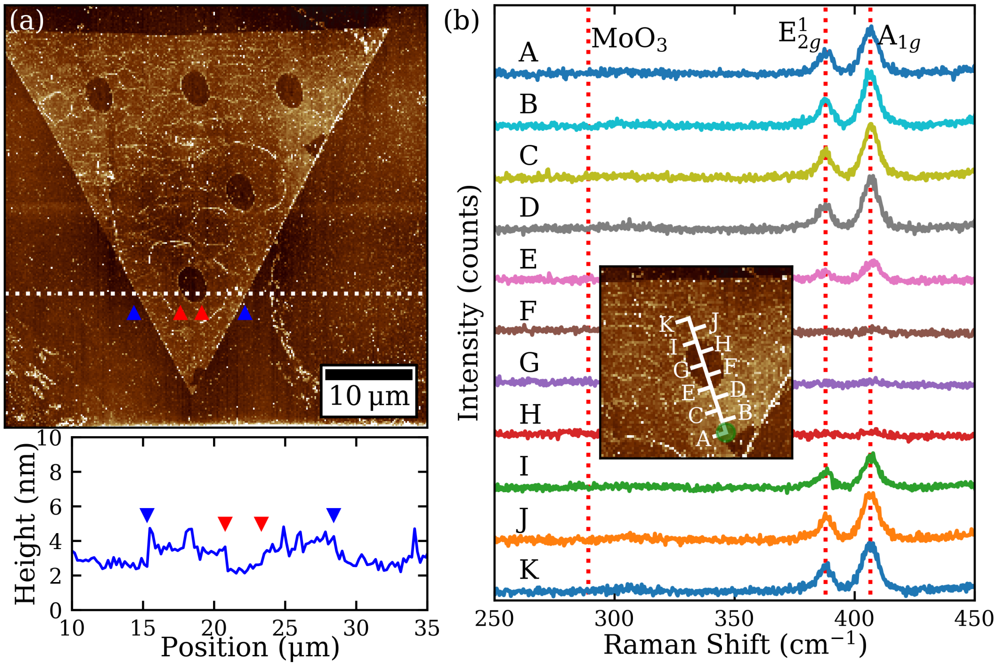

Figure 3.3: (a) AFM scan and (b) Raman scan of MoS_2 after ablation showing clean removal of material.

In addition to OM, AFM and Raman spectroscopy were used to further characterize the ablation features. Similar to OM images, AFM also confirms the clean removal of material under high fluences as shown in Figure 3.3a where the hole height matches the height for monolayer MoS_2. Raman spectroscopy gives a similar result where Figure 3.3b shows a line scan across a hole in a MoS_2 flake. Two dashed vertical lines at 388 cm^{-1} and 406 cm^{-1} represent the in-plane E^1_{2g} and the out-of-plane A_{1g} vibrational modes for monolayer MoS_2. A common peak for MoO_3 is also labeled at 289 cm^{-1}. As the Raman spectra for various points across the hole are recorded, the peaks associated with MoS_2 disappear while no peaks were detected for MoO_3. No peaks were also measured at 810 cm^{-1}, another common peak for MoO_3. At fluences greater than $2F_{th}$, clean removal of material with minimal modification to the edges of the hole is achieved, which is an attractive feature for laser patterning. These properties ensure that TMDs can be shaped in any fashion while maintaining their electronic and optical properties for various applications.

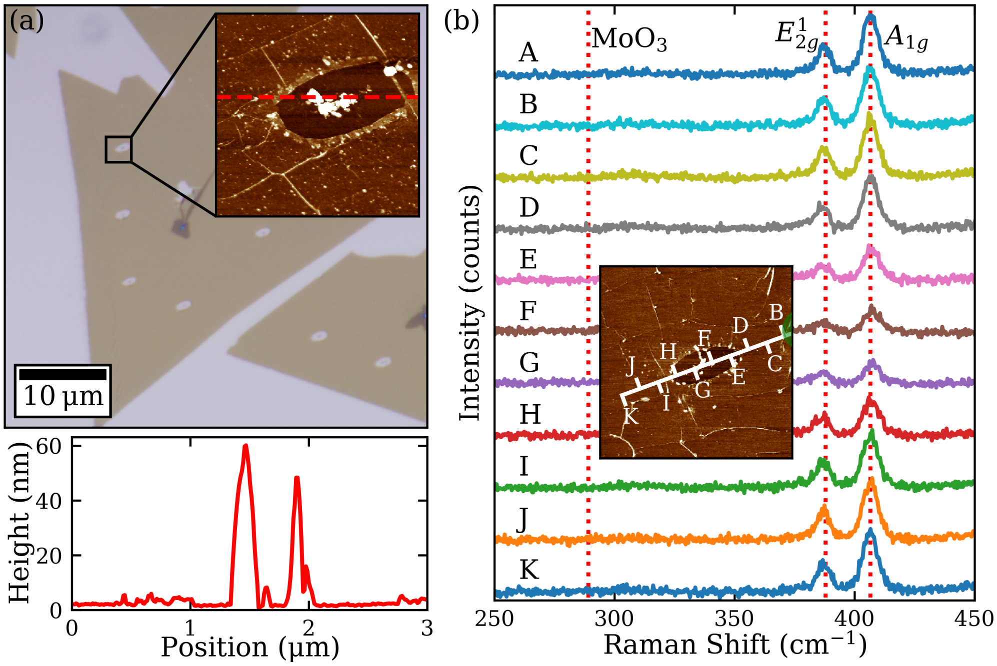

Figure 3.4: (a) OM, AFM, and (b) Raman scan of MoS_2 at a fluence of $1.5F_{th}$.

At low fluences ($F < 2F_{th}$), some residual material is visible through OM in the center of the ablation hole. AFM of these features were also recorded and shown in Figure 3.4a. The height of this residual material is giant (>10 nm) when compared to the height of the monolayer flakes. Additionally, the presence of nanofolds was confirmed with AFM where the fold lengths were 150 nm or less. Raman spectroscopy of the residual material did not reveal any new peaks. There are a couple conclusions that can be made based on this result though. One group proposed material removal during the ablation of MoS_2 occurs through sublimation [65]. Since some material remains after ablation, other mechanisms such as ultrafast melting followed by evaporation, resolidification, or oxidation are possible.

The absence of the MoO_3 peak in the Raman spectrum in Figure 3.4b does not disprove the oxidation of MoS_2. Multiple groups have measured oxidation of MoS_2 due to continuous-wave (CW) laser thinning. One group used *i*-XPS after laser thinning where they confirmed the presence of Mo_xO_y with Mo_2O_5 being the most probable state [104]. In the same work, they also showed the presence of amorphous MoS_2. Another group measured the presence of amorphous MoO_x through Raman spectrscopy using a HeCd laser operating at 325 nm [105]. The same Raman modes were not measurable when 442 nm or 532 nm sources were used. They explain two reasons for this result. Firstly, since the band gap of amorphous MoO_x is about 3.59 eV, the resonant excitation of 325 nm light leads to enhanced Raman scattering. Secondly, the Raman scattering cross-section scales as λ^{-4} which means the Raman modes are more efficient for shorter wavelengths. They also gave another indicator for the presence of MoO_x. The density of amorphous MoO_x is less than MoS_2. During CW laser thinning experiments, the formation of amorphous MoO_x led to the local increase in film height by up to 6 nm which was easily measurable with AFM. The volume of the residual material in Figure 3.4a was about 2.8× larger than the volume of the hole itself. Based on these results, the residual material in Figure 3.4 may be amorphous MoO_x but further work is needed to confirm the material composition.

3.3 Experimental Evidence For Avalanche Ionization

To better understand the carrier dynamics at ablation, the dependence of ablation on crystal orientation and incident polarization was investigated. The ionization and ablation of many crystals such as GaAs, ZnSe, MgO, and LiF have been shown to strongly depend on the crystals' orientation with respect to the linear polarization of the incident pulse [31, 106, 107]. This orientation dependence directly corresponds to the crystalline axes of the material and is easily incorporated into Keldysh's theory by simply considering the different electron effective masses along each crystal axis [26]. To investigate this dependence, MoS_2 was exposed to pulses whose polarization were aligned with the zigzag and armchair crystalline directions as illustrated in Figure 3.5a. No crystalline dependence was observed with the results for MoS_2 shown in Figure 3.5b.

The first possibility is that the electron and hole effective masses along each crystal

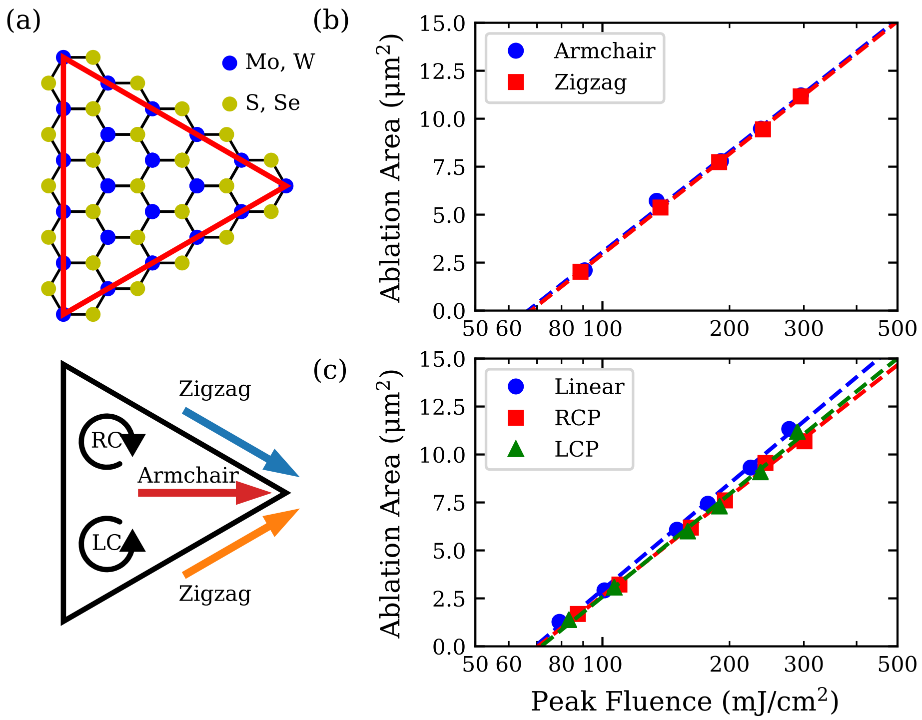

Figure 3.5: (a) Crystal structure of a single crystal TMD flake. Four polarizations were tested: linearly polarized light along the armchair and zigzag directions and left and right circularly polarized light. (b) Ablation areas for the armchair and zigzag crystal orientations for MoS_2. (c) Ablation areas for linearly, right circularly (RCP), and left circularly polarized (LCP) light for MoS_2. The linearly polarized light is randomly oriented to the crystal axes.

axis are the same. This case is true if the carrier transition occurs at the K point in the band structure where the effective masses are expected to differ by less that 1% between each crystal direction [108]. For MoS_2, the transition from the valence band max to the second conduction band is about 3 eV at the K point, which is nearly resonant with 800 nm (1.55 eV) excitation when considering 2PA [109]. If the transition is away from the K point, then the effective masses can differ by up to 50% depending on the crystal orientation [108]. At the fluences tested here, a 50% difference in effective mass corresponds to a 35% difference in the ionization rates between the different crystalline directions as determined by Keldysh's theory (Figure 3.6).

The second possibility is that the predominant carrier generation mechanism is AI.

In bulk crystals such as GaAs, the ablation feature size strongly depends on the crystal orientation for fluences near the threshold where MPI dominates. At larger fluences, carrier generation transitions from MPI to AI which depends on the average kinetic energy or temperature of the free electrons and is insensitive to crystal orientation [107]. Additionally, AI has shown to play an important role for pulse durations greater than 100 fs [38]. Given that the pulse duration here is 170 fs, AI is expected to have a significant impact on the ionization rate.

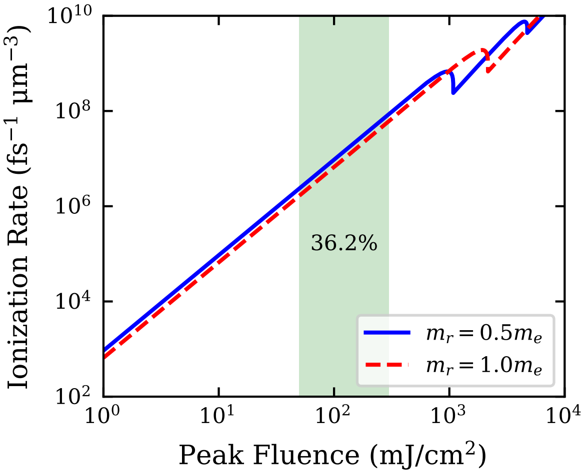

Figure 3.6: Calculated ionization rates based on Equation (1.7) for monolayer MoS_2 for two different effective masses. The region shaded in green corresponds to the experimental fluence range investigated. The ionization rates differ, on average, by 36% in this fluence range.

To confirm whether MPI or AI dominates, the ablation of MoS_2 under linearly versus circularly polarized light was tested. If MPI dominates, then the ionization rate is expected to be higher for linearly polarized light, leading to a smaller threshold compared to circularly polarized light. This dependence of the ionization rate has been observed and successfully modeled for InSb where it was shown that the 2PA cross-section for linearly polarized light can be up to 33% larger than for circularly polarized light [110]. Similar results were also observed for fused silica and sapphire [111, 112]. If AI dominates, then the thresholds are expected to be independent of the ellipticity of the incident polarization. Again, the ablation threshold was found to be independent of polarization as shown in Figure 3.5c. The lack of polarization and orientation dependence suggest that AI is the dominate carrier generation mechanism in MoS_2 at ablation.

Further insight in the role of AI can be found in how the ablation threshold scales with band gap. Out of the 2D materials tested here, graphene and $MoSe_2$ had the lowest thresholds of $\sim 45\ \mathrm{mJ/cm^2}$ and $\sim 31\ \mathrm{mJ/cm^2}$, respectively, despite possessing different electrical and optical properties. Graphene is a zero band gap semi-metal while $MoSe_2$ is a direct band gap semiconductor with a strong excitonic resonance at 1.57 eV [113]; however, both materials exhibit 1PA and saturable absorption (SA) at 800 nm. Comparing linear absorption coefficients between the two materials, the absorption coefficient of graphene ($2.4 \times 10^5\ \mathrm{cm^{-1}}$) is about twice that of $MoSe_2$ ($1.3 \times 10^5\ \mathrm{cm^{-1}}$) [114, 115]. At these high intensities though, nonlinear mechanisms will surely be prevalent. Considering SA, literature has shown that the saturation intensity of graphene ($\sim 3\ \mathrm{GW/cm^2}$) is about three orders of magnitude larger than $MoSe_2$ ($\sim 2.5\ \mathrm{MW/cm^2}$) at 800 nm. The modulation depths of graphene and $MoSe_2$ are 73.6% and 80%, respectively [116–118]. The intensities investigated here are greater than $150\ \mathrm{GW/cm^2}$ which is well above the saturation intensities for both graphene and $MoSe_2$. By considering 1PA and its saturation at the ablation threshold, the surface carrier density generated can be estimated and found to be similar at $\sim 4.3 \times 10^{14}\ \mathrm{cm^{-2}}$ and $\sim 2.2 \times 10^{14}\ \mathrm{cm^{-2}}$ for graphene and $MoSe_2$, respectively. Even though the carriers generated in graphene is twice as large, the threshold is 1.5× larger than $MoSe_2$ was well. This difference can be attributed to the exceptional mechanical strength of graphene. Graphene possesses a Young's modulus that is ten times larger than that found in $MoSe_2$ and has a breaking strength that is three times larger as well [54, 69]. The mechanical robustness of graphene allows for high carrier generation before intense ionization leads to Coulomb explosion [119].

The excitation dynamics of MoS_2 and WS_2 are different compared to $MoSe_2$. The optical band gaps or excitonic resonances of MoS_2 and WS_2 are 1.87 eV and 2.02 eV, respectively, which are both larger than the 1.57 eV transition found in $MoSe_2$ [120, 121]. Under 800 nm excitation the incident pulses are resonant with the excitons in $MoSe_2$, allowing for 1PA and its subsequent saturation. For MoS_2 and WS_2, carriers must be generated by 2PA to the electronic band gap which are 2.40 eV and 2.73 eV, respectively [120, 121]. As a result, the thresholds are expected to be larger for MoS_2 and WS_2. A similar calculation can be performed to determine the number of carriers generated due to 2PA. For MoS_2, the 2PA coefficient is ∼60 cm/GW which leads to a carrier density of $\sim 2.1 \times 10^{14}$ cm^{-2} with an excitation intensity of ∼370 GW/cm^2 at ablation [56]. This carrier density is similar to those found for graphene and $MoSe_2$ and demonstrates excellent scaling between the ablation threshold of $MoSe_2$ and MoS_2; however, the critical density to cause ablation has not been determined.

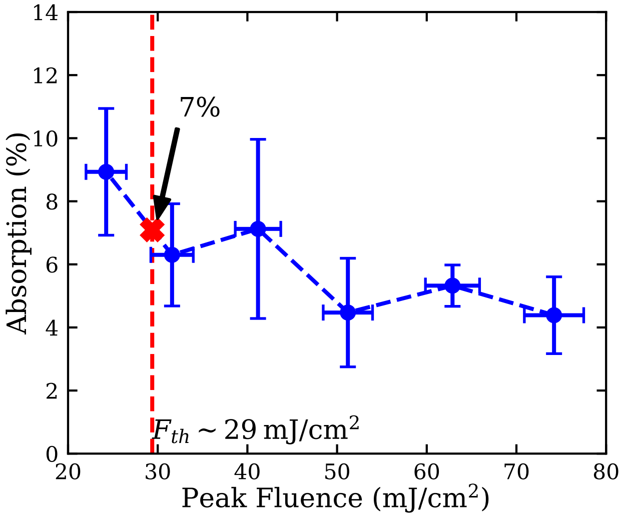

Figure 3.7: Single shot absorption of MoS_2 for 400 nm pulses. The ablation threshold was measured to be ∼29 mJ/cm^2 at 400 nm.

To estimate the carrier density required for ablation, a simple absorption experiment was performed. The 800 nm pulses were frequency doubled at 400 nm and exposed to monolayer MoS_2 which undergoes 1PA with little saturation at this wavelength [7]. The absorption was recorded for fluences above the ablation threshold with the results given in Figure 3.7. Near the ablation threshold, the absorption was found to be ~7%, yielding a peak carrier density of $\sim 4.2 \times 10^{15}$ cm^{-2} which corresponds to 30% of the total valence band population being excited. This percentage is three times larger than that found in bulk materials such as Si and GaAs at the onset of damage [122, 123]. This carrier density is also an order of magnitude larger than those predicted for 800 nm excitation calculated earlier at the ablation threshold for both $MoSe_2$ and MoS_2 when only 1PA and 2PA were considered. To account for this discrepancy, AI must account for the majority of the carriers generated. The fact that 30% of the carriers have been excited provides further evidence that TMDs are more robust than their bulk counterparts and that AI plays a significant role in the breakdown of these 2D materials.

To gain further insight into AI and how the AI rate should scale with band gap in the MPI regime, the total carrier density N can be described to a first order approximation with a single rate equation (SRE) as

$$\frac{dN}{dt} = W_{PI}(t) + \gamma_{AI} I(t) N. \tag{3.2}$$

The first term represents the photoionization (PI) rate that can include both MPI and TI. The second term represents the impact ionization rate. Assuming sufficient seed carriers have been generated and AI is the dominate process, an approximate analytical solution can be obtained for the electric field strength at threshold (see Appendix B). The peak field strength $\mathcal{E}_0$ at threshold follows the proportionality

$$\mathcal{E} \propto (m_{vb} E_g)^{1/2} \tag{3.3}$$

where m_{vb} is the effective mass of a hole in the valence band and E_g is the band gap. If AI truly dominates, then the above ratio should be the same for MoS_2 and WS_2 at their respective ablation fluences. The field strengths at ablation for MoS_2 and WS_2 are 1.85×10^9 V/m and 2.04×10^9 V/m and their effective masses are $0.43m_e$ and $0.40m_e$, respectively [124, 125]. Using these field strengths and their electronic band gaps, the ratios for MoS_2 and WS_2 from Equation (3.3) only differ by ∼7%, further supporting that AI plays a crucial role in the optical breakdown of MoS_2. Figure 3.1c summarizes the ablation thresholds and the important excitation mechanisms involved.

3.4 Modeling Carrier Dynamics

Although Equation (3.3) provides an explanation for the band gap scaling observed in Figure 3.1c, a number of simplifying assumptions were made in order to obtain an analytical result. In order to to extract out an reasonable value for the AI coefficient γ_{AI}, the initial carriers generated by PI and the effects of saturation need to be considered. Accordingly, a modified SRE is introduced and is given by

$$\frac{dN}{dt} = (W_{PI}(t) + \gamma_{AI} I(t) N)\left(1 - \frac{N}{N_{tot}}\right). \tag{3.4}$$

The second term on the right introduces the effects of saturation due to carrier depletion in the valance band. Given the PI rate, critical carrier density, and the pulse profile at ablation, the AI coefficient can determined by solving the above equation.

Several approaches are taken to model the PI rate. The first approach is based on Beer's law where the PI rate for 2PA is proportional to the squared intensity:

$$W_{PI}^{2PA}(t) = \sigma_2 I^2(t). \tag{3.5}$$

The term σ_2 represents the 2PA cross section which can be determined experimentally and is related to the 2PA coefficient β (see Appendix B). Zhou and Ji measured β for monolayer MoS_2 at various wavelengths by creating a phototransistor and measuring the induced currents due to 2PA [56]. At 800 nm excitation, they found $\beta = 58\,\mathrm{cm}^2/\mathrm{GW}$; however, they failed to account for the etalon effect as previously demonstrated in Chapter 2. Considering the etalon effect, β can be corrected to obtain the substrate independent 2PA coefficient β' which was found to be $\beta' = 40\,\mathrm{cm}^2/\mathrm{GW}$. From β', σ_2 was found to be $8.03\times10^{25}\,\mathrm{cm\,fs/J}$. The other approaches involve the calculation of the PI rate based on the model first presented by Keldysh [26]. Recently, another set of expressions describing the photoionization rates for 2D materials were presented that also account for the proper selection rules due to interefernce between quantum trajectories for MPA [126, 127]. These theoretical calculations provide an alternative to the experimentally determined value of β which is shown to have a strong variation in literature [4, 56]. Additionally, they also account for contributions from TI. Resultantly, the four methods for predicting the PI rate are: 2PA based on experimental coefficients (Ji's Exp.) [56], the Keldysh expression for PI of bulk materials (3D KLD) [26], the Keldysh expression for PI of 2D materials (2D KLD) [126], and the Keldysh expression for 2D materials considering quantum interference (2D KLD wQI) [126].

Given the methods for modeling the PI rate, the transient internal intensity must also be accurately modeled. To this end, the intensity profile of the pulse is given by

$$I(t) = \mathrm{Re}\left[\tilde{n}(t)\right]\xi_{ZTA} I_0(t) \tag{3.6}$$

where $\tilde{n}(t)$ is the transient refractive index based on the Drude model (see Appendix B), ξ_{ZTA} is the internal intensity enhancement as given by the zero-thickness approximation (ZTA) due to interference effects with the underlying substrate, and $I_0(t)$ is the Gaussian intensity profile of the incident pulse. Given the high carrier densities generated at ablation, the temporal evolution of the refractive index will significantly affect the internal intensity seen at the end of the pulse compared to the beginning due to the presence of free carrier absorption [39]. The transient refractive index is an important property for bulk materials because it leads to the plasma mirror effect where the reflectivity drastically increases due to the presence of free carriers in the conduction band. Moreover, the current description of the intensity does not consider any spatial propagation into the material. For bulk materials, properties such as diffraction and the Kerr nonlinearity are important to consider due to their strong effects on the propagation of the pulse and its intensity. In contrast, these effects can be ignored for 2D materials due to their thinness where the increase in reflectivity and effects of self-focusing are expected to be negligible, greatly simplifying the computation of the intensity and resulting carrier density.

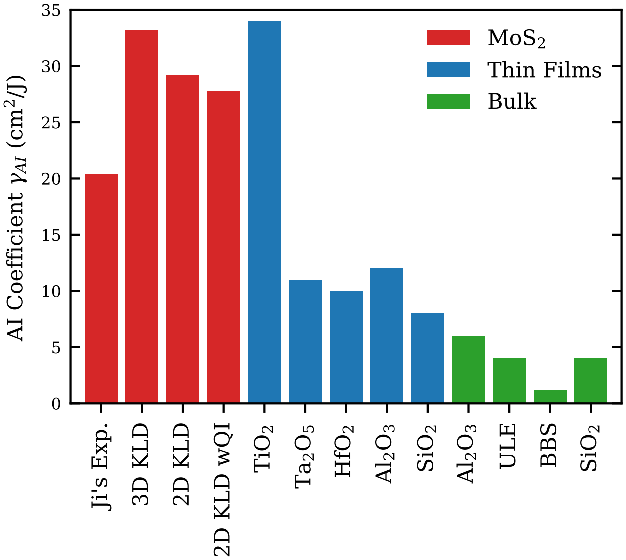

Figure 3.8: Avalanche ionization coefficients for MoS_2 and several bulk materials found in literature. All coefficients were determined by single rate equations [128–130]. ULE is a doped fused silica containing SiO_2 (92.5%) and TiO_2 (7.5%). BBS is a barium aluminum borosilicate glass.

With Equations (3.4)-(3.6), the AI coefficient γ_{AI} was determined for the four different descriptions of the PI and were found to range from 20 cm^2/J to 33 cm^2/J. The AI coefficients are summarized in Figure 3.8 along with several bulk materials found in literature. All of these AI coefficients were based on single rate equations to ensure comparability. Regardless of the PI model used, the AI coefficients for MoS_2 are generally larger by a factor of 2 or more than those for most bulk materials with TiO_2 being the only exception [129].

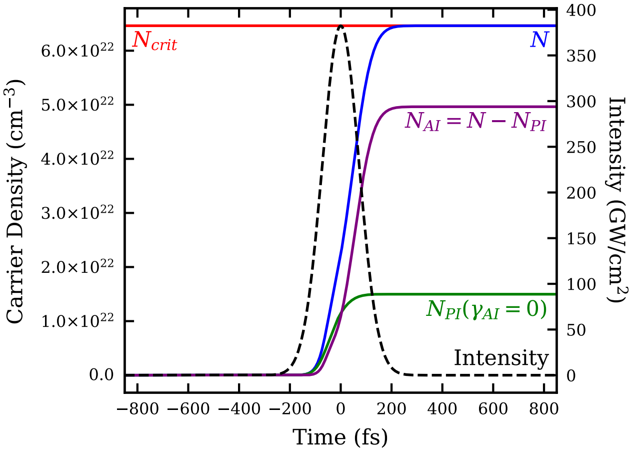

Figure 3.9: Carrier generation in monolayer MoS_2 at the ablation threshold along with the intensity profile of the pulse. The carriers density due to photoionization were calculated using the experimentally determined 2PA coefficient (Ji's Exp.).

Figure 3.9 shows the carrier density generated at ablation and their contributions from both PI and AI based on Ji's Exp. This calculation method represents the lower limit of carriers generated by AI. Nevertheless, AI generates more than three times the number of carriers than PI alone. Specifically, AI accounts for 76.8%, 98.7%, 95.9%, and 94.5% of the generated carriers for the methods Ji's Exp., 3D KLD, 2D KLD, and 2D KLD wQI, respectively (see Figure B.2). Regardless of the calculation method employed, AI is found to clearly dominate carrier generation in monolayer MoS_2. The large AI rate is not overly suprising since Auger recombination was also found to be enhanced in MoS_2 [131]. This enhancement may be due to the reduced dimensionality of 2D materials resulting in quantum confinements effects that enhance several properties of MoS_2. Further investigations utilizing microscopic theory is needed to understand this origin though.

3.5 Conclusion

In closing, several experiments were conducted to investigate the single-shot ablation of monolayer MoS_2. At fluences greater than $2F_{th}$, the ablation consisted of clean removal of material as indicated by OM, AFM, and Raman studies. At fluences below $2F_{th}$, residual material was found in the center of the hole whose height was greater than 10 nm above the surface of the monolayer flake. Based on its volume, the residual material is most likely an amorphous oxide of MoS_2. As such, ablation may result in the sublimation of MoS_2 at high fluences where as other processes such as ultrafast melting may be possible at fluences near the ablation threshold. Moreover, the effect of the incident polarization on ablation was studied which showed that the ablation threshold was independent on the orientation or ellipticity of the incident polarization, suggesting that AI is the dominate mechanism of carrier generation over 2PA. Correspondingly, the AI coefficient was determined by solving a SRE that described the carrier generation due to both PI and AI. The AI coefficient was found to vary between 20 and 33 cm^2/J for MoS_2, which is more than 2× larger than AI coefficients for most bulk materials. This large coefficient showed that more than 75% of carriers generated at ablation were due to AI alone. Similar to Auger recombination, the avalanche process could be enhanced due to quantum confinement effects induced by the reduced dimensionality of 2D materials, similar to that found for MPA based on the 2D Keldysh PI rate equation. The research presented here provides a stepping stone to further understand the effects of reduced dimensionality on strong field physics and is expected drive the innovation of future strong field devices.

CHAPTER 4: ULTRAFAST MULTI-SHOT ABLATION AND DEFECT GENERATION IN MONOLAYER MOLYBDENUM DISULFIDE

4.1 Introduction

Understanding the optical responses of two-dimensional (2D) materials under strong excitation is important. For example, semiconductor transition metal dichalcogenides (TMDs) have demonstrated strong optical nonlinearities such as second harmonic generation (SHG) [7, 132], high harmonic generation [10], saturable absorption [53, 118], and giant two-photon and three-photon absorption [4, 55, 57]. These properties make TMDs an excellent candidate for attosecond photonics, mode locking, optical limiting, and multi-photon detectors. For such applications, performance is limited by the optical damage of 2D materials so understanding the laser-induced damage under repetitive excitation in these materials is critical to improve their performance metrics. Additionally, ultrafast lasers have been demonstrated to selectively remove 2D materials for specific sizes and geometries [97]. Compared to electron-beam and photolithography which have high costs, complexity, and degraded device performance due to unwanted dopants, contaminates, and polymer residues [78], ultrafast laser ablation is a promising technique to pattern 2D materials that is *in situ*, resist-free, and maskless. For this application, knowledge of multi-shot ablation is essential to select optimal laser parameters for the best results. As the onset of ablation and damage are governed by similar physical principles, determining the ablation threshold fluences F_{th} of 2D materials as a function of the number of pulses N admitting on the same spot of the substrate is important.

Such a phenomenon, commonly referred to as incubation, is well known in pulsed laser-induced ablation and damage of bulk materials for optimizing laser processing and avoiding catastrophic damage of optical components [133]. Starting from the single-shot ablation threshold $F_{th}(1)$, the threshold fluence decreases monotonically with N until it approximately saturates at N_{sat}. For $N > N_{sat}$, F_{th} varies in a small range of fluence, defined as $F_{th}(\infty)$. If the fluence is below $F_{th}(\infty)$, ablation does not occur for any number of pulses, at least theoretically. The ratio $R \equiv F_{th}(\infty)/F_{th}(1)$ is a measure of the degree of incubation: the larger the R, the less pronounced the incubation and the more resistant the material is to radiation damage. For bulk materials, large R values were reported for HfO_2 ($R \sim 0.73$ for 50 fs and 0.84 for 1 ps) [134], and Ta_2O_5 films ($R \sim 0.67$ for 150 fs) [129].

To date, a few studies have investigated 2D materials under repetitive excitation below or near the ablation threshold. Wetzel *et al.* reported the first incubation study of femtosecond ablation of graphene but their study was purely experimental without any discussion or understanding [83]. Paradisanos *et al.* investigated the multi-shot degradation of exfoliated monolayer MoS_2 induced by ultrafast excitation [65]. They showed both the Raman A_{1g} and E^1_{2g} modes decay by 30% and 60% over 10^5 shots, when excited at 25% and 40% of $F_{th}(1)$, respectively. They attributed the Raman weakening to a decrease of the Mo-S bond density, as revealed in the formation of macroscopic holes within the monolayer that progressively increased in size upon further exposure. Despite these studies, incubation in terms of $F_{th}(N)$ for monolayer TMDs has not been investigated, nor discussed for graphene in literature. In this work, the multi-shot ablation of monolayer MoS_2 and WS_2 is studied and compared to results found in literature for graphene and several bulk materials based on a phenomenological model. Notably, MoS_2 exhibits a unique response where the threshold saturates within the first 10 pulses. Moreover, the saturation threshold is found to be about 75% of the single-shot ablation threshold and coincides with the damage threshold as measured by second harmonic generation. Finally, transmission electron microscope (TEM) images show that the onset of damage begins with the removal of clusters of atoms, resulting in dangling bonds that permanently modify the optical properties of MoS_2.

Monolayer MoS_2 films and WS_2 flakes were grown by chemical vapor deposition on c-cut sapphire (Al_2O_3) and transferred to a borosilicate glass and Al_2O_3 substrate, respectively [14]. A Coherent RegA 9000 producing 160 fs pulses at a central wavelength of 800 nm is used to conduct all ablation experiments. The repetition rate was kept constant at 307 Hz where a mechanical shutter was used to select a single or multiple pulses from the pulse train. The laser pulse energy was controlled using a continuous neutral density filter wheel or a half-wave plate with a polarizer, where a calibrated, fast photodiode was used to record individual pulse energies E. The pulses were focused on to the MoS_2 film by a 10×, 0.26 NA objective which also allowed for *in situ* imaging of the experiment. The MoS_2 sample was mounted on an Aerotech ANT three-axis motorized translation stage for precise positioning control.

4.2 Multi-Shot Ablation and Incubation

The ablation threshold F_{th} was determined by measuring the ablated hole area as a function of the incident peak fluence F where the linear extrapolation of the hole area versus $\ln(F)$ yields the threshold fluence F_{th} at zero area [92]. This area method is illustrated in Figure 4.1a for MoS_2 on a glass substrate and $N = 1$, 3, and 10 pulses. For fluences above F_{th}, the ablation produces deterministic holes with a well-defined shape, as illustrated in Figure 4.1b. As previously demonstrated in Chapters 2 and 3, this method allows the determination of the laser spot radius and F_{th} of monolayer MoS_2. Figure 4.1c shows F_{th} of MoS_2 and WS_2 for selective N up to 1000 pulses. As a comparison, Figure 4.1c also displays $F_{th}(N)$ for graphene from Ref. 83. For MoS_2, F_{th} decreases monotonically from $N = 1$ to 10 before saturating at $N_{sat} \sim 10$. For WS_2 and graphene, F_{th} quickly reduces for the first three pulses and then experiences an inflection, before leveling off at 1000 pulses. The R values for MoS_2 and WS_2 were found to be larger than the majority of bulk materials [129, 133, 135]. Only HfO_2

($R \sim 0.73$, $N_{sat} \sim 10,000$) and Ta_2O_5 ($R \sim 0.67$, $N_{sat} \sim 1000$) films were found to have comparable R values to MoS_2 and WS_2, respectively [129, 134]. Among all these materials, MoS_2 has the fastest saturation.

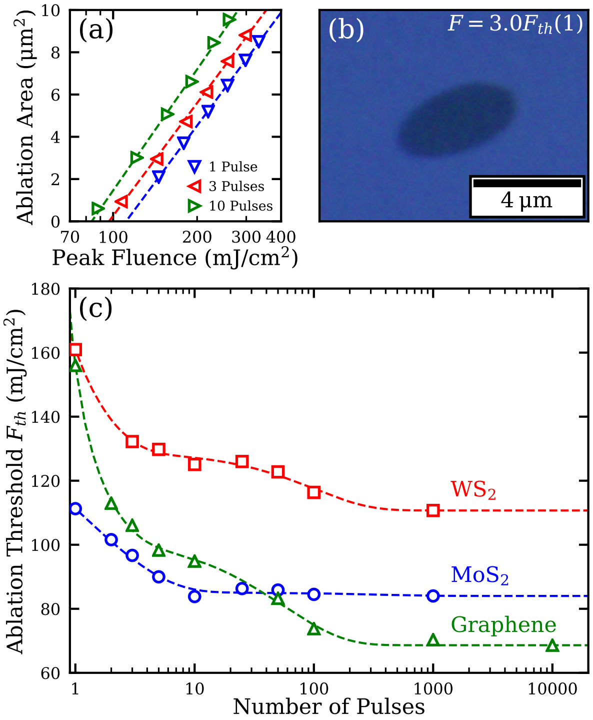

Figure 4.1: (a) Determination of the ablation threshold of MoS_2 for 1 pulse, 3 pulses, and 10 pulses. (b) Optical microscope image of an ablated hole made in a MoS_2 film due to a single pulse. (c) Multi-shot ablation thresholds for monolayer MoS_2, WS_2, and graphene [83].

To model the data, we generalize the phenomenological model introduced by Sun *et al.* to 2D materials [133]. We assume the absorption $A \equiv \Delta E/E$ and the critical surface energy density G' change over successive pulses according to

$$\begin{aligned} A(N, F') &= A_0 + \Delta A \left(1 - e^{-\beta F' N}\right), \\ G'(N, F') &= G'_0 + \Delta G' \left(1 - e^{-\gamma F' N}\right), \end{aligned} \tag{4.1}$$

where A_0 is the initial absorption, $\Delta A = A_{max} - A_0$ is its maximal change (typically positive), G'_0 is the initial critical surface energy density needed for single-shot ablation, and $\Delta G' = G'_{min} - G'_0$ is its maximal change (typically negative). The coefficients β and γ are the laser-induced rate of change of A and G' towards their respective final values. Importantly, $F' = \xi_{ZTA} F$ is the internal fluence inside the 2D materials where ξ_{ZTA} represents the intensity enhancement factor due to the interference effect of the supporting substrate and was shown to vary up to 20× among different substrates in Chapter 2. Using the internal fluence allows the determination of substrate independent coefficients. According to this model, the threshold fluence $F_{th}(N)$ is reached when the energy density deposited by the N^{th} pulse equals the critical energy density modified by the preceding $N-1$ pulses:

$$A\left(N-1, F'_{th}(N)\right) F'_{th}(N) = G'\left(N-1, F'_{th}(N)\right). \tag{4.2}$$

By combining Equations (4.1) and (4.2), the multi-shot threshold satisfies the following transcendental equation

$$F'_{th}(N) = \frac{F'_{th}(1) - \left[F'_{th}(1) - F'_{th}(\infty)\left(1 + \dfrac{\Delta A}{A_0}\right)\right]\left[1 - e^{-\gamma F'_{th}(N)(N-1)}\right]}{1 + \dfrac{\Delta A}{A_0}\left[1 - e^{-\beta F'_{th}(N)(N-1)}\right]} \tag{4.3}$$

where $F'_{th}(1) = G'_0/A_0$ is the intrinsic single-shot ablation threshold and $F'_{th}(\infty)$ is the intrinsic multi-shot ablation threshold at saturation. From Equation (4.3), R can be expressed as a simple analytical function of the maximal fractional change in critical energy $\Delta G'/G'_0$ and absorption $\Delta A/A_0$ according to

$$R \equiv \frac{F_{th}(\infty)}{F_{th}(1)} = \frac{1 + \Delta G'/G'_0}{1 + \Delta A/A_0}. \tag{4.4}$$

To obtain a large R value, Equation (4.4) indicates $\Delta G'$ and ΔA should be as close to zero as possible. Equation (4.3) is applied to fit experimental data for 2D materials and extract the fitting parameters $\Delta A/A$, β, and γ. $F'_{th}(N)$ can be determined experimentally through $F' = \xi_{ZTA} F$ where $\xi_{ZTA} = 0.63$ and 0.53 for borosilicate glass and Al_2O_3, respectively. $\Delta G'/G'_0$ is then calculated from Equation (4.4). The dashed curves in Figure 4.1 are the theoretical fits where all the fitting parameters are shown in Table 4.1 in the descending order of R. Though these materials have similar $\Delta A/A$ values, MoS_2 has the smallest $\Delta G'/G'_0$, yielding the largest R value and the smallest N_{sat} with a single decay trend in its measured $F_{th}(N)$. For WS_2 and graphene, the initial fast decay in F_{th} is due to the fast saturation of ΔA (i.e. large β), followed by a slow decay due to the slow saturation of $\Delta G'$ (i.e. small γ), leading to a larger N_{sat}. Figure 4.2 includes the multi-shot ablation thresholds for various bulk materials in literature with their fits to the original equation proposed by Sun *et al.* [133]. Their fit parameters are also summarized in Table 4.1.

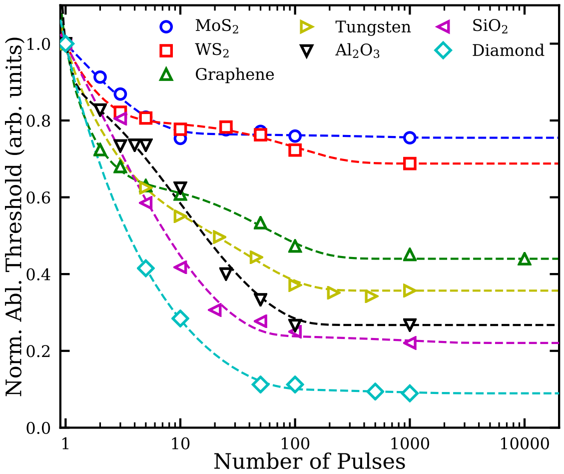

Figure 4.2: Normalized multi-shot threshold for various materials. The excitation conditions were similar for all materials (800 nm, 100∼200 fs) except for diamond (1064 nm, 10 ps) [135–138]. The thresholds are normalized to the single-shot threshold.

4.3 Single-Shot Sub-Threshold Damage and Defect Generation

Our finding is consistent with the report by Mannebach *et al.*, where they observed the transient second harmonic (SH) signal from a monolayer MoS_2 is completely recovered when it was repeatedly excited at 70% of ablation threshold [7]. As SHG is

Table 4.1: Fit parameters for Figures 4.1c and 4.2.

Materials	$\boldsymbol{R}$	$\frac{\Delta A}{A_0}$ or $\frac{\Delta \alpha}{\alpha_0}$	$\frac{\Delta G'}{G'_0}$ or $\frac{\Delta G}{G_0}$	β (cm^2/J)	γ (cm^2/J)
MoS_2	0.75	0.31	-0.013	6.3	0.052
WS_2	0.69	0.25	-0.14	13	0.16
Graphene	0.44	0.55	-0.32	15	0.35
Tungsten	0.36	0.62	-0.42	1.2	0.11
Al_2O_3	0.27	0.12	-0.70	1.5	0.026
SiO_2	0.22	0.088	-0.76	0.0015	0.089
Diamond	0.089	0.13	-0.90	0.0012	0.045

sensitive to the change in crystal structure, we performed a correlated area method and SHG experiment, in which the MoS_2 sample is exposed to a single intense pump pulse, followed by a train of weaker pulses to probe the resultant structural modification using static SHG. The result is shown in Figure 4.3 for various pump fluences below and above $F_{th}(1)$. For fluences above $F_{th}(1)$ where holes are created deterministically, the SH signal decreases with increasing fluence, indicating the SHG is due to the spatial overlap of the probe pulse with the edges of the hole. For pump fluences below $89\,\mathrm{mJ/cm^2}$, the SH intensity remained the same as that of pristine MoS_2, indicating the material is intact. Between them where no visible hole was seen, the SH signal is still below the pristine value, signifying that the film is permanently damaged. Accordingly, we define $F_{dmg} = 0.78F_{th}(1)$ as the fluence causing permanent damage to the film. This result indicates that SHG is more sensitive than the area method to detect sub-ablation damage. Importantly, comparing Figures 4.2 and 4.3 shows $F_{th}(\infty) \sim F_{dmg}$, implying as long as the pulse fluence is below F_{dmg}, monolayer MoS_2 will not be ablated for an infinite number of pulses. Similarly, the sub-ablation damage observed represents the beginning stages of incubation. For N-pulse exposure at $F_{th}(N)$, each pulse will generate sub-ablation damage, accumulatively creating a deterministic hole at its zero-area limit.

To search for further evidence of such sub-ablation damage, a MoS_2 film was transferred to a holey carbon film grid for high resolution transmission electron microscopy

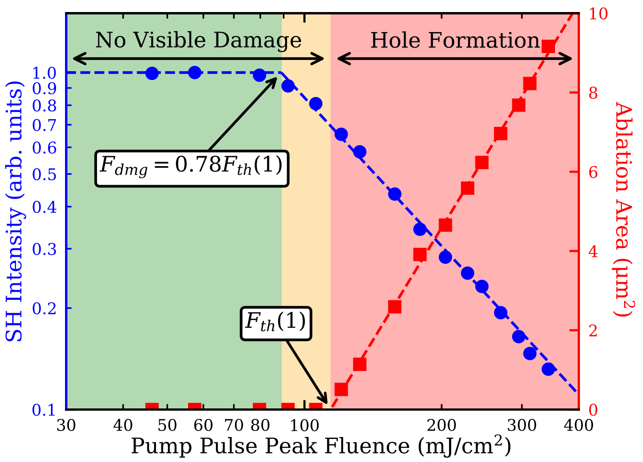

Figure 4.3: SH intensity of damage to the MoS_2 film due to a single pump pulse. The fluences in the red region creates a hole visible under an optical microscope. Fluences in the yellow region damage the film without visible evidence. No permanent damage to the film occurs for fluences highlighted in green. The probe pulse fluence is 30% of $F_{th}(1)$. The left axis is logarithmic, and the right axis is linear.

(HR-TEM). The left image in Figure 4.4 shows a HR-TEM image of pristine MoS_2 where the dark spots represent the sulfur atoms and the bright spots are the molybdenum atoms. The images on the right show MoS_2 exposed to a single pulse at $F = 0.93F_{th}(1)$ where clusters of atoms ranging up to a few nanometers across are removed without destroying the overall integrity of the film. Figure 4.4 reveals that such sub-ablation damage is stochastic in nature where voids appear sporadic with random sizes and shapes within the exposed area. This is in sharp contrast to the deterministic ablated holes seen in the area method (Figure 4.1a). The nano-voids in Figure 4.4 show a decrease of roughly 5% in atomic density, which translates to a 10% reduction in SH intensity. Figure 4.3, however, indicates a 20% reduction in SH intensity, implying the presence of other defects in addition to the nano-voids. We note that Figure 4.4 lacks the resolution to resolve native and laser-induced point defects.

To reveal more information regarding these defects, we performed various optical spectroscopies on pristine MoS_2 and MoS_2 exposed to a single pulse at $0.83F_{th}(1)$.

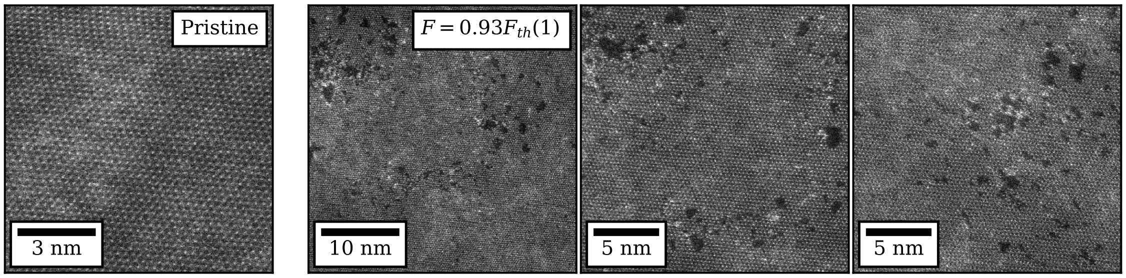

Figure 4.4: (left) HR-TEM of pristine monolayer MoS_2. (right) Damaged MoS_2 film exposed to a pulse with a fluence $F = 0.93F_{th}(1)$.

Figure 4.5a shows the SH polar profile for pristine MoS_2 by rotating the incident polarization while recording the SH signal at x- and y-polarizations. The data follows the theoretical curve (solid line) for this method, indicating excellent crystallinity [7]. The polar profile at the center of the damaged region is shown in Figure 4.5b. As the damaged region is significantly smaller than the probe pulse spot size, the SH signal is dominated by the surrounding pristine MoS_2 where a 4-fold symmetry is clearly resolved. Compared to Figure 4.5a, however, the depolarization (reduced contrast) is evident where the maximal SH intensity reduces by ~20% and the minimum never drops completely to zero. A more pronounced depolarization can be seen for MoS_2 exposed to $2F_{th}(1)$ where more of the SH signal is from the edge of the hole (see Appendix C). In addition to SHG, Figures 4.5c-4.5d show the PL and Raman spectra recorded at the center of the damaged spot. As a reference, pristine spectra are also shown in blue. The line profile of the PL peak intensity and center energy across the damaged spot is presented in Figure 4.5e, showing an obvious intensity reduction of ~25% and blue shift in the PL after exposure. Similar results were also recorded for the Raman line scan as shown in Figure 4.5f, where the intensity of both the E^1_{2g} and A_{1g} peaks are reduced ~25% in the damage region of the MoS_2 film. Additionally, the E^1_{2g} mode experiences a maximal redshift of $1.6\,\text{cm}^{-1}$ while the A_{1g} peak shows a maximal blue shift of $0.9\,\text{cm}^{-1}$.

For single pulse exposure at $0.83F_{th}(1)$, these nano-voids revealed by HR-TEM

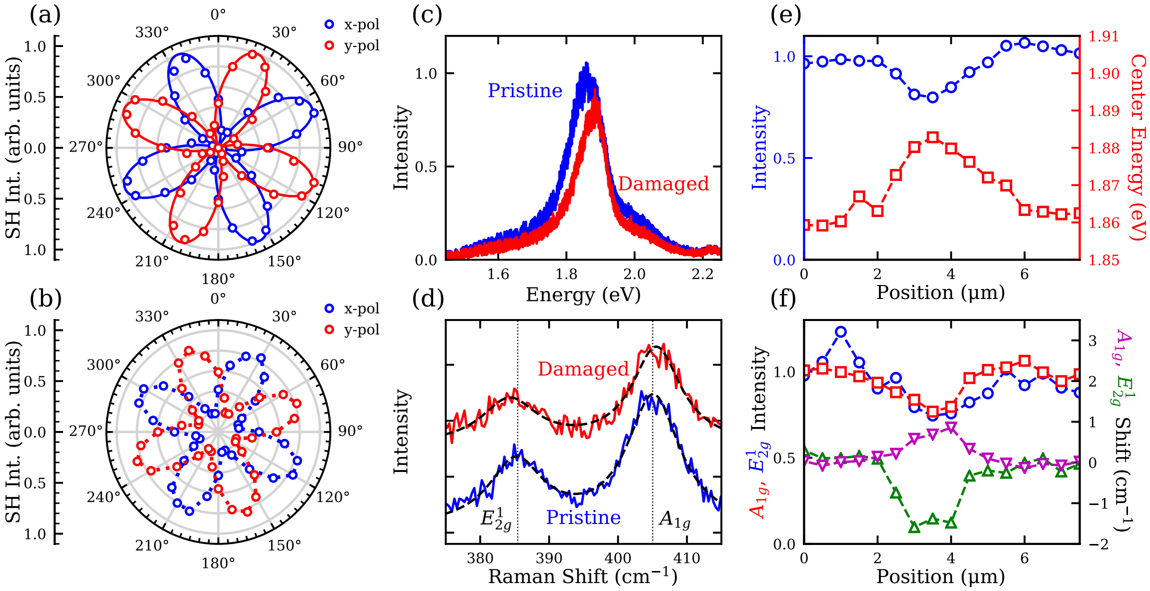

Figure 4.5: Second harmonic polar profile of (a) pristine MoS_2 and (b) damaged MoS_2 by a pulse of $F = 0.83F_{th}(1)$. (c) Photoluminescence and (d) Raman spectra of pristine and damaged MoS_2. (e) Photoluminescence and (f) Raman line scans across damaged MoS_2. The second harmonic polar plot in (b) and the PL and Raman scans in (c)-(f) were all recorded for the same damaged spot.

only account for less than a 5% reduction in the number of atoms which alone is not enough to explain the near 20%-25% drop in SH, PL, and Raman intensities. The fact that the SH intensity in the polar plot never drops to zero is similar to that seen for polycrystalline MoS_2, suggesting that the local crystal lattice has become disordered [139]. Such disorder most likely happens at the edges of the nano-voids, which will contribute to the reduction of the maximal SH intensity in the polar plot. In addition, several types of vacancies associated with S and Mo atoms are likely present around the edges of the nano-voids or in the MoS_2 film after exposure. The dangling bonds associated with these vacancies are known to introduce mid-gap states in the band structure of MoS_2 which could strongly quench the PL intensity and cause a blue shift similar to that observed here [140–144]. Such mid-gap states could increase light absorption ($\Delta A/A_0$) of successive laser pulses during incubation, leading to a reduction in the threshold fluence [145]. Additionally, the lateral strain introduced locally by the defects and lattice disorder can cause the Raman intensities to decrease [146, 147]. The blue shift in the A_{1g} and red shift in the E_{2g}^{1} peaks could be explained by a combination of p-doping from the presence of Mo-O bonds [76, 148] and strain introduced by laser-induced defects and lattice disorder [143, 146].

4.4 Conclusion

In summary, we show that MoS_2 and WS_2 have weak incubation effects. A modified phenomenological model was applied to describe the incubation behavior of MoS_2, WS_2, and graphene with good agreement, revealing that MoS_2 is the most resistant to laser-induced bond softening, which is foundational to its weakest incubation ($R \sim 0.75$) and fastest saturation ($N_{sat} \sim 10$). Moreover, static SH measurements reveal the threshold for sub-ablation damage to be $F_{dmg} = 0.78 F_{th}(1)$ for MoS_2, below which MoS_2 remains intact for many pulses. For fluences slightly above F_{dmg}, incubation starts with laser generated vacancies which introduce mid-gap states that quench the PL and increases subsequent pulse absorption. Such vacancies also introduce strain and disorder in the lattice that weaken the Raman and SH intensities. Successive pulse exposure leads to nano-voids with random sizes and shapes, which grow in size with subsequent pulses, until a deterministic ablation hole with a theoretical zero area is reached. At pulse fluences between F_{dmg} and $F_{th}(1)$, nano-voids could form during the first shot, requiring fewer number of pulses to reach the onset of ablation. The fast saturation and weak incubation establish MoS_2 as an attractive material for high-throughput laser processing and strong field devices.

CHAPTER 5: ADDITIONAL EXPERIMENTS AND CHALLENGES

Chapters 2, 3, and 4 provide important foundational knowledge for the ultrafast ablation of monolayer MoS_2 and TMDs in general. During the course of this research several other experiments were conducted in addition to those discussed in the previous chapters. The initial findings from some of these experiments necessitate further investigations that are beyond the scope of this dissertation; however, the potential impact of these experiments could be significant and warrant discussion. Correspondingly, this chapter is broken into three short sections discussing the initial findings of three of these preliminary studies and to promote further investigation.

5.1 Double Pulse Ablation

The previous studies either involved ablation due to a single pulse or a stream of pulses whose separation is longer than most lifetimes found within the MoS_2 monolayer. As a result, most transient processes during ablation had to be handled theoretically such as the refractive index or free carrier absorption (FCA). To probe these transient effects, time-resolved studies have to be conducted. To date, a few time-resolved experiments involving intense excitation have been performed regarding TMDs but none of these studies investigate fluences large enough to cause ablation [7, 149–152]. On the contrary, several time- and spatial-resolved studies have been conducted for bulk materials at ablation, revealing interesting material responses at breakdown including Coulomb explosion, phase transitions, and enhanced double pulse ablation to just name a few [8, 9, 102, 103, 122, 153–165]. Correspondingly, a time-resolved double pulse experiment was designed and performed for monolayer MoS_2, WS_2, and graphene.

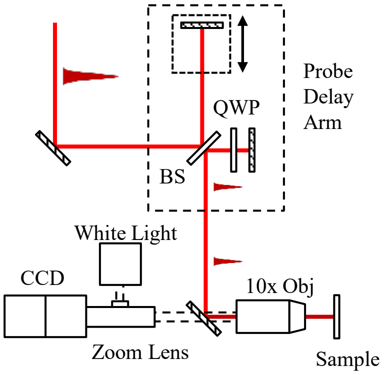

Figure 5.1: Schematic for double pulse ablation.

Figure 5.1 shows a diagram for a double pulse ablation experiment. A single pulse is split using a 50/50 beam splitter (BS) along two arms, similar to that in a Michelson interferometer. One arm consists of a mirror aligned at normal incidence set on a delay stage to control the time separation between the two pulses. The second arm consists of a stationary mirror and a quarter-wave plate (QWP) which rotates the polarization by 90° after a double pass through the QWP. Rotating the polarization is important to avoid interference effects at the surface of the 2D material when the pulses are temporally overlapped. The translation stage was capable of producing delays greater than ±400 ps. The fluence for each pulse was set to be below the two pulse ablation threshold $F_{th}(2)$. Setting this fluence is important to ensure the ablation area goes to zero for large delays.

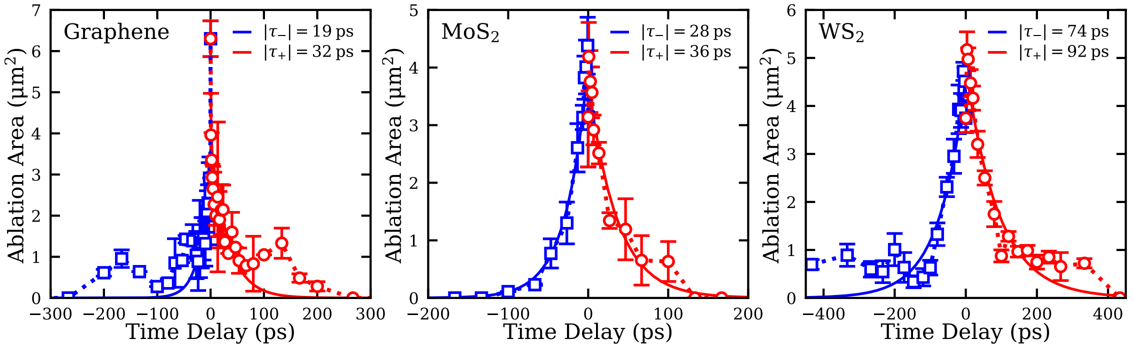

Figure 5.2: Double pulse ablation of graphene, MoS$_2$, and WS$_2$.

Using this setup, the ablation area can be recorded as a function of the pulse separation as shown in Figure 5.2 for graphene, MoS_2, and WS_2. The data in red represents positive delays while the data in blue marks negative delays. Across all three 2D materials, the ablation area decreases towards zero at long delays as expected since the fluence of each pulse is below $F_{th}(2)$. For MoS_2 and WS_2, the decay in the ablation threshold agrees well with a simple exponential decay given by the solid lines in Figure 5.2. This result can be described using a SRE similar to that in Equation (3.2) given by

$$\frac{dN}{dt} = W_{PI}(t) + \gamma_{AI} I(t) N - \frac{N}{\tau} \tag{5.1}$$

where the new term with τ describes the relaxation of carriers. If the pulse separation Δt is greater than the pulse duration τ_{FWHM}, the carrier density is approximately given by

$$N(\Delta t) \cong N_0 \left[1 + \exp\left(\frac{f\gamma_{AI}F}{2} - \frac{\Delta t}{\tau} \right) \right] \exp\left(\frac{f'\gamma_{AI}F}{2} - \frac{\tau_{FWHM}}{\tau} \right) \tag{5.2}$$

where N_0 is the initial carriers created by MPI, and f and f' represent the fraction of the fluence that contributes to AI [164]. The above equation yields an exponential decay in terms of Δt which qualitatively describes the trend seen for MoS_2 and WS_2.

There are multiple features in the double pulse ablation of graphene that are unique compared to the results for MoS_2 and WS_2. First, graphene exhibits a very strong peak at zero time delay. This peak could be an indicator that the optical breakdown of graphene occurs through Coulomb explosion. Time of flight experiments measuring the ions ejected from graphite due to ultrafast ablation show that the optical breakdown of graphene is due to Coulomb explosion [102, 103]. In particular, a similar double pulse experiment was performed for graphite which showed that the ion yield increased substantially when the two pulses were overlapped temporaly. In fact, the ion yield nearly drops to zero with a pulse separation of less than 200 fs [102, 103]. Consequently, the strong peak observed for the double pulse ablation of graphene may also indicate the presence of Coulomb explosion.

The second unique aspect observed for graphene in Figure 5.2 are the humps observed at time delays of about ±50 ps and ±150 ps which are not present in MoS_2 and WS_2. These resonances could potentially describe some unique carrier dynamics. In particular, graphene exhibits many remarkable properties when excited by femtosecond pulses. Once carriers are generated, they rapidly relax through strong electron-phonon interactions, leading to a hot lattice temperature. This energy is typically dissipated through lateral diffusion in the graphene film; however, given a sufficiently strong optical excitation, energy can be dissipated via out-of-plane acoustic phonons where the energy is transferred to the underlying substrate or the air [166, 167]. In fact, one group reported the generation of sound through opto-thermo-acoustic waves from graphene when excited by a femtosecond pulse [167]. These phonons were found to effect the reflectivition and and transmission properties of graphene. Similar pump probe experiments showed oscillations in both the reflectivity and transmissivity of graphene for time delays of 50 ps and larger [166]. Given the intense excitation used in these experiments, the effects of acoustic phonons on the ablation of graphene may be significant and give rise to the humps observed in the double pulse ablation data.

In summary, the results presented in Figure 5.2 are only preliminary. Further experiments are needed to understand the complex carrier dynamics that occur at ablation. Importantly, the double pulse ablation of MoS_2 and WS_2 present an opportunity to expand upon the SRE from Chapter 3 and further probe the effects or free carrier absorption and impact ionization in TMDs. Additionally, the current SRE in Equation (5.1) could be used to extract effective lifetimes for carriers. Moreover, effects such as band gap renormalization are expected to be present within this experiment. Both MoS_2 and WS_2 exhibit giant band gap renormalization and columb screening effects due to femtosecond excitation [150–152]. Specifically, bilayer WS_2 has shown a band gap reduction of 0.5 eV and complete screening of the exciton when excited by 515 nm pulses [150]. These previous experiments only observed these effects due to 1PA excitation. The double pulse ablation gives the opportunity to identify these same processes for nonlinear excitation. Furthermore, this study may provide the first experimental evidence of Coulomb explosion in graphene. To date, only molecular dynamic simulations have been performed to investigate Coulomb explosion in graphene [119]. Additional experiments investigating the ablation threshold as a function of pulse separation will provide complementary information to that previously presented and may be easier to model. Nevertheless, further insight and understanding can be obtained from these time-resolved experiments, potentially revealing unique physical processes that result from the reduced dimensionality of these materials.

5.2 Ultrafast Laser Thinning

Most of the work presented here is focused on the physical mechanisms leading to the optical breakdown of MoS_2. While this knowledge is important for understanding the limitations of this material, little has been discussed regarding immediate applications. Chapter 2 does discuss in some detail the application of ultrafast ablation to pattern MoS_2 for different devices, though this is just one application. One of the most studied processes is the laser thinning of MoS_2 [80, 86, 104, 105, 168, 169]. While this is another laser patterning application, the focus is on producing high-quality monolayers for devices from multi-layer MoS_2. While these studies show promise, there are some noticeable issues that need resolved. Many studies reveal that the surface roughness of laser-thinned monolayer MoS_2 is two to three times higher compared to a pristine monolayer and that the surface is covered by amorphous particles [80, 104, 168, 169]. Although these particles can be moved or removed, they can inadvertently effect the optical and electrical properties of the monolayer. Additionally, all studies to this point have utilized a continuous-wave (CW) source which relies on material removal via thermal heating and sublimation of the MoS_2 layers. This process easily allows for oxidation of the resultant monolayer [104, 105, 168]. To avoid

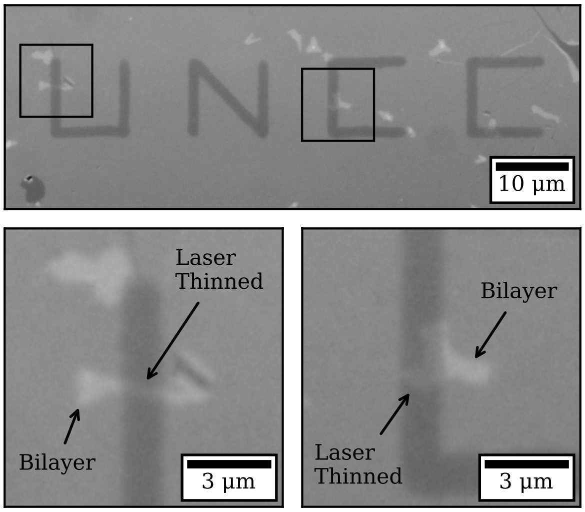

Figure 5.3: Incidental ultrafast laser thinning of bilayer MoS_2 during laser patterning trials.

such oxidation, the laser power has to be reduced which lowers the patterning rate, or the thinning process has to be conducted in a vacuum environment.

The use of an ultrafast source may be able to circumvent some of these issues. During the laser pattering experiments presented in Chapter 2, ultrafast laser thinning was accidentally demonstrated for bilayer MoS_2 as shown in Figure 5.3. The bilayers can easily be identified under an optical microscope due to their strong change in contrast [170]. There are multiple potential advantages to the use of an ultrafast source. First, with the proper selection of power level, the optical breakdown can be governed by electronic processes instead of thermal which could limit the effects of oxidation and the formation of amorphous particles. Additionally, if 800 nm pulses are used, laser thinning to a monolayer will be self-terminating based on the difference in band structure. Current CW laser thinning studies claim that monolayer formation is self-terminating due to the substrate acting as a heat sink for the final MoS_2 layer where as heat coupling between layers is minimal since the layers are held together by van der Waals forces [80, 168]. The results from Chapter 2 and thermal boundary conductance studies contradict this exact claim, proving that little thermal energy is transferred to the underlying substrate [94, 95]. Band structure calculations and measurements reveal that multilayer MoS_2 has an indirect band gap of 1.2 eV while monolayer MoS_2 has a direct band gap with an optical transition at 1.8 eV [3]. As a result, monolayer formation should be self-terminating due to the transition from 1PA to 2PA for multi-layer and monolayer MoS_2. Ultimately, a comparative study between CW and ultrafast laser thinning needs to be conducted to test these claims.

5.3 Ablation of As-Grown MoS_2

Chemical vapor deposition (CVD) is an important tool to produce monolayer 2D materials with graphene and MoS_2 being the two biggest examples. Monolayer graphene and MoS_2 can also be obtained by mechanical exfoliation from bulk crystals but this process requires trial and error and often results in multi-layer films with a few regions consisting of monolayers. For this reason, CVD grown MoS_2 was used for all studies since CVD provides the best method for mass producing monolayer MoS_2 films; however, all films that were grown were transferred from their host substrate to a new substrate for experiments. This transfer process can harm the MoS_2 monolayer as shown in Figure 1.3 where cracks are visible in the transferred monolayer flake. On occasion, the transfer process can completely destroy the monolayer flakes as shown in Figure 5.4. Subsequently, the transfer process can induce defects that degrade the optical and electrical properties of the 2D material and limit its performance for device applications. The best solution would be to grow the 2D material directly on the intended substrate. For example monolayer MoS_2 has been successfully grown on both Al_2O_3 and SiO_2/Si substrates. Out of these two substrates, the SiO_2/Si substrate is a popular choice for FET devices. Given that, studying the ablation of as-grown MoS_2 is equally, if not more important than transferred MoS_2.

The preliminary results for the ablation of as-grown MoS_2 flakes were surprisingly different than flakes that were transferred. Figure 5.5 shows OM images and scanning electron microscope (SEM) images of ablation of as-grown flakes. Initially, OM images

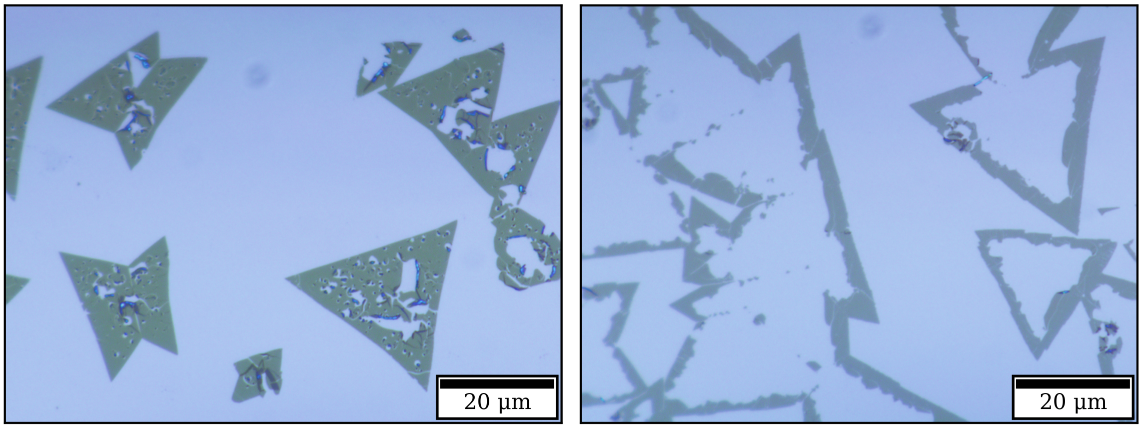

Figure 5.4: Failed transfer of CVD grown monolayer MoS_2 (left) and WS_2 (right).

reveal a clean hole similar to those observed for transferred flakes in Figure 3.1 yet SEM images reveal that the holes themselves contained residual material. Figure 5.6 summarizes several forms of characterization including OM, SEM, AFM, and Raman spectroscopy for a single hole. Similar to the results in Figure 3.4 for a transferred MoS_2 flake, AFM measurements reveal that the residual material is significantly taller than height of the flake itself. Raman measurements of the hole were also similar in that the peaks associated with MoS_2 reduce to zero while no other peaks were recorded for the residual material in the center of the hole. Following a similar line of logic, the residual material is believed to be an amorphous molybdenum suboxide just as in Chapter 3.

More importantly, this residual material was there regardless of the incident fluence. SEM and AFM images of the surrounding substrate show a high density of the seed sites that serve as precursors for the flakes to grow. It is believed that these precursors significantly contribute to the formation of the residual material after ablation. Further investigation of this residual material though needs to be conducted if as-grown flakes and films are to be used to MoS_2-based devices.

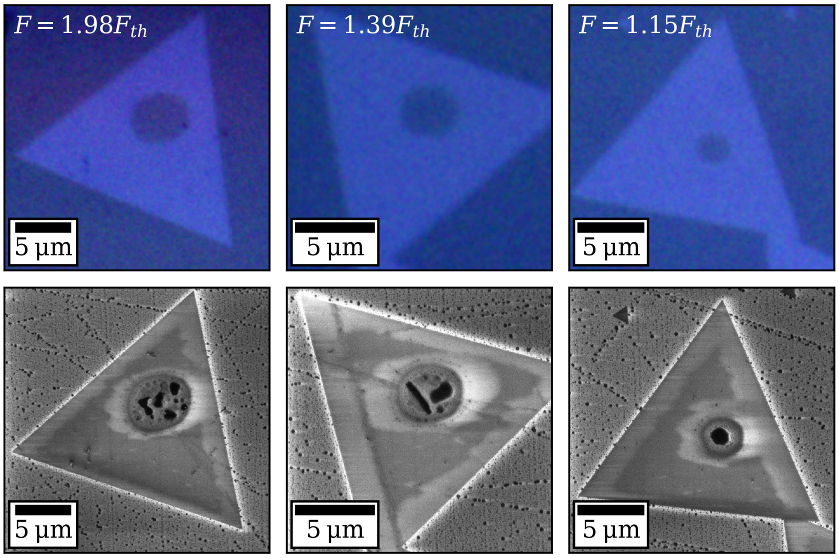

Figure 5.5: OM images (top row) and SEM images (bottom row) of ultrafast ablation of as-grown monolayer MoS_2 flakes on Al_2O_3.

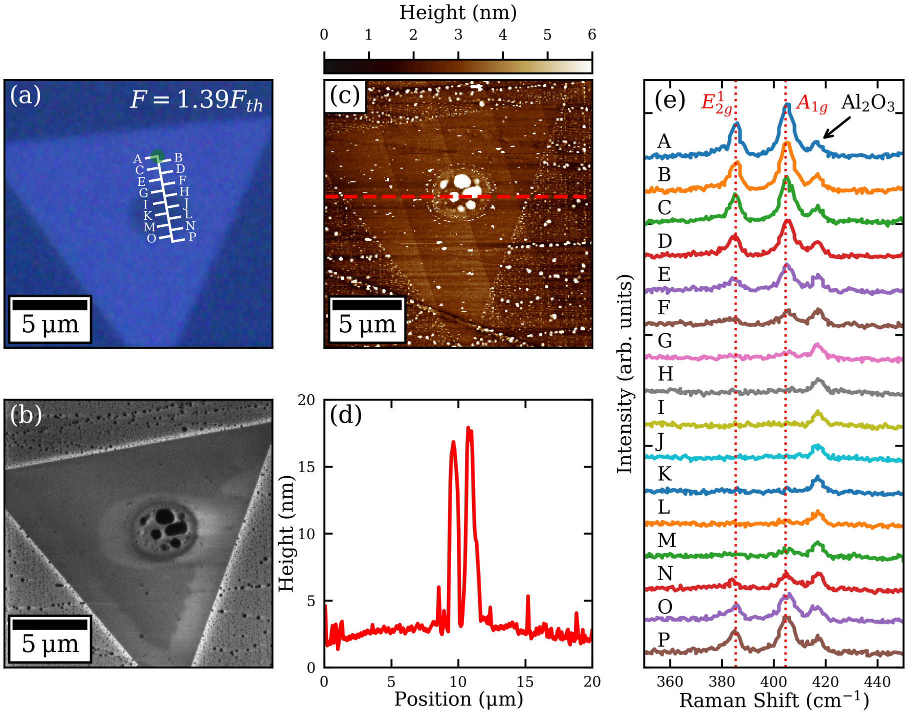

Figure 5.6: (a) OM, (b) SEM, and (c) AFM images of a single ablation hole in a MoS_2 flake on Al_2O_3. (d) AFM height profile as marked in (c). (e) Raman line scan across the hole as indicated in (a).

CHAPTER 6: CONCLUSIONS

Transition metal dichalcogenides are a unique class of 2D materials that posses special properties due to their reduced dimensionality. Specifically, semiconductor TMDs such as monolayer MoS_2 are of particular interest due to their direct band gap, strong excitonic resonances, and exceptional nonlinear optical properties that make them ideal candidates for future nano- and optoelectronic devices. Therefore, investigating the optical limitations and breakdown of MoS_2 is imperative to maximize the performance of these TMD-based devices. Additionally, understanding the ultrafast ablation of these materials is important in order to optimize the laser patterning process as a viable route for rapid device production. Moreover, MoS_2 provides an opportunity to study the effects of reduced dimensionality on strong field physics. To that end, this dissertation provides the first in-depth research on the ultrafast ablation of monolayer MoS_2. The studies included here provide insight on the impact of the underlying substrate, the role of avalanche ionization, and the process of defect generation in the intense ultrafast excitation of MoS_2. Finally, this dissertation concludes with future projects that will further reveal the underlying physics governing the intense excitation of TMDs.

6.1 Summary

For the first time, a systematic study on the role of the substrate in the ultrafast ablation of 2D materials was conducted. Experiments revealed that the ablation threshold can vary by nearly 20× across several substrates for MoS_2. This variation was found to be due to the optical interference produced at the surface of the substrate within the TMD. Simple analytical expressions were derived that showed that the optical excitation is independent of the 2D material within the zeroth order. With these expressions, substrates can easily be designed to engineer the robustness of 2D materials by either raising or reducing the ablation threshold through destructive or constructive interference, respectively. As demonstrated, two DBR substrates were designed that yielded total constructive or destructive interference within the MoS_2 monolayer where the threshold differed by more than 40×. With the large reduction in threshold produced by the one DBR susbtrate, high-speed laser patterning using a low power ultrafast oscillator was easily demonstrated where feature sizes less than 250 nm were achieved with modest focusing conditions. Furthermore, the excellent scaling with the etalon for both single-shot and line-scan ablation revealed that the ablation process is adiabatic, meaning that negligible thermal energy is transferred to the underlying substrate during ablation. This work highlights the importance of the substrate in the optical breakdown of MoS_2 and 2D materials in general and establishes femtosecond ablation as a viable route to pattern 2D materials.

With the role of the substrate clarified, the underlying physical mechanisms of ablation were studied for monolayer MoS_2. The ablation threshold was found to be insensitive to the orientation of the flake or incident polarization of the pulse. Both these results indicated that avalanche ionization (AI) plays a significant role in the optical breakdown of MoS_2. With the combination of absorption measurements and theoretical modeling, the AI coefficient was found to be greater than $20\,\mathrm{cm}^2/\mathrm{J}$, which is two times larger than those found for those bulk materials. In fact, the model used here showed that more than 75% of the carriers generated at ablation were due to AI, providing evidence that the avalanche process is also enhanced in these 2D materials. In addition, atomic force microscope images revealed the presence of residual material after ablation which is believed to be an amorphous molybdenum suboxide. This residual material proves that sublimation is not the only mechanism governing material removal at ablation. Other processes such as ultrafast melting, oxidation, and evaporation can occur.

Although understanding the ultrafast ablation due to a single pulse is important, most cases of laser induced-damage or patterning occur due to repetitive excitation. With this process in mind, the multi-shot ablation and the role of incubation in MoS_2 was also investigated. The study showed that MoS_2 has weak incubation effects where the threshold only reduces by 25% and saturates within the first 10 pulses when under repetitive intense excitation. Modeling revealed that the record robustness of MoS_2 is due to the small reduction in critical energy needed for ablation, where the threshold only reduces due to the increased absorption from laser-induced defects. Transmission electron microscope images revealed that the onset of damage occurs through the formation of nano-voids that disorder the local crystal lattice. The dangling bonds created by these nano-voids along with the presence of vacancies result in mid-gap states that increase the absorption for subsequent pulses and act as quench states as observed in the photoluminescence spectra of damaged MoS_2. Importantly, the fast saturation and weak incubation establish MoS_2 as attractive material for future strong field devices.

6.2 Future Work

The work presented here provides fundamental insight into the strong field physics governing the ablation of monolayer MoS_2 and lays the foundation for further research endeavors. Many projects, including experimental, theoretical, and practical, can directly build upon this work. Experimentally, only the ultrafast ablation of transferred, CVD-grown MoS_2 was systematically investigated. As a result, the role of native defects has not been studied. Literature has shown that natural, CVD-grown, and PVD-grown monolayer MoS_2 all possess different defects and defect densities [171]. Repeating several previous experiments for other variations of MoS_2 monolayers will reveal the impact of these native defects during ablation.

Additionally, only the ablation by 800 nm excitation was thoroughly studied. The nonlinear absorption and optical breakdown due to other wavelengths can reveal new information. Some groups have reported on the two-photon and three-photon absorption coefficients in MoS_2 but they failed to include the etalon effect and the contribution of second harmonic generation in their analysis [4, 56, 57]. As a result, accurate measurements of these nonlinear coefficients remain elusive. Moreover, discussion regarding tunneling ionization in MoS_2 is severely lacking. MoS_2 has demonstrated strong high-harmonic generation which is believed to be mediated by tunneling ionization [10]; however, the 2D Keldysh expression predicts that the tunneling ionization is mitigated in 2D materials [126]. Therefore, experiments designed to probe tunneling ionization need to be conducted which can be done by investigating the intense excitation of MoS_2 due to mid-IR pulses to reduce the contribution of multi-photon absorption. Similarly, the ablation of other TMDs and 2D materials such as $MoSe_2$, WSe_2, WS_2, and h-BN can offer similar insight due to their differing band gaps.

In addition to other wavelengths, varying the pulse duration can also highlight different ionization mechanisms. The pulse durations utilized in this study were all around 160∼170 fs. Literature suggests that avalanche ionization will strongly contribute for pulse durations greater than 100 fs [38]. By pushing to pulse durations below 50 fs, one can attempt to isolate multi-photon ionization in the breakdown of 2D materials. Conversely, if the avalanche process is enhanced in 2D materials, then a weak pulse duration dependence may be observed in the ablation of MoS_2.

Theoretically, the single rate equation is a great starting point to model carrier generation, though it greatly simplifies the avalanche process into a single coefficient. Other modeling methods such as the two-temperature model or multiple rate equations can give further insight regarding the role of avalanche at breakdown. For example, a multiple rate equation model will allow characterization of free carrier absorption and impact ionization independently. Combined with time resolved studies such as double pulse ablation and degenerate pump-probe experiments, both free carrier absorption and impact ionization can be described completely, both theoretically and experimentally. Moreover, a multiple rate equation model will be able describe the contribution of the laser-induced defects observed during the multi-shot ablation of MoS_2. These defect states introduce mid-gap transitions that can enhance both the absorption and avalanche process. Moreover, the role of the exciton has not be discussed regarding the optical breakdown of MoS_2. A multiple rate equation model can account for both the defect states and the exciton transition.

Practically, ultrafast laser thinning and patterning experiments remain largely unexplored. As discussed in Chapter 5.2, ultrafast sources may be able to bypass some of the drawbacks seen in CW laser thinning applications. Moreover, while the ultrafast laser patterning of MoS_2 was demonstrated, the electrical and optical performance of patterned MoS_2 has yet to be investigated for device applications. Ultimately, to prove that ultrafast laser patterning is a viable route for rapid production of MoS_2-based devices, a transistor or similar device needs to be created from a laser patterned MoS_2 film and tested to see if its performance is comparable with similar MoS_2-based devices seen in literature. These projects will help push the boundaries of strong field devices, enabling miniaturization and advancement of future technologies.

REFERENCES

[1] K. S. Novoselov, A. K. Geim, S. V. Morozov, D. Jiang, Y. Zhang, S. V. Dubonos, I. V. Grigorieva, and A. A. Firsov, "Electric Field Effect in Atomically Thin Carbon Films," Science **306**, 666 LP – 669 (2004).

[2] Q. H. Wang, K. Kalantar-Zadeh, A. Kis, J. N. Coleman, and M. S. Strano, "Electronics and optoelectronics of two-dimensional transition metal dichalcogenides," Nature Nanotechnology **7**, 699–712 (2012).

[3] M. Chhowalla, H. S. Shin, G. Eda, L.-J. Li, K. P. Loh, and H. Zhang, "The chemistry of two-dimensional layered transition metal dichalcogenide nanosheets," Nature Chemistry **5**, 263–275 (2013).

[4] X. Li and H. Zhu, "Two-dimensional MoS_2: Properties, preparation, and applications," Journal of Materiomics **1**, 33–44 (2015).

[5] B. Radisavljevic, A. Radenovic, J. Brivio, V. Giacometti, and A. Kis, "Single-layer MoS_2 transistors," Nature Nanotechnology **6**, 147 (2011).

[6] S. Bertolazzi, J. Brivio, and A. Kis, "Stretching and Breaking of Ultrathin MoS_2," ACS Nano **5**, 9703–9709 (2011).

[7] E. M. Mannebach, K.-A. N. Duerloo, L. A. Pellouchoud, M.-J. Sher, S. Nah, Y.-H. Kuo, Y. Yu, A. F. Marshall, L. Cao, E. J. Reed, and A. M. Lindenberg, "Ultrafast Electronic and Structural Response of Monolayer MoS_2 under Intense Photoexcitation Conditions," ACS Nano **8**, 10734–10742 (2014).

[8] C. V. Shank, R. Yen, and C. Hirlimann, "Femtosecond-Time-Resolved Surface Structural Dynamics of Optically Excited Silicon," Physical Review Letters **51**, 900–902 (1983).

[9] C. V. Shank, R. Yen, and C. Hirlimann, “Time-Resolved Reflectivity Measurements of Femtosecond-Optical-Pulse-Induced Phase Transitions in Silicon,” Physical Review Letters **50**, 454–457 (1983).

[10] H. Liu, Y. Li, Y. S. You, S. Ghimire, T. F. Heinz, and D. A. Reis, “High-harmonic generation from an atomically thin semiconductor,” Nature Physics **13**, 262–265 (2017).

[11] O. V. Yazyev and A. Kis, “MoS_2 and semiconductors in the flatland,” Materials Today **18**, 20–30 (2015).

[12] Y.-H. Lee, X.-Q. Zhang, W. Zhang, M.-T. Chang, C.-T. Lin, K.-D. Chang, Y.-C. Yu, J. T.-W. Wang, C.-S. Chang, L.-J. Li, and T.-W. Lin, “Synthesis of Large-Area MoS_2 Atomic Layers with Chemical Vapor Deposition,” Advanced Materials **24**, 2320–2325 (2012).

[13] M.-L. Tsai, S.-H. Su, J.-K. Chang, D.-S. Tsai, C.-H. Chen, C.-I. Wu, L.-J. Li, L.-J. Chen, and J.-H. He, “Monolayer MoS_2 Heterojunction Solar Cells,” ACS Nano **8**, 8317–8322 (2014).

[14] W.-F. Hsu, L.-S. Lu, P.-C. Kuo, J.-H. Chen, W.-C. Chueh, H. Yeh, H.-L. Kao, J.-S. Chen, and W.-H. Chang, “Monolayer MoS_2 Enabled Single-Crystalline Growth of AlN on Si(100) Using Low-Temperature Helicon Sputtering,” ACS Applied Nano Materials **2**, 1964–1969 (2019).

[15] H. Yu, M. Liao, W. Zhao, G. Liu, X. J. Zhou, Z. Wei, X. Xu, K. Liu, Z. Hu, K. Deng, S. Zhou, J.-A. Shi, L. Gu, C. Shen, T. Zhang, L. Du, L. Xie, J. Zhu, W. Chen, R. Yang, D. Shi, and G. Zhang, “Wafer-Scale Growth and Transfer of Highly-Oriented Monolayer MoS_2 Continuous Films,” ACS Nano **11**, 12001–12007 (2017).

[16] Q. Wang, N. Li, J. Tang, J. Zhu, Q. Zhang, Q. Jia, Y. Lu, Z. Wei, H. Yu, Y. Zhao, Y. Guo, L. Gu, G. Sun, W. Yang, R. Yang, D. Shi, and G. Zhang, “Wafer-Scale Highly Oriented Monolayer MoS_2 with Large Domain Sizes,” Nano Letters (2020), 10.1021/acs.nanolett.0c02531.

[17] C. Lee, H. Yan, L. E. Brus, T. F. Heinz, J. Hone, and S. Ryu, “Anomalous Lattice Vibrations of Single- and Few-Layer MoS_2,” ACS Nano **4**, 2695–2700 (2010).

[18] S.-L. Li, H. Miyazaki, H. Song, H. Kuramochi, S. Nakaharai, and K. Tsukagoshi, “Quantitative Raman Spectrum and Reliable Thickness Identification for Atomic Layers on Insulating Substrates,” ACS Nano **6**, 7381–7388 (2012).

[19] P. E. McGuff, D. Bushnell, H. S. Soroff, and R. A. Deterling, Jr, “Studies of the surgical applications of laser (light amplification by stimulated emission of radiation).” Surg. Forum, 14: 143-5(1963). (1963).

[20] P. E. McGuff, R. A. Deterling, Jr, L. S. Gottlieb, H. D. Fahimi, D. Bushnell, and F. Roeber, “Laser treatment of experimental malignant tumors.” Can. Med. Ass. J., 91: 1089-95 (Nov. 21, 1964). (1964).

[21] H. M. Smith and A. F. Turner, “Vacuum deposited thin films using a ruby laser,” Appl. Opt. **4**, 147–148 (1965).

[22] A. J. DeMaria, D. A. Stetser, and H. Heynau, “Self mode-locking of lasers with saturable absorbers,” Applied Physics Letters **8**, 174–176 (1966).

[23] R. L. Fork, B. I. Greene, and C. V. Shank, “Generation of optical pulses shorter than 0.1 psec by colliding pulse mode locking,” Applied Physics Letters **38**, 671–672 (1981).

[24] M. Göppert-Mayer, "Über Elementarakte mit zwei Quantensprüngen," Annalen der Physik **401**, 273–294 (1931).

[25] V. Nathan, A. H. Guenther, and S. S. Mitra, "Review of multiphoton absorption in crystalline solids," Journal of the Optical Society of America B **2**, 294–316 (1985).

[26] L. V. Keldysh, "Ionization in the Field of a Strong Electromagnetic Wave," Soviet Physics JETP **20**, 1307–1314 (1965).

[27] E. O. Kane, "Band structure of indium antimonide," Journal of Physics and Chemistry of Solids **1**, 249–261 (1957).

[28] V. E. Gruzdev, "Laser-induced collective ionization in wide band-gap crystalline dielectrics," in *ICONO 2005: Ultrafast Phenomena and Physics of Superintense Laser Fields; Quantum and Atom Optics; Engineering of Quantum Information*, Vol. 6256, edited by H. A. Bachor, A. D. Bandrauk, P. B. Corkum, M. Drescher, M. Fedorov, S. Haroche, S. Kilin, and A. Sergienko, International Society for Optics and Photonics (SPIE, 2006) pp. 18 – 29.

[29] V. E. Gruzdev, "Photoionization rate in wide band-gap crystals," Phys. Rev. B **75**, 205106 (2007).

[30] V. Gruzdev, "Ultrafast laser-induced modifications of energy bands of nonmetal crystals," in *Proc.SPIE*, Vol. 7504 (2009).

[31] S. M. Golin, S. E. Kirkwood, D. D. Klug, D. M. Villeneuve, D. M. Rayner, C. A. T. Herrero, and P. B. Corkum, "Strong field processes inside gallium arsenide," Journal of Physics B: Atomic, Molecular and Optical Physics **47**, 204025 (2014).

[32] L. V. Keldysh, “Concerning the theory of impact ionization in semiconductors,” Soviet Physics JETP **21**, 1135–1144 (1965).

[33] N. Bloembergen, “Laser-induced electric breakdown in solids,” IEEE Journal of Quantum Electronics **10**, 375–386 (1974).

[34] B. C. Stuart, M. D. Feit, A. M. Rubenchik, B. W. Shore, and M. D. Perry, “Laser-Induced Damage in Dielectrics with Nanosecond to Subpicosecond Pulses,” Physical Review Letters **74**, 2248–2251 (1995).

[35] B. C. Stuart, M. D. Feit, S. Herman, A. M. Rubenchik, B. W. Shore, and M. D. Perry, “Nanosecond-to-femtosecond laser-induced breakdown in dielectrics,” Physical Review B **53**, 1749–1761 (1996).

[36] F. Quéré, S. Guizard, and P. Martin, “Time-resolved study of laser-induced breakdown in dielectrics,” Europhysics Letters (EPL) **56**, 138–144 (2001).

[37] M. B. Agranat, S. I. Anisimov, S. I. Ashitkov, A. V. Ovchinnikov, P. S. Kondratenko, D. S. Sitnikov, and V. E. Fortov, “On the mechanism of the absorption of femtosecond laser pulses in the melting and ablation of Si and GaAs,” JETP Letters **83**, 501–504 (2006).

[38] B. Chimier, O. Utéza, N. Sanner, M. Sentis, T. Itina, P. Lassonde, F. Légaré, F. Vidal, and J. C. Kieffer, “Damage and ablation thresholds of fused-silica in femtosecond regime,” Physical Review B **84**, 94104 (2011).

[39] P. Balling and J. Schou, “Femtosecond-laser ablation dynamics of dielectrics: basics and applications for thin films,” Reports on Progress in Physics **76**, 36502 (2013).

[40] B. K. Ridley, “Quantum processes in semiconductors,” (Oxford University Press, 1999) Chap. 6, pp. 235–281, 4th ed.

[41] A. H. Castro Neto, F. Guinea, N. M. R. Peres, K. S. Novoselov, and A. K. Geim, "The electronic properties of graphene," Reviews of Modern Physics **81**, 109–162 (2009).

[42] Q. Bao and K. P. Loh, "Graphene Photonics, Plasmonics, and Broadband Optoelectronic Devices," ACS Nano **6**, 3677–3694 (2012).

[43] H. Wang, Y. Zhao, Y. Xie, X. Ma, and X. Zhang, "Recent progress in synthesis of two-dimensional hexagonal boron nitride," Journal of Semiconductors **38**, 31003 (2017).

[44] J. Xiao, M. Zhao, Y. Wang, and X. Zhang, "Excitons in atomically thin 2D semiconductors and their applications," Nanophotonics **6**, 1309–1328 (2017).

[45] Y. Yoon, K. Ganapathi, and S. Salahuddin, "How Good Can Monolayer MoS_2 Transistors Be?" Nano Letters **11**, 3768–3773 (2011).

[46] Y. Zhang, J. Ye, Y. Matsuhashi, and Y. Iwasa, "Ambipolar MoS_2 Thin Flake Transistors," Nano Letters **12**, 1136–1140 (2012).

[47] H. S. Lee, S.-W. Min, Y.-G. Chang, M. K. Park, T. Nam, H. Kim, J. H. Kim, S. Ryu, and S. Im, "MoS_2 Nanosheet Phototransistors with Thickness-Modulated Optical Energy Gap," Nano Letters **12**, 3695–3700 (2012).

[48] O. Lopez-Sanchez, D. Lembke, M. Kayci, A. Radenovic, and A. Kis, "Ultrasensitive photodetectors based on monolayer MoS_2," Nature Nanotechnology **8**, 497–501 (2013).

[49] J. S. Ross, P. Klement, A. M. Jones, N. J. Ghimire, J. Yan, D. G. Mandrus, T. Taniguchi, K. Watanabe, K. Kitamura, W. Yao, D. H. Cobden, and X. Xu, "Electrically tunable excitonic light-emitting diodes based on monolayer WSe_2 p-n junctions," Nature Nanotechnology **9**, 268–272 (2014).

[50] Y. Woo, W. Hong, S. Y. Yang, H. J. Kim, J.-H. Cha, J. E. Lee, K. J. Lee, T. Kang, and S.-Y. Choi, "Large-Area CVD-Grown $\mathrm{MoS_2}$ Driver Circuit Array for Flexible Organic Light-Emitting Diode Display," Advanced Electronic Materials **4**, 1800251 (2018).

[51] Q. He, Z. Zeng, Z. Yin, H. Li, S. Wu, X. Huang, and H. Zhang, "Fabrication of Flexible $\mathrm{MoS_2}$ Thin-Film Transistor Arrays for Practical Gas-Sensing Applications," Small **8**, 2994–2999 (2012).

[52] F. K. Perkins, A. L. Friedman, E. Cobas, P. M. Campbell, G. G. Jernigan, and B. T. Jonker, "Chemical Vapor Sensing with Monolayer $\mathrm{MoS_2}$," Nano Letters **13**, 668–673 (2013).

[53] K. Wang, J. Wang, J. Fan, M. Lotya, A. O'Neill, D. Fox, Y. Feng, X. Zhang, B. Jiang, Q. Zhao, H. Zhang, J. N. Coleman, L. Zhang, and W. J. Blau, "Ultrafast Saturable Absorption of Two-Dimensional $\mathrm{MoS_2}$ Nanosheets," ACS Nano **7**, 9260–9267 (2013).

[54] X. Wang, Y. Hong, M. Wang, G. Xin, Y. Yue, and J. Zhang, "Mechanical properties of molybdenum diselenide revealed by molecular dynamics simulation and support vector machine," Physical Chemistry Chemical Physics **21**, 9159–9167 (2019).

[55] S. Zhang, N. Dong, N. McEvoy, M. O'Brien, S. Winters, N. C. Berner, C. Yim, Y. Li, X. Zhang, Z. Chen, L. Zhang, G. S. Duesberg, and J. Wang, "Direct Observation of Degenerate Two-Photon Absorption and Its Saturation in $\mathrm{WS_2}$ and $\mathrm{MoS_2}$ Monolayer and Few-Layer Films," ACS Nano **9**, 7142–7150 (2015).

[56] F. Zhou and W. Ji, "Two-photon absorption and subband photodetection in monolayer $\mathrm{MoS_2}$," Optics Letters **42**, 3113–3116 (2017).

[57] F. Zhou and W. Ji, "Giant Three-Photon Absorption in Monolayer MoS_2 and Its Application in Near-Infrared Photodetection," Laser & Photonics Reviews **11**, 1700021 (2017).

[58] M. Currie, J. D. Caldwell, F. J. Bezares, J. Robinson, T. Anderson, H. Chun, and M. Tadjer, "Quantifying pulsed laser induced damage to graphene," Applied Physics Letters **99**, 211909 (2011).

[59] S. Dhar, A. R. Barman, G. X. Ni, X. Wang, X. F. Xu, Y. Zheng, S. Tripathy, Ariando, A. Rusydi, K. P. Loh, M. Rubhausen, A. H. C. Neto, B. Őzyilmaz, and T. Venkatesan, "A new route to graphene layers by selective laser ablation," AIP Advances **1**, 22109 (2011).

[60] A. Roberts, D. Cormode, C. Reynolds, T. Newhouse-Illige, B. J. LeRoy, and A. S. Sandhu, "Response of graphene to femtosecond high-intensity laser irradiation," Applied Physics Letters **99**, 51912 (2011).

[61] F. Wakaya, T. Kurihara, S. Abo, and M. Takai, "Ultra-violet laser processing of graphene on SiO_2/Si," Microelectronic Engineering **110**, 358–360 (2013).

[62] R. Sahin, E. Simsek, and S. Akturk, "Nanoscale patterning of graphene through femtosecond laser ablation," Applied Physics Letters **104**, 53118 (2014).

[63] I. I. Bobrinetskiy, A. V. Emelianov, N. Otero, and P. M. Romero, "Patterned graphene ablation and two-photon functionalization by picosecond laser pulses in ambient conditions," Applied Physics Letters **107**, 43104 (2015).

[64] A. Vasquez, P. Samolis, J. Zeng, and M. Y. Sander, "Micro-structuring, ablation, and defect generation in graphene with femtosecond pulses," OSA Continuum **2**, 2925–2934 (2019).

[65] I. Paradisanos, E. Kymakis, C. Fotakis, G. Kioseoglou, and E. Stratakis, "Intense femtosecond photoexcitation of bulk and monolayer MoS_2," Applied Physics Letters **105**, 41108 (2014).

[66] C. Pan, L. Jiang, J. Sun, Q. Wang, F. Wang, K. Wang, Y. Lu, Y. Wang, L. Qu, and T. Cui, "Ultrafast optical response and ablation mechanisms of molybdenum disulfide under intense femtosecond laser irradiation," Light: Science & Applications **9**, 80 (2020).

[67] J. M. Solomon, S. I. Ahmad, A. Dave, L.-S. Lu, Y.-C. Wu, W.-H. Chang, C.-W. Luo, and T.-H. Her, "Ultrafast multi-shot ablation and defect generation in monolayer transition metal dichalcogenides," AIP Advances **12**, 15217 (2022), licensed under a Creative Commons Attribution (CC BY) license.

[68] S. V. Morozov, K. S. Novoselov, M. I. Katsnelson, F. Schedin, D. C. Elias, J. A. Jaszczak, and A. K. Geim, "Giant Intrinsic Carrier Mobilities in Graphene and Its Bilayer," Physical Review Letters **100**, 16602 (2008).

[69] C. Lee, X. Wei, J. W. Kysar, and J. Hone, "Measurement of the Elastic Properties and Intrinsic Strength of Monolayer Graphene," Science **321**, 385 LP – 388 (2008).

[70] Q. Bao, H. Zhang, Y. Wang, Z. Ni, Y. Yan, Z. X. Shen, K. P. Loh, and D. Y. Tang, "Atomic-Layer Graphene as a Saturable Absorber for Ultrafast Pulsed Lasers," Advanced Functional Materials **19**, 3077–3083 (2009).

[71] A. K. Geim and I. V. Grigorieva, "Van der Waals heterostructures," Nature **499**, 419–425 (2013).

[72] N. Clark, L. Nguyen, M. J. Hamer, F. Schedin, E. A. Lewis, E. Prestat, A. Garner, Y. Cao, M. Zhu, R. Kashtiban, J. Sloan, D. Kepaptsoglou, R. V. Gor-

bachev, and S. J. Haigh, “Scalable patterning of encapsulated black phosphorus,” Nano Letters **18**, 5373–5381 (2018), pMID: 30067903.

[73] H. Kwon, P. J. Jeon, J. S. Kim, T.-Y. Kim, H. Yun, S. W. Lee, T. Lee, and S. Im, “Large scale MoS_2 nanosheet logic circuits integrated by photolithography on glass,” 2D Materials **3**, 044001 (2016).

[74] Z. Cheng, Q. Zhou, C. Wang, Q. Li, C. Wang, and Y. Fang, “Toward intrinsic graphene surfaces: A systematic study on thermal annealing and wet-chemical treatment of SiO_2-supported graphene devices,” Nano Letters **11**, 767–771 (2011).

[75] X. Lu, M. I. B. Utama, J. Zhang, Y. Zhao, and Q. Xiong, “Layer-by-layer thinning of MoS_2 by thermal annealing,” Nanoscale **5**, 8904–8908 (2013).

[76] J. Wu, H. Li, Z. Yin, H. Li, J. Liu, X. Cao, Q. Zhang, and H. Zhang, “Layer thinning and etching of mechanically exfoliated mos_2 nanosheets by thermal annealing in air,” Small **9**, 3314–3319 (2013).

[77] Y. Liu, H. Nan, X. Wu, W. Pan, W. Wang, J. Bai, W. Zhao, L. Sun, X. Wang, and Z. Ni, “Layer-by-layer thinning of mos_2 by plasma,” ACS Nano **7**, 4202–4209 (2013).

[78] P. S. Kollipara, J. Li, and Y. Zheng, “Optical Patterning of Two-Dimensional Materials,” Research **2020**, 6581250 (2020).

[79] R. J. Stöhr, R. Kolesov, K. Xia, and J. Wrachtrup, “All-Optical High-Resolution Nanopatterning and 3D Suspending of Graphene,” ACS Nano **5**, 5141–5150 (2011).

[80] A. Castellanos-Gomez, M. Barkelid, A. M. Goossens, V. E. Calado, H. S. J.

van der Zant, and G. A. Steele, “Laser-Thinning of MoS_2: On Demand Generation of a Single-Layer Semiconductor,” Nano Letters **12**, 3187–3192 (2012).

[81] L. Lin, J. Li, W. Li, M. N. Yogeesh, J. Shi, X. Peng, Y. Liu, B. B. Rajeeva, M. F. Becker, Y. Liu, D. Akinwande, and Y. Zheng, “Optothermoplasmonic Patterning: Optothermoplasmonic Nanolithography for On-Demand Patterning of 2D Materials (Adv. Funct. Mater. 41/2018),” Advanced Functional Materials **28**, 1870299 (2018).

[82] J.-H. Yoo, J. Bin In, J. Bok Park, H. Jeon, and C. P. Grigoropoulos, “Graphene folds by femtosecond laser ablation,” Applied Physics Letters **100**, 233124 (2012).

[83] B. Wetzel, C. Xie, P.-A. Lacourt, J. M. Dudley, and F. Courvoisier, “Femtosecond laser fabrication of micro and nano-disks in single layer graphene using vortex Bessel beams,” Applied Physics Letters **103**, 241111 (2013).

[84] A. Gil-Villalba, C. Xie, R. Salut, L. Furfaro, R. Giust, M. Jacquot, P. A. Lacourt, J. M. Dudley, and F. Courvoisier, “Deviation from threshold model in ultrafast laser ablation of graphene at sub-micron scale,” Applied Physics Letters **107**, 61103 (2015).

[85] G. H. Han, S. J. Chae, E. S. Kim, F. Güneş, I. H. Lee, S. W. Lee, S. Y. Lee, S. C. Lim, H. K. Jeong, M. S. Jeong, and Y. H. Lee, “Laser Thinning for Monolayer Graphene Formation: Heat Sink and Interference Effect,” ACS Nano **5**, 263–268 (2011).

[86] B.-C. Tran-Khac, R. M. White, F. W. DelRio, and K.-H. Chung, “Layer-by-layer thinning of MoS_2 via laser irradiation,” Nanotechnology **30**, 275302 (2019).

[87] D. Yoon, H. Moon, Y.-W. Son, J. S. Choi, B. H. Park, Y. H. Cha, Y. D. Kim, and H. Cheong, "Interference effect on Raman spectrum of graphene on SiO_2/Si," Physical Review B **80**, 125422 (2009).

[88] D.-H. Lien, J. S. Kang, M. Amani, K. Chen, M. Tosun, H.-P. Wang, T. Roy, M. S. Eggleston, M. C. Wu, M. Dubey, S.-C. Lee, J.-H. He, and A. Javey, "Engineering Light Outcoupling in 2D Materials," Nano Letters **15**, 1356–1361 (2015).

[89] Y.-C. Chen, H. Yeh, C.-J. Lee, and W.-H. Chang, "Distributed Bragg Reflectors as Broadband and Large-Area Platforms for Light-Coupling Enhancement in 2D Transition-Metal Dichalcogenides," ACS Applied Materials & Interfaces **10**, 16874–16880 (2018).

[90] M. Velický, W. R. Hendren, G. E. Donnelly, J. M. Katzen, R. M. Bowman, and F. Huang, "Optimising the visibility of graphene and graphene oxide on gold with multilayer heterostructures," Nanotechnology **29**, 275205 (2018).

[91] G. E. Donnelly, M. Velický, W. R. Hendren, R. M. Bowman, and F. Huang, "Achieving extremely high optical contrast of atomically-thin MoS_2," Nanotechnology **31**, 145706 (2020).

[92] J. M. Liu, "Simple technique for measurements of pulsed Gaussian-beam spot sizes," Optics Letters **7**, 196–198 (1982).

[93] *CRC Handbook of Chemistry and Physics*, 102nd ed. (CRC Press, 2021).

[94] X. Zhang, D. Sun, Y. Li, G.-H. Lee, X. Cui, D. Chenet, Y. You, T. F. Heinz, and J. C. Hone, "Measurement of Lateral and Interfacial Thermal Conductivity of Single- and Bilayer MoS_2 and $MoSe_2$ Using Refined Optothermal Raman Technique," ACS Applied Materials & Interfaces **7**, 25923–25929 (2015).

[95] E. Yalon, C. J. McClellan, K. K. H. Smithe, M. Muñoz Rojo, R. L. Xu, S. V. Suryavanshi, A. J. Gabourie, C. M. Neumann, F. Xiong, A. B. Farimani, and E. Pop, "Energy Dissipation in Monolayer MoS_2 Electronics," Nano Letters **17**, 3429–3433 (2017).

[96] P. Yasaei, C. J. Foss, K. Karis, A. Behranginia, A. I. El-Ghandour, A. Fathizadeh, J. Olivares, A. K. Majee, C. D. Foster, F. Khalili-Araghi, Z. Aksamija, and A. Salehi-Khojin, "Interfacial Thermal Transport in Monolayer MoS_2- and Graphene-Based Devices," Advanced Materials Interfaces **4**, 1700334 (2017).

[97] J. B. Park, J.-H. Yoo, and C. P. Grigoropoulos, "Multi-scale graphene patterns on arbitrary substrates via laser-assisted transfer-printing process," Applied Physics Letters **101**, 43110 (2012).

[98] D. Puerto, W. Gawelda, J. Siegel, J. Solis, and J. Bonse, "Erratum: "Plasma formation and structural modification below the visible ablation threshold in fused silica upon femtosecond laser irradiation" [Appl. Phys. Lett. 91, 082902 (2007)]," Applied Physics Letters **92**, 219901 (2008).

[99] P. Rudolph, J. Bonse, J. Krüger, and W. Kautek, "Femtosecond- and nanosecond-pulse laser ablation of bariumalumoborosilicate glass," Applied Physics A **69**, S763–S766 (1999).

[100] T. Dong, M. Sparkes, C. Durkan, and W. O'Neill, "Evaluating femtosecond laser ablation of graphene on SiO_2/Si substrate," Journal of Laser Applications **28**, 22202 (2016).

[101] M. Lenner, A. Kaplan, and R. E. Palmer, "Nanoscopic Coulomb explosion in ultrafast graphite ablation," Applied Physics Letters **90**, 153119 (2007).

[102] A. Kaplan, M. Lenner, and R. E. Palmer, "Emission of ions and charged clusters due to impulsive Coulomb explosion in ultrafast laser ablation of graphite," Physical Review B **76**, 73401 (2007).

[103] A. Kaplan, M. Lenner, C. Huchon, and R. E. Palmer, "Nonlinearity and time-resolved studies of ion emission in ultrafast laser ablation of graphite," Applied Physics A **92**, 999–1004 (2008).

[104] A. Alrasheed, J. M. Gorham, B. C. Tran Khac, F. Alsaffar, F. W. DelRio, K.-H. Chung, and M. R. Amer, "Surface Properties of Laser-Treated Molybdenum Disulfide Nanosheets for Optoelectronic Applications," ACS Applied Materials & Interfaces **10**, 18104–18112 (2018).

[105] C. Tessarek, O. Gridenco, M. Wiesing, J. Müssener, S. Figge, K. Sebald, J. Gutowski, and M. Eickhoff, "Controlled Laser-Thinning of $\mathrm{MoS_2}$ Nanolayers and Transformation to Amorphous $\mathrm{MoO_x}$ for 2D Monolayer Fabrication," ACS Applied Nano Materials (2020).

[106] M. Gertsvolf, H. Jean-Ruel, P. P. Rajeev, D. D. Klug, D. M. Rayner, and P. B. Corkum, "Orientation-Dependent Multiphoton Ionization in Wide Band Gap Crystals," Physical Review Letters **101**, 243001 (2008).

[107] X. Li, W. Rong, L. Jiang, K. Zhang, C. Li, Q. Cao, G. Zhang, and Y. Lu, "Generation and elimination of polarization-dependent ablation of cubic crystals by femtosecond laser radiation," Optics Express **22**, 30170–30176 (2014).

[108] E. S. Kadantsev and P. Hawrylak, "Electronic structure of a single $\mathrm{MoS_2}$ monolayer," Solid State Communications **152**, 909–913 (2012).

[109] J. Gusakova, X. Wang, L. L. Shiau, A. Krivosheeva, V. Shaposhnikov, V. Borisenko, V. Gusakov, and B. K. Tay, "Electronic Properties of Bulk

and Monolayer TMDs: Theoretical Study Within DFT Framework (GVJ-2e Method)," physica status solidi (a) **214**, 1700218 (2017).

[110] A. M. Danishevskii, E. A. Ivchenko, S. F. Kochegarov, and M. I. Stepanova, "Dependence of Two-Photon Absorption Coefficient on Light Polarization in Cubic-Symmetry Semiconductors," JETP Letters **16**, 440–443 (1972).

[111] A. P. Joglekar, H.-h. Liu, E. Meyhöfer, G. Mourou, and A. J. Hunt, "Optics at critical intensity: Applications to nanomorphing," Proceedings of the National Academy of Sciences of the United States of America **101**, 5856 LP – 5861 (2004).

[112] V. V. Temnov, K. Sokolowski-Tinten, P. Zhou, A. El-Khamhawy, and D. von der Linde, "Multiphoton Ionization in Dielectrics: Comparison of Circular and Linear Polarization," Physical Review Letters **97**, 237403 (2006).

[113] P. Tonndorf, R. Schmidt, P. Böttger, X. Zhang, J. Börner, A. Liebig, M. Albrecht, C. Kloc, O. Gordan, D. R. T. Zahn, S. Michaelis de Vasconcellos, and R. Bratschitsch, "Photoluminescence emission and Raman response of monolayer MoS_2, $MoSe_2$, and WSe_2," Optics Express **21**, 4908–4916 (2013).

[114] J. W. Weber, V. E. Calado, and M. C. M. van de Sanden, "Optical constants of graphene measured by spectroscopic ellipsometry," Applied Physics Letters **97**, 91904 (2010).

[115] H.-L. Liu, C.-C. Shen, S.-H. Su, C.-L. Hsu, M.-Y. Li, and L.-J. Li, "Optical properties of monolayer transition metal dichalcogenides probed by spectroscopic ellipsometry," Applied Physics Letters **105**, 201905 (2014).

[116] G. Xing, H. Guo, X. Zhang, T. C. Sum, and C. H. A. Huan, "The Physics of ultrafast saturable absorption in graphene," Optics Express **18**, 4564–4573 (2010).

[117] S. Lu, S. Chen, Z. Zheng, H. Zhang, C. Zhao, and S. Wen, "Saturable absorption in graphene at 800-nm band," in *Proc.SPIE*, Vol. 8555 (2012).

[118] Z. Nie, C. Trovatello, E. A. A. Pogna, S. Dal Conte, P. B. Miranda, E. Kelleher, C. Zhu, I. C. E. Turcu, Y. Xu, K. Liu, G. Cerullo, and F. Wang, "Broadband nonlinear optical response of monolayer $MoSe_2$ under ultrafast excitation," Applied Physics Letters **112**, 31108 (2018).

[119] C. Ming, Z.-Z. Lin, Y. Wang, W. Zhang, J. Zhuang, and X.-J. Ning, "Ion Acceleration by the Coulomb Explosion of Graphene," Japanese Journal of Applied Physics **49**, 45103 (2010).

[120] Y. L. Huang, Y. Chen, W. Zhang, S. Y. Quek, C.-H. Chen, L.-J. Li, W.-T. Hsu, W.-H. Chang, Y. J. Zheng, W. Chen, and A. T. S. Wee, "Bandgap tunability at single-layer molybdenum disulphide grain boundaries," Nature Communications **6**, 6298 (2015).

[121] B. Zhu, X. Chen, and X. Cui, "Exciton Binding Energy of Monolayer WS_2," Scientific Reports **5**, 9218 (2015).

[122] K. Sokolowski-Tinten, J. Bialkowski, and D. von der Linde, "Ultrafast laser-induced order-disorder transitions in semiconductors," Physical Review B **51**, 14186–14198 (1995).

[123] K. Sokolowski-Tinten and D. von der Linde, "Generation of dense electron-hole plasmas in silicon," Physical Review B **61**, 2643–2650 (2000).

[124] W. Jin, P.-C. Yeh, N. Zaki, D. Zhang, J. T. Liou, J. T. Sadowski, A. Barinov, M. Yablonskikh, J. I. Dadap, P. Sutter, I. P. Herman, and R. M. Osgood, "Substrate interactions with suspended and supported monolayer MoS_2: Angle-resolved photoemission spectroscopy," Physical Review B **91**, 121409 (2015).

[125] M. Dendzik, M. Michiardi, C. Sanders, M. Bianchi, J. A. Miwa, S. S. Grønborg, J. V. Lauritsen, A. Bruix, B. Hammer, and P. Hofmann, "Growth and electronic structure of epitaxial single-layer WS_2 on Au(111)," Physical Review B **92**, 245442 (2015).

[126] T.-H. Her, J. M. Solomon, H.-Y. Yao, L.-S. Lu, S. I. Ahmad, W.-C. Chiu, C.-H. Chang, S.-C. Lin, J. Obeid, W.-H. Chang, and C.-W. Luo, "Optical breakdown of monolayer transition-metal dichalcogenides inudced by femtosecond laser," in *RAPID WC3.2* (2021).

[127] N. S. Shcheblanov, M. E. Povarnitsyn, P. N. Terekhin, S. Guizard, and A. Couairon, "Nonlinear photoionization of transparent solids: A nonperturbative theory obeying selection rules," Physical Review A **96**, 63410 (2017).

[128] M. Lenzner, J. Krüger, S. Sartania, Z. Cheng, C. Spielmann, G. Mourou, W. Kautek, and F. Krausz, "Femtosecond Optical Breakdown in Dielectrics," Physical Review Letters **80**, 4076–4079 (1998).

[129] M. Mero, B. R. Clapp, J. C. Jasapara, W. G. Rudolph, D. Ristau, K. Starke, J. Krüger, S. Martin, and W. Kautek, "On the damage behavior of dielectric films when illuminated with multiple femtosecond laser pulses," Optical Engineering **44**, 1–7 (2005).

[130] N. M. Bulgakova, R. Stoian, and A. Rosenfeld, "Laser-induced modification of transparent crystals and glasses," Quantum Electronics **40**, 966–985 (2010).

[131] H. Wang, C. Zhang, and F. Rana, "Ultrafast Dynamics of Defect-Assisted Electron-Hole Recombination in Monolayer MoS_2," Nano Letters **15**, 339–345 (2015).

[132] N. Kumar, S. Najmaei, Q. Cui, F. Ceballos, P. M. Ajayan, J. Lou, and H. Zhao,

"Second harmonic microscopy of monolayer MoS_2," Physical Review B **87**, 161403 (2013).

[133] Z. Sun, M. Lenzner, and W. Rudolph, "Generic incubation law for laser damage and ablation thresholds," Journal of Applied Physics **117**, 73102 (2015).

[134] D. N. Nguyen, L. Emmert, M. Mero, W. G. Rudolph, D. Patel, E. Krous, and C. S. Menoni, "The effect of annealing on the subpicosecond breakdown behavior of hafnia films," in *Proc.SPIE*, Vol. 7132 (2008).

[135] A. Rosenfeld, M. Lorenz, R. Stoian, and D. Ashkenasi, "Ultrashort-laser-pulse damage threshold of transparent materials and the role of incubation," Applied Physics A **69**, S373–S376 (1999).

[136] J. Byskov-Nielsen, J.-M. Savolainen, M. S. Christensen, and P. Balling, "Ultrashort pulse laser ablation of metals: threshold fluence, incubation coefficient and ablation rates," Applied Physics A **101**, 97–101 (2010).

[137] D. Ashkenasi, R. Stoian, and A. Rosenfeld, "Single and multiple ultrashort laser pulse ablation threshold of Al_2O_3 (corundum) at different etch phases," Applied Surface Science **154-155**, 40–46 (2000).

[138] P. Börner, *Ultra-short pulsed laser ablation of diamond*, Ph.D. thesis, University of Freiburg (Albert-Ludwigs-Universität Freiburg) (2019).

[139] D. J. Clark, V. Senthilkumar, C. T. Le, D. L. Weerawarne, B. Shim, J. I. Jang, J. H. Shim, J. Cho, Y. Sim, M.-J. Seong, S. H. Rhim, A. J. Freeman, K.-H. Chung, and Y. S. Kim, "Strong optical nonlinearity of CVD-grown MoS_2 monolayer as probed by wavelength-dependent second-harmonic generation," Physical Review B **90**, 121409 (2014).

[140] Q. Ma, P. M. Odenthal, J. Mann, D. Le, C. S. Wang, Y. Zhu, T. Chen, D. Sun, K. Yamaguchi, T. Tran, M. Wurch, J. L. McKinley, J. Wyrick, K. Magnone, T. F. Heinz, T. S. Rahman, R. Kawakami, and L. Bartels, "Controlled argon beam-induced desulfurization of monolayer molybdenum disulfide," Journal of Physics: Condensed Matter **25**, 252201 (2013).

[141] A. Förster, S. Gemming, G. Seifert, and D. Tománek, "Chemical and Electronic Repair Mechanism of Defects in MoS_2 Monolayers," ACS Nano **11**, 9989–9996 (2017).

[142] S. V. Sivaram, A. T. Hanbicki, M. R. Rosenberger, G. G. Jernigan, H.-J. Chuang, K. M. McCreary, and B. T. Jonker, "Spatially Selective Enhancement of Photoluminescence in MoS_2 by Exciton-Mediated Adsorption and Defect Passivation," ACS Applied Materials & Interfaces **11**, 16147–16155 (2019).

[143] H. M. Oh, G. H. Han, H. Kim, J. J. Bae, M. S. Jeong, and Y. H. Lee, "Photochemical Reaction in Monolayer MoS_2 via Correlated Photoluminescence, Raman Spectroscopy, and Atomic Force Microscopy," ACS Nano **10**, 5230–5236 (2016).

[144] J. Lu, A. Carvalho, X. K. Chan, H. Liu, B. Liu, E. S. Tok, K. P. Loh, A. H. Castro Neto, and C. H. Sow, "Atomic Healing of Defects in Transition Metal Dichalcogenides," Nano Letters **15**, 3524–3532 (2015).

[145] M. A. Khan, M. Erementchouk, J. Hendrickson, and M. N. Leuenberger, "Electronic and optical properties of vacancy defects in single-layer transition metal dichalcogenides," Physical Review B **95**, 245435 (2017).

[146] Y. Wang, C. Cong, C. Qiu, and T. Yu, "Raman Spectroscopy Study of Lattice Vibration and Crystallographic Orientation of Monolayer MoS_2 under Uniaxial Strain," Small **9**, 2857–2861 (2013).

[147] G. Kukucska and J. Koltai, "Theoretical Investigation of Strain and Doping on the Raman Spectra of Monolayer MoS_2," physica status solidi (b) **254**, 1700184 (2017).

[148] L. P. L. Mawlong, K. K. Paul, and P. K. Giri, "Direct Chemical Vapor Deposition Growth of Monolayer MoS_2 on TiO_2 Nanorods and Evidence for Doping-Induced Strong Photoluminescence Enhancement," The Journal of Physical Chemistry C **122**, 15017–15025 (2018).

[149] R. Wang, B. A. Ruzicka, N. Kumar, M. Z. Bellus, H.-Y. Chiu, and H. Zhao, "Ultrafast and spatially resolved studies of charge carriers in atomically thin molybdenum disulfide," Physical Review B **86**, 45406 (2012).

[150] A. Chernikov, C. Ruppert, H. M. Hill, A. F. Rigosi, and T. F. Heinz, "Population inversion and giant bandgap renormalization in atomically thin WS_2 layers," Nature Photonics **9**, 466–470 (2015).

[151] P. D. Cunningham, A. T. Hanbicki, K. M. McCreary, and B. T. Jonker, "Photoinduced Bandgap Renormalization and Exciton Binding Energy Reduction in WS_2," ACS Nano **11**, 12601–12608 (2017).

[152] E. A. A. Pogna, M. Marsili, D. De Fazio, S. Dal Conte, C. Manzoni, D. Sangalli, D. Yoon, A. Lombardo, A. C. Ferrari, A. Marini, G. Cerullo, and D. Prezzi, "Photo-Induced Bandgap Renormalization Governs the Ultrafast Response of Single-Layer MoS_2," ACS Nano **10**, 1182–1188 (2016).

[153] I. L. Shumay and U. Höfer, "Phase transformations of an InSb surface induced by strong femtosecond laser pulses," Physical Review B **53**, 15878–15884 (1996).

[154] D. Puerto, W. Gawelda, J. Siegel, J. Bonse, G. Bachelier, and J. Solis, "Transient reflectivity and transmission changes during plasma formation and abla-

tion in fused silica induced by femtosecond laser pulses," Applied Physics A **92**, 803 (2008).

[155] I. H. Chowdhury, X. Xu, and A. M. Weiner, "Ultrafast double-pulse ablation of fused silica," Applied Physics Letters **86**, 151110 (2005).

[156] V. V. Temnov, K. Sokolowski-Tinten, P. Zhou, and D. von der Linde, "Ultrafast imaging interferometry at femtosecond-laser-excited surfaces," Journal of the Optical Society of America B **23**, 1954–1964 (2006).

[157] S. Amoruso, R. Bruzzese, X. Wang, and J. Xia, "Ultrafast laser ablation of metals with a pair of collinear laser pulses," Applied Physics Letters **93**, 191504 (2008).

[158] V. Piñon, C. Fotakis, G. Nicolas, and D. Anglos, "Double pulse laser-induced breakdown spectroscopy with femtosecond laser pulses," Spectrochimica Acta Part B: Atomic Spectroscopy **63**, 1006–1010 (2008).

[159] Z. Hu, S. Singha, Y. Liu, and R. J. Gordon, "Mechanism for the ablation of Si$\langle 111 \rangle$ with pairs of ultrashort laser pulses," Applied Physics Letters **90**, 131910 (2007).

[160] D. E. Roberts, A. du Plessis, and L. R. Botha, "Femtosecond laser ablation of silver foil with single and double pulses," Applied Surface Science **256**, 1784–1792 (2010).

[161] X. Zhao and Y. C. Shin, "Ablation enhancement of silicon by ultrashort double-pulse laser ablation," Applied Physics Letters **105**, 111907 (2014).

[162] M. Garcia-Lechuga, L. Haahr-Lillevang, J. Siegel, P. Balling, S. Guizard, and J. Solis, "Simultaneous time-space resolved reflectivity and interferometric mea-

surements of dielectrics excited with femtosecond laser pulses," Physical Review B **95**, 214114 (2017).

[163] S. Preuss, M. Späth, Y. Zhang, and M. Stuke, "Time resolved dynamics of subpicosecond laser ablation," Applied Physics Letters **62**, 3049–3051 (1993).

[164] R. Stoian, M. Boyle, A. Thoss, A. Rosenfeld, G. Korn, I. V. Hertel, and E. E. B. Campbell, "Laser ablation of dielectrics with temporally shaped femtosecond pulses," Applied Physics Letters **80**, 353–355 (2002).

[165] K. Zhang, J. Zhang, L. Jiang, X. Li, Y. Liu, B. Li, and Y. Lu, "Ablation enhancement of metal in ultrashort double-pulse experiments," Applied Physics Letters **112**, 261906 (2018).

[166] I.-J. Chen, P.-A. Mante, C.-K. Chang, S.-C. Yang, H.-Y. Chen, Y.-R. Huang, L.-C. Chen, K.-H. Chen, V. Gusev, and C.-K. Sun, "Graphene-to-Substrate Energy Transfer through Out-of-Plane Longitudinal Acoustic Phonons," Nano Letters **14**, 1317–1323 (2014).

[167] Y. Tian, H. Tian, Y. L. Wu, L. L. Zhu, L. Q. Tao, W. Zhang, Y. Shu, D. Xie, Y. Yang, Z. Y. Wei, X. H. Lu, T.-L. Ren, C.-K. Shih, and J. Zhao, "Coherent Generation of Photo-Thermo-Acoustic Wave from Graphene Sheets," Scientific Reports **5**, 10582 (2015).

[168] J. Lu, J. H. Lu, H. Liu, B. Liu, K. X. Chan, J. Lin, W. Chen, K. P. Loh, and C. H. Sow, "Improved Photoelectrical Properties of MoS_2 Films after Laser Micromachining," ACS Nano **8**, 6334–6343 (2014).

[169] B. C. Tran Khac, K.-J. Jeon, S. T. Choi, Y. S. Kim, F. W. DelRio, and K.-H. Chung, "Laser-Induced Particle Adsorption on Atomically Thin MoS_2," ACS Applied Materials & Interfaces **8**, 2974–2984 (2016).

[170] H. Li, J. Wu, X. Huang, G. Lu, J. Yang, X. Lu, Q. Xiong, and H. Zhang, "Rapid and Reliable Thickness Identification of Two-Dimensional Nanosheets Using Optical Microscopy," ACS Nano **7**, 10344–10353 (2013).

[171] J. Hong, Z. Hu, M. Probert, K. Li, D. Lv, X. Yang, L. Gu, N. Mao, Q. Feng, L. Xie, J. Zhang, D. Wu, Z. Zhang, C. Jin, W. Ji, X. Zhang, J. Yuan, and Z. Zhang, "Exploring atomic defects in molybdenum disulphide monolayers," Nature Communications **6**, 6293 (2015).

[172] P. Yeh, A. Yariv, and C.-S. Hong, "Electromagnetic propagation in periodic stratified media. i. general theory∗," J. Opt. Soc. Am. **67**, 423–438 (1977).

[173] B. Jaeggi, B. Neuenschwander, M. Zimmermann, M. Zecherle, and E. W. Boeckler, "Time-optimized laser micro machining by using a new high dynamic and high precision galvo scanner," in *Proc.SPIE*, Vol. 9735 (2016).

[174] J. Aumanen, A. Johansson, J. Koivistoinen, P. Myllyperkiö, and M. Pettersson, "Patterning and tuning of electrical and optical properties of graphene by laser induced two-photon oxidation," Nanoscale **7**, 2851–2855 (2015).

[175] E. Horynová, O. Romanyuk, L. Horák, Z. Remeš, B. Conrad, A. Peter Amalathas, L. Landová, J. Houdková, P. Jiříček, T. Finsterle, and J. Holovský, "Optical characterization of low temperature amorphous $\mathrm{MoO_x}$, $\mathrm{WO_x}$, and $\mathrm{VO_x}$ prepared by pulsed laser deposition," Thin Solid Films **693**, 137690 (2020).

[176] B. H. Christensen and P. Balling, "Modeling ultrashort-pulse laser ablation of dielectric materials," Physical Review B **79**, 155424 (2009).

[177] H. Shi, H. Pan, Y.-W. Zhang, and B. I. Yakobson, "Quasiparticle band structures and optical properties of strained monolayer MoS_2 and WS_2," Physical Review B **87**, 155304 (2013).

[178] T. Cheiwchanchamnangij and W. R. L. Lambrecht, “Quasiparticle band structure calculation of monolayer, bilayer, and bulk MoS_2,” Physical Review B **85**, 205302 (2012).

[179] A. Ramasubramaniam, “Large excitonic effects in monolayers of molybdenum and tungsten dichalcogenides,” Physical Review B **86**, 115409 (2012).

[180] A. Kormányos, G. Burkard, M. Gmitra, J. Fabian, V. Zólyomi, N. D. Drummond, and V. Fal’ko, “k · p theory for two-dimensional transition metal dichalcogenide semiconductors,” 2D Materials **2**, 22001 (2015).

[181] L. Wang, A. Kutana, and B. I. Yakobson, “Many-body and spin-orbit effects on direct-indirect band gap transition of strained monolayer MoS_2 and WS_2,” Annalen der Physik **526**, L7–L12 (2014).

[182] F. A. Rasmussen and K. S. Thygesen, “Computational 2D Materials Database: Electronic Structure of Transition-Metal Dichalcogenides and Oxides,” The Journal of Physical Chemistry C **119**, 13169–13183 (2015).

[183] Y. Jee, M. F. Becker, and R. M. Walser, “Laser-induced damage on single-crystal metal surfaces,” Journal of the Optical Society of America B **5**, 648–659 (1988).

[184] Y. Jee, R. M. Walser, and M. F. Becker, *Laser Induced Damage in Optical Materials: 1986* (ASTM International, West Conshohocken, PA) pp. 593–1988.

[185] P. Mannion, J. Magee, E. Coyne, G. O’Connor, and T. Glynn, “The effect of damage accumulation behaviour on ablation thresholds and damage morphology in ultrafast laser micro-machining of common metals in air,” Applied Surface Science **233**, 275–287 (2004).

[186] S. E. Kirkwood, A. C. van Popta, Y. Y. Tsui, and R. Fedosejevs, "Single and multiple shot near-infrared femtosecond laser pulse ablation thresholds of copper," Applied Physics A **81**, 729–735 (2005).

[187] C. S. R. Nathala, A. Ajami, W. Husinsky, B. Farooq, S. I. Kudryashov, A. Daskalova, I. Bliznakova, and A. Assion, "Ultrashort laser pulse ablation of copper, silicon and gelatin: effect of the pulse duration on the ablation thresholds and the incubation coefficients," Applied Physics A **122**, 107 (2016).

[188] J. Bonse, J. M. Wrobel, J. Krüger, and W. Kautek, "Ultrashort-pulse laser ablation of indium phosphide in air," Applied Physics A **72**, 89–94 (2001).

[189] H. W. Choi, D. F. Farson, J. Bovatsek, A. Arai, and D. Ashkenasi, "Direct-write patterning of indium-tin-oxide film by high pulse repetition frequency femtosecond laser ablation," Appl. Opt. **46**, 5792–5799 (2007).

[190] L. M. Machado, R. E. Samad, W. de Rossi, and N. D. V. Junior, "D-scan measurement of ablation threshold incubation effects for ultrashort laser pulses," Opt. Express **20**, 4114–4123 (2012).

[191] F. Di Niso, C. Gaudiuso, T. Sibillano, F. P. Mezzapesa, A. Ancona, and P. M. Lugarà, "Role of heat accumulation on the incubation effect in multi-shot laser ablation of stainless steel at high repetition rates," Optics Express **22**, 12200–12210 (2014).

[192] D. Ashkenasi, M. Lorenz, R. Stoian, and A. Rosenfeld, "Surface damage threshold and structuring of dielectrics using femtosecond laser pulses: the role of incubation," Applied Surface Science **150**, 101–106 (1999).

[193] L. A. Emmert, M. Mero, and W. Rudolph, "Modeling the effect of native and laser-induced states on the dielectric breakdown of wide band gap optical

materials by multiple subpicosecond laser pulses," Journal of Applied Physics **108**, 43523 (2010).

APPENDIX A: SUPPORTING INFORMATION FOR ULTRAFAST LASER ABLATION, INTRINSIC THRESHOLD, AND NANOPATTERNING OF MONOLAYER MOLYBDENUM DISULFIDE

A.1 Calculation of Internal Field in 2D Materials

When light is incident on 2D materials (2DMs) such as graphene, hexagonal boron nitride, or transition metal dichalcogenides (TMDs), the field inside the 2DM can be enhanced or attenuated due to the etalon effect between the air, 2DM, and substrate. The system can be modeled as an asymmetric etalon composed of air (refractive index $\tilde{n}_0$), 2DM ($\tilde{n}_1$), and a substrate ($\tilde{n}_s$) (see Figures A.1a and A.1b). By considering a normally incident field $\mathcal{E}_{inc}$ and their multiple reflections from two interfaces, the electric field $\mathcal{E}_{2DM}$ at a point x within the 2DM follows the standard Airy formula to be

$$\mathcal{E}_{2DM}(x) = \mathcal{E}_{inc}\tilde{t}_{01}\left(\frac{e^{i\beta_1 x} + \tilde{r}_{1s}e^{i\beta_1(2d_1-x)}}{1 - \tilde{r_{1s}}\tilde{r}_{10}e^{i2\beta_1 d_1}}\right), \tag{A.1}$$

where $\beta_j = 2\pi\tilde{n}_j/\lambda_0$, d_1 is the thickness of the 2DM, $\tilde{t}_{01} = 2/(1+\tilde{n}_1)$ and $\tilde{r}_{10} = (\tilde{n}_1 - 1)/(\tilde{n}_1 + 1)$ are Fresnel coefficients, and $\tilde{r}_{1s}$ is the effective reflection coefficient of the substrate, as seen from the 2DM. The internal intensity quoted in this work is the average $|\mathcal{E}_{2DM}|^2$, calculated from Equation (A.1) by

$$|\mathcal{E}_{2DM}|^2 = \frac{1}{d_1}\int_0^{d_1} \mathcal{E}^*_{2DM}(x)\mathcal{E}_{2DM}(x)\,dx. \tag{A.2}$$

For single-material substrates such as Al_2O_3, cover glass, or a thick Au film, $\tilde{r}_{1s}$ is simply the Fresnel reflection coefficient:

$$\tilde{r}_{1s} = \frac{\tilde{n}_1 - \tilde{n}_s}{\tilde{n}_1 - \tilde{n}_s}. \tag{A.3}$$

For SiO_2/Si substrates, $\tilde{r}_{1s}$ can be calculated analytically using an asymmetric etalon composed of a TMD, SiO_2, and Si, which yields

$$\tilde{r}_{1s} = \frac{(\tilde{n}_2 + \tilde{n}_s)(\tilde{n}_1 - \tilde{n}_2) + (\tilde{n}_1 + \tilde{n}_2)(\tilde{n}_2 - \tilde{n}_s)e^{i2\beta_2 d_2}}{(\tilde{n}_2 + \tilde{n}_s)(\tilde{n}_1 + \tilde{n}_2) + (\tilde{n}_1 + \tilde{n}_2)(\tilde{n}_2 - \tilde{n}_s)e^{i2\beta_2 d_2}}, \tag{A.4}$$

where d_2 is the thickness of the SiO_2 layer and $\tilde{n}_1$, $\tilde{n}_2$, and $\tilde{n}_s$ are the refractive indices of the 2DM, SiO_2, and Si, respectively. $\tilde{r}_{1s}$ as a function of the thickness of the SiO_2 layer is shown in Figure A.1c, from which the intensity enhancement factor ξ based on Equation (A.1) is shown as the blue solid line in Figure A.1d.

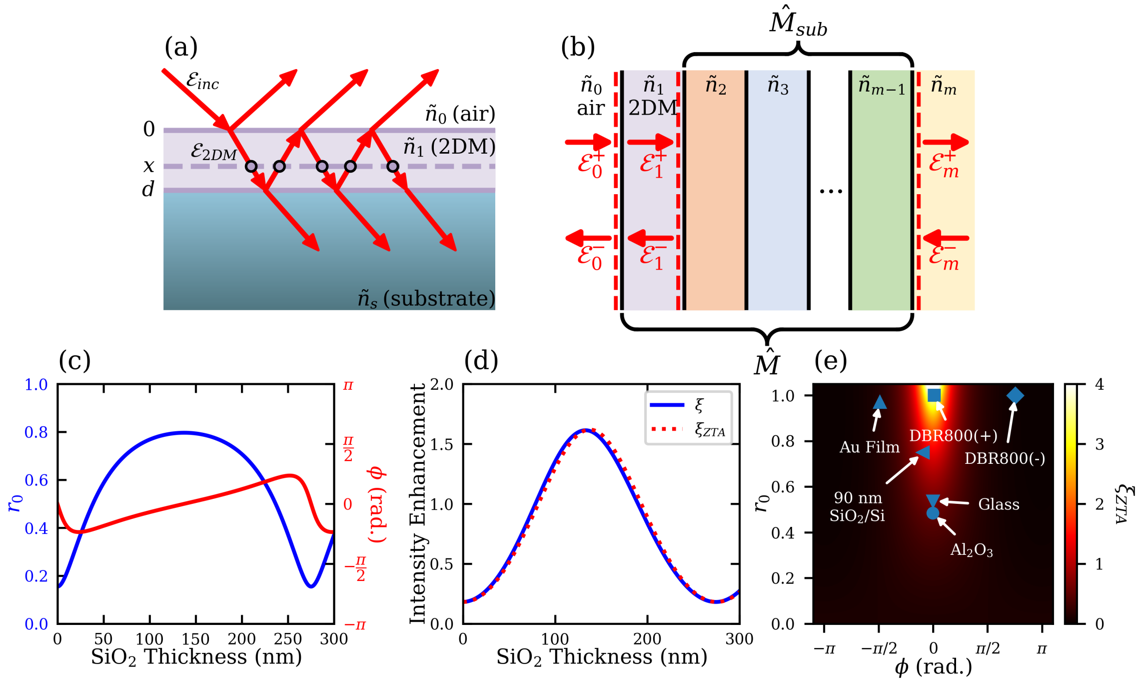

Figure A.1: (a) Diagram for calculating the internal field strength in a 2D material. (b) Diagram for calculating the internal field in a 2D material on a stratified media based on a transfer matrix method. (c) The calculated effective reflection coefficient $\tilde{r}_{1s}$ between a MoS_2 and a SiO_2/Si substrate as a function of SiO_2 thickness, when excited at 800 nm. The reflection coefficient $\tilde{r}_{1s}$ is expressed as $\tilde{r}_{1s} = r_0 e^{i\phi}$ to plot in terms of its amplitude and phase. (d) The intensity enhancement factor for an MoS_2 film supported by an SiO_2/Si substrate. (e) The calculated intensity enhancement factor as a function of the effective reflection coefficient $\tilde{r}_{1s} = r_0 e^{i\phi}$. The substrates tested in Chapter 2 are marked within the plot.

For arbitrary stratified substrates, the effective reflection coefficient $\tilde{r}_{1s}$ can be calculated using a transfer matrix method (TMM). The layer indices are shown in Figure A.1b, where dashed lines indicate the position to which fields are referenced. The substrate is composed of layers 2 through $m-1$, which connects the input and output fields according to

$$\begin{bmatrix} \mathcal{E}_1^+ \\ \mathcal{E}_1^- \end{bmatrix} = \hat{I}_{12}\hat{T}_2\hat{I}_{23}\hat{T}_3 \cdots \hat{T}_{m-1}\hat{I}_{m-1,m} \begin{bmatrix} \mathcal{E}_m^+ \\ \mathcal{E}_m^- \end{bmatrix} = \hat{M}_{sub} \begin{bmatrix} \mathcal{E}_m^+ \\ \mathcal{E}_m^- \end{bmatrix}, \tag{A.5}$$

where

$$\begin{aligned} \hat{I}_{jk} &= \text{Interface Matrix} = \frac{1}{\tilde{t}_{jk}} \begin{bmatrix} 1 & \tilde{r}_{jk} \\ \tilde{r}_{jk} & 1 \end{bmatrix}, \\ \hat{T}_j &= \text{Propagation Matrix} = \begin{bmatrix} e^{-i\beta_j d_j} & 0 \\ 0 & e^{i\beta_j d_j} \end{bmatrix}, \\ \hat{M}_{sub} &= \text{Substrate Matrix} = \begin{bmatrix} M_{sub,00} & M_{sub,01} \\ M_{sub,10} & M_{sub,11} \end{bmatrix}. \end{aligned} \tag{A.6}$$

In the above equation, $\tilde{r}_{jk}$ is the Fresnel reflection coefficient, $\tilde{t}_{jk}$ is the Fresnel transmission coefficient from the j^{th} to k^{th} medium, and d_j is the thickness of the j^{th} material. If the field in the final layer traveling left ($\mathcal{E}_m^-$) is zero, dividing Equation (A.5) by $\mathcal{E}_1^+$ yields the effective reflection and transmission coefficients of the composite substrate given by

$$\begin{aligned} \tilde{r}_{1s} &= \frac{\mathcal{E}_1^-}{\mathcal{E}_1^+} = \frac{M_{sub,10}}{M_{sub,00}}, \\ \tilde{t}_{1s} &= \frac{\mathcal{E}_m^+}{\mathcal{E}_1^+} = \frac{1}{M_{sub,00}}. \end{aligned} \tag{A.7}$$

To prove that $\mathcal{E}_{2DM}^{ZTA}$ is independent of the 2DM for arbitrary stratified substrates, we note that the only dependence on the 2D material's refractive index is at the interface between layers 1 and 2. We then define a $\hat{S}$ matrix according to $\hat{M}_{sub} = \hat{I}_{12}\hat{S}$ and the effective reflection coefficient $\tilde{r}_{1s}$ can easily be shown to be

$$\tilde{r}_{1s} = \frac{S_{10} + \tilde{r}_{12} S_{00}}{S_{00} + \tilde{r}_{12} S_{10}}, \tag{A.8}$$

where Equation (A.8) is rigorous. To prove that $\mathcal{E}_{2DM}^{ZTA}$ is independent of the 2DM, substituting Equation (A.8)) into Equation (2.1) gives

$$\mathcal{E}_{2DM}^{ZTA} = \mathcal{E}_{inc} \frac{2(S_{00} + S_{10})}{(1 + \tilde{n}_2) S_{00} + (1 - \tilde{n}_2) S_{10}}. \tag{A.9}$$

Equation (A.9) offers a general proof that the $\mathcal{E}_{2DM}^{ZTA}$ is independent of the 2D material's refractive index ($\tilde{n}_1$) for any arbitrary substrate when light is at normal incidence.

For the DBR800(+) substrate with N periodic bi-layers (see Figure A.2a; even layers are SiO_2 and odd layers are TiO_2), the $\hat{S}$ matrix at normal incidence can be calculated analytically according to [172]

$$\hat{S} = \begin{bmatrix} S_{00} & S_{01} \\ S_{10} & S_{11} \end{bmatrix} = \begin{bmatrix} AU_{N-1} - U_{N-2} & BU_{N-1} \\ CU_{N-1} & DU_{N-1} - U_{N-2} \end{bmatrix} \tag{A.10}$$

where

$$\begin{aligned}
A &= \frac{1}{\tilde{t}_{23}\tilde{t}_{32}} e^{-i\beta_2 d_2} e^{-i\beta_3 d_3} \left(1 - \tilde{r}_{23}^2 e^{i2\beta_3 d_3}\right), \\
B &= \frac{\tilde{r}_{23}}{\tilde{t}_{23}\tilde{t}_{32}} e^{-\beta_2 d_2} \left(e^{i\beta_3 d_3} - e^{-\beta_3 d_3}\right), \\
C &= \frac{\tilde{r}_{23}}{\tilde{t}_{23}\tilde{t}_{32}} e^{i\beta_2 d_2} \left(e^{-i\beta_3 d_3} - e^{i\beta_3 d_3}\right), \\
D &= \frac{1}{\tilde{t}_{23}\tilde{t}_{32}} e^{i\beta_2 d_2} e^{-i\beta_3 d_3} \left(e^{i2\beta_3 d_3} - \tilde{r}_{23}^2\right), \\
U_N &= \frac{\sin\left\{(N+1)\arccos\left[\frac{1}{2}(A+D)\right]\right\}}{\sqrt{1 - \frac{1}{4}(A+D)^2}}.
\end{aligned} \tag{A.11}$$

The $\mathcal{E}_{2DM}^{ZTA}$ for the DBR800(+) substrate at normal incidence is therefore

$$\mathcal{E}_{2DM}^{ZTA} = \mathcal{E}_{inc} \frac{2(AU_{11} - U_{10} + CU_{11})}{(1+\tilde{n}_2)(AU_{11} - U_{10}) + (1-\tilde{n}_2)CU_{11}} \tag{A.12}$$

where $N = 12$.

A.2 DBR Design and Characterization

As noted in Chapter 2, two custom designed distributed Bragg reflector (DBR) substrates were fabricated: one of which (DBR800(+)) targets maximal intensity enhancement of 4 ($\xi_{ZTA} = 4$, $r_0 = 1$, $\phi = 0$) and the other (DBR800(-)) targets maximal intensity suppression ($\xi_{ZTA} = 0$, $r_0 = 1$, $\phi = \pi$) for 800 nm light. Both DBRs feature multiple quarter-wave stacks of the low index material SiO_2 ($n = 1.45$) and the high index material TiO_2 ($n = 2.08$) for a center wavelength of 800 nm. The design of the DBR800(+) is shown in Figure A.2a, which contains 12 pairs of stacks including SiO_2 as the terminating layer to produce a zero-phase shift upon reflection for total constructive interference within the 2D material. The design of the DBR800(-) is shown in Figure A.2d, which contains 11 pairs of stacks plus an additional TiO_2 layer as the terminating layer to produce a π-phase shift upon reflection for total destructive interference within the 2D material.

To account for manufacturing imperfections in thickness control of the DBR substrates, their reflectivities were measured and fitted to their theoretical design to extract actual layer thicknesses (Figures A.2b and A.2e). These extracted values are then used to calculate the theoretical reflectivity and phases (Figures A.2c and A.2f) and the effective reflection coefficients of the DBR substrates using Equation (A.8), which yield $r_0 = 1.0$, $\phi = 0.011\pi$, and $r_0 = 1.0$, $\phi = 0.76\pi$ for the DBR800(+) and DBR800(-), respectively. Measuring the actual layer thicknesses is important to best model the DBR's performance and to predict the actual field enhancement or attenuation experienced by the 2D material.

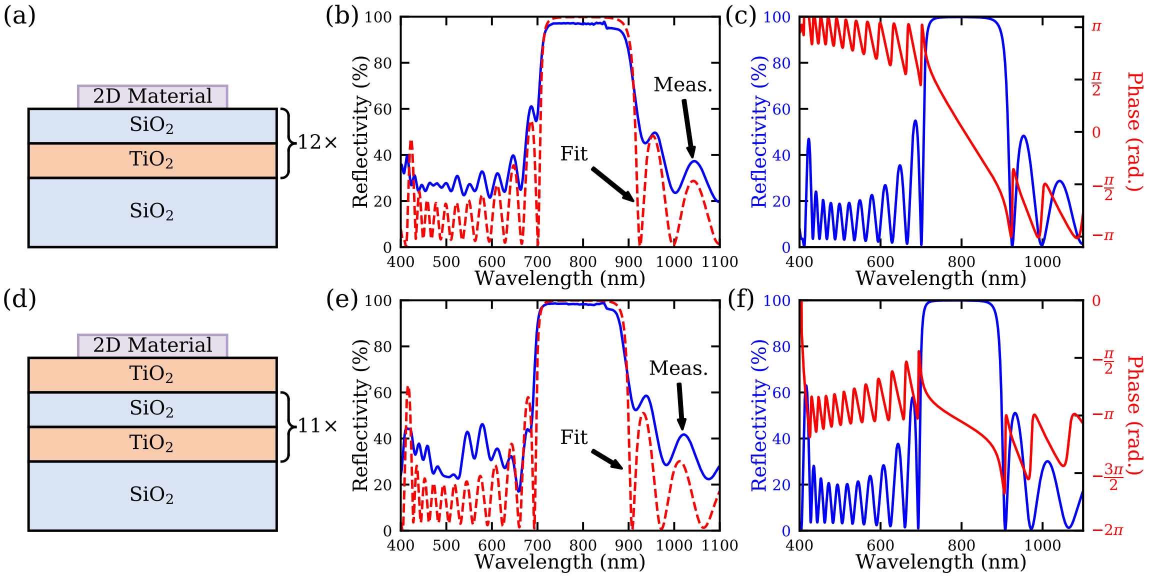

Figure A.2: (a) Design for the DBR800(+) substrate. (b) Measured and fitted reflectivity for the DBR800(+). (c) Calculated reflectivity and phase for the DBR800(+). (d) Design for the DBR800(-) substrate. (e) Measured and fitted reflectivity for the DBR800(-). (f) Calculated reflectivity and phase for the DBR800(-)

As part of the DBR and MoS$_2$ film characterization, AFM scans of the surface were taken. Figure A.3a shows an AFM height map of the edge of the MoS$_2$ film on the DBR800(+) substrate. The height of the monolayer is difficult to resolve due to the surface roughness of the DBR substrate itself. The MoS$_2$ film can be clearly resolved using the phase mapping capability of the AFM instrument as shown in Figure A.3b. A significant phase change is measured when the probe is tapping the DBR surface versus the MoS$_2$ film. This capability allows one to identify when the material properties on the surface has changed. Although the DBR surface was not smooth, the surface roughness had negligible impact on the surface field enhancement as seen in the good agreement between the experimental results and the TMM calculations in Figure 2.3.

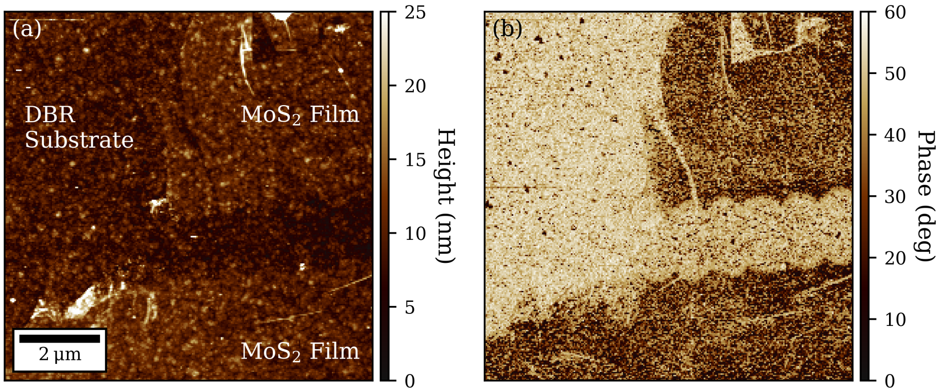

Figure A.3: (a) AFM height map of monolayer MoS2 supported by the DBR800(+) substrate. (b) AFM phase map for the same region as in (a).

A.3 Determination of Focused Laser Spot Size, Threshold Fluence, and Intrinsic Threshold Fluence

For a Gaussian spot, the diameter D of an ablation feature is given by [92]

$$D^2_{u,v} = 2w^2_{u,v}\ln\left(\frac{E}{E_{th}}\right) = 2w^2_{u,v}\ln\left(\frac{F}{F_{th}}\right) \tag{A.13}$$

where w is the laser spot radius at an intensity e^{-2}, E is the pulse energy, E_{th} is the pulse energy at the ablation threshold, F is the peak fluence of the pulse, and F_{th} is the peak fluence at threshold. The subscripts u and v represent the major and minor axes, respectively, of the laser spot profile. The peak fluence for a pulse with a Gaussian spatial and temporal profile is given by

$$F = \frac{2E}{\pi w_u w_v} = \frac{2E}{\pi w^2_{eff}} = 2F_{ave} \tag{A.14}$$

where $w_{eff} = \sqrt{w_u w_v}$ is the effective laser spot radius and F_{ave} is the average laser fluence. Equation (A.13) consists of two expressions for pulses with elliptical spatial profiles; however, the two equations can be combined in terms of the ablation area giving

$$A = \frac{\pi}{2} w_{eff}^2 \ln\left(\frac{E}{E_{th}}\right) = \frac{\pi}{2} w_{eff}^2 \ln\left(\frac{F}{F_{th}}\right), \tag{A.15}$$

where A is the ablation area. This relationship also allows the determination of both the laser spot size and ablation threshold *in situ*. The effective e^{-2}-intensity beam radius determined from the fits were found to be 1.9 µm for the single-shot ablation trials, which agrees with the spot measured by a beam profiler within 5%. Examples of the fits for Equations (A.13) and (A.15) are demonstrated in Figure A.4 for the ablation of monolayer MoS_2 on borosilicate glass.

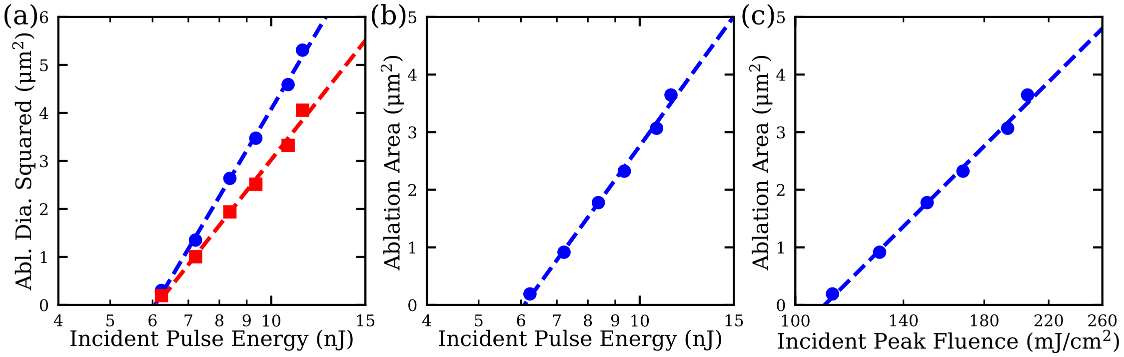

Figure A.4: (a) Ablation diameters for MoS2 on a borosilicate glass cover slip. The major and minor axes are fitted to Equation (A.13)). (b) Ablation area for MoS_2 as a function of pulse energy with its fit to Equation (A.15). (c) Ablation area of MoS_2 as a function of the peak fluence of the incident pulse with its fit to Equation (A.15)).

When determining the damage threshold with the oscillator as shown in Figure 2.4d of the main text, the line width is fitted to Equation (A.13) to extract the threshold. Although the experimental data follows the same logarithmic dependence on the fluence, care needs to be taken when extracting out the spot size. Equations (A.13) and (A.15) were derived under the assumption that lateral carrier diffusion is negligible. For line scans with an oscillator, material modification or breakdown is dominated by thermal mechanisms where lateral carrier diffusion may not be negligible. Additionally, line scans only scan across one axis of the laser spot which was found to be slightly elliptical. Due to these two reasons, the effective laser spot radius

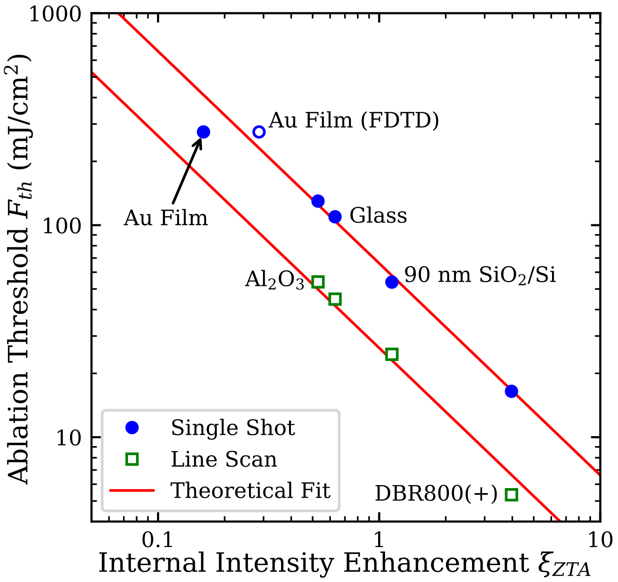

Figure A.5: Determination of the intrinsic ablation threshold F_{th}^{int} for the single shot and oscillator-based line scan experiments. For the single shot experiments, $F_{th}^{int} = 66\,\mathrm{mJ/cm^2}$. For the line scans with an 80 MHz oscillator, the scan rate was set to 0.1 mm/s and $F_{th}^{int} = 26\,\mathrm{mJ/cm^2}$. The theoretical fit is done with Equation (2.4).

was determined using a CCD camera and was found to be 2.0 μm for the oscillator.

After extracting the ablation thresholds with Equations (A.13) and (A.15) for the line scan and single shot experiments, respectively, the intrinsic ablation threshold was determined by fitting the thresholds to Equation (2.4). These fits are shown in Figure A.5.

A.4 Ultrafast Oscillator Laser Patterning

As mentioned in Chapter 2, laser line scans and patterning were limited by the performance of the three-axis stage used in this work. At large scan speeds, mechanical vibrations would skew lines and widen linewidths as shown in Figure A.6. For the UNCC logo in Figure 2.6f, scan rates larger than 3 μm/s would overshoot sharp corners due the size of the logo, skewing the pattern. For the features created here, the speed was ultimately limited by the three-axis translation stage used. Galvo scanners can overcome these imitations and offer improved patterning rates and efficiencies where scan speeds reaching up 25 m/s are possible [173].

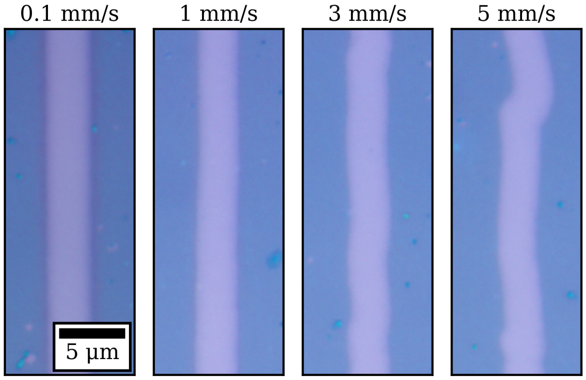

Figure A.6: OM images of lines patterned into a MoS_2 film supported by a 90 nm SiO_2/Si substrate. The fluence was set at 46 mJ/cm^2. The scan rates are 0.1, 1, 3, and 5 mm/s from left to right. All images are set to the same scale.

Ideally, ultrafast laser patterning of 2DMs would be conducted using oscillators due to their small form-factor and reduced cost compared to amplifiers. Fiber oscillators are especially attractive due to their superior robustness, stability, and overall ease-of-use versus their free-space counterparts. To that end, we designed the DBR800(+) substrate in order to reduce the ablation threshold of 2DMs as low as possible such that laser patterning with a commercial off-the-shelf fiber oscillator would be possible. For monolayer MoS_2 on the DBR800(+) substrate, single shot ablation was obtainable with 1 nJ pulse energies and laser patterning with a scan rate of 0.1 mm/s can be done with pulse energies as low as 0.37 nJ when using a 10× objective. The UNCC logo in Figure 2.6f in the main text was patterned with a pulse energy of 65 pJ when the pulses were focused down with a 50× objective. All-fiber, ultrafast oscillators such as erbium-doped oscillators operating at 780 nm or yitterbium-doped oscillators operating at 1030 nm typically only produce pulses that reach up to a couple of nJ. With the DBR800(+) substrate, laser patterning with these types of systems is possible. Additionally, with recent progress made in the synthesis of wafer-scale, highly-oriented MoS_2 films, this example further demonstrates the potential for rapid production of MoS_2-based devices using ultrafast laser patterning [15]. Experimentally, a high-power Ti:S oscillator (Spectra-Physics Tsunami) capable of producing 10 nJ pulses at the sample was used for patterning purposes. These larger pulse energies were needed to pattern MoS_2 films supported by the Al_2O_3 and glass substrates.

A.5 Ultrafast Laser-Induced Oxidation

In ultrafast laser patterning, the incident fluence and scan rate provide a processing matrix, allowing for fine control over the feature types and sizes. In Figure 2.6a, the fluence was set such the material removal occurred for every scan rate. At lower fluences though, the material can be potenitially modified similar to that observed for graphene [64]. Figure A.7 shows optical (Figure A.7a), AFM height (Figure A.7b), and AFM phase (Figure A.7c) images of lines patterned into a MoS_2 film supported by a 90 nm SiO_2/Si substrate using an oscillator with different scan speeds and a fixed peak fluence of 38 mJ/cm^2. Their cross-sectional profiles are shown in Figure A.7d, where the optical contrast is defined as relative pixel difference between the hole and the MoS_2 film, normalized to the MoS_2 film. At low scan rates up to 3 μm/s, removal of material is demonstrated by a high optical contrast and a smooth flat trench in the AFM height profile. At a scan rate of 50 μm/s, the AFM height profile shows an increase in height with a local valley. At a scan rate of 5 mm/s, the valley develops into a plateau that is 2 to 3 nm taller than the monolayer MoS_2 film. This rise in film height is similar to those observed in continuous-wave laser thinning of MoS_2, where an increase in film height of greater than 4 nm was measured due to the formation of an amorphous MoO_x suboxide [105, 143]. Additionally, Raman and photoluminescence measurements show a strong decrease in the MoS_2 peaks, providing further evidence that the material has been oxidized [105, 143]. At very low and very high scan speeds, AFM height and phase profiles are identical, whereas the AFM profiles deviate by various degrees for intermediate scan speeds. Similar AFM scans were taken for lines patterned in the DBR800(+) substrate; however, the DBR was found to have a high surface roughness which prevented accurate measurement of the MoS_2 film height after patterning (Figure A.3). The AFM phase mapping was able to resolve the location of the patterned lines but to a lesser extent when compared to the results in Figure A.7.

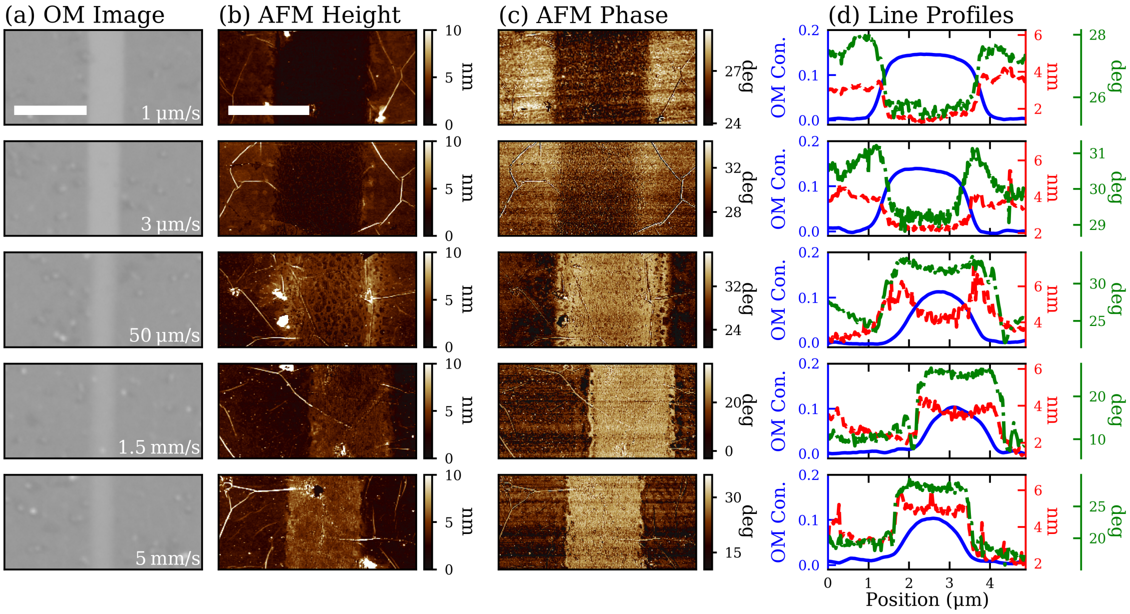

Figure A.7: (a) OM images of lines patterned into a MoS_2 film on a 90 nm SiO_2/Si. The scale bar is 5 μm. (b) Corresponding AFM height images. The scale bar is 2 μm. (c) Corresponding AFM phase images. (d) OM contrast (blue solid), AFM height (red dashed), and AFM phase (green dash-dotted) cross-sections of corresponding OM, AFM height, and AFM phase images, respectively. The scale bars for the AFM height (red) are all set for a range of 5 nm. The peak fluence for these line scans was 38 mJ/cm^2.

Since the optical contrast of the lines change depending on how the material has been altered, the optical contrast can be used as an indicator whether material has been removed or oxidized, or if the material is in transition between those two states. For practical applications, calibrating the OM contrast can remove the need for time-consuming AFM measurements. Figure A.8 shows how both the line width and optical contrast scale with scan speed and which regions correspond to hole formation, modification, or oxidation. As the scan rate increases, the line linewidth slowly decreases before leveling off for both substrates. The linewidth decreases since each spot on the film effectively sees a lower number of pulses and total deposited energy, which reduces the produced linewidth. For the 90 nm SiO_2/Si substrate in Figure

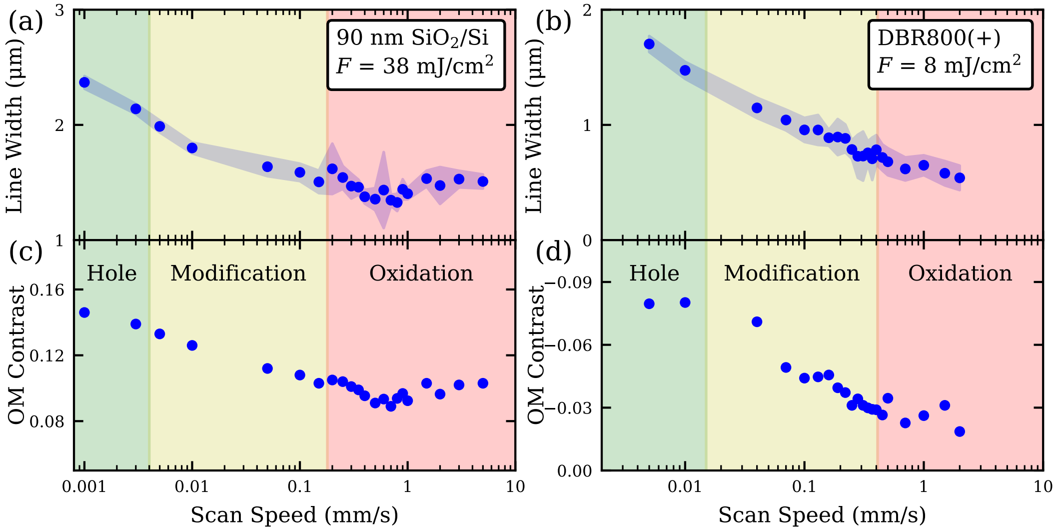

Figure A.8: Measured linewidth with varying scan rate for MoS_2 on (a) 90 nm SiO_2/Si and (b) DBR800(+). Measured OM contrast with varying scan rate for MoS_2 on (c) 90 nm and (d) DBR800(+).

A.8c, the OM contrast also decreases with increasing scan rate. Similar results are also obtained for the DBR800(+) in Figure A.8d. The OM contrast here is negative since the hole in the film has a lower pixel value than the MoS_2 film (see Figure 2.2a), but the results are qualitatively similar.

When patterning with an oscillator, material breakdown can be dominated by either electronic or thermal mechanism depending upon the incident fluence. For the latter case, as energy is deposited into the MoS_2 film, the lattice heats up which can result in several chemical processes such as oxidation, melting and evaporation, or sublimation. For the 90 nm SiO_2/Si substrate at scan rates less than 4 µm/s, enough energy is deposited to remove the MoS_2 film where material removal is thought to occur by sublimation, but this mechanism has yet to be confirmed [65, 80, 168]. At scan rates between 4 µm/s to 200 µm/s, the material is modified and can consist of some material removal and oxidation, whereas uniform oxidation occurs for scan rates greater than 200 µm/s. The oxidation observed here is noticeably different than those presented in literature. In CW experiments where an increase in film height was observed, the feature height was not uniform or contained sharp peaks [105, 143]. In lasing thinning experiments, the oxide forms as loose, amorphous particles scattered across the surface of the MoS_2 film [86, 104, 169]. Similar to graphene, the uniform oxidation obtained with ultrafast pulses illustrates the ability to tune the optical and electrical properties of MoS_2 [174]. With both graphene and MoS_2, oxidation results in an increase of band gap, where the band gap shifts to 3.59 eV for MoS_2 [105, 175]. The increase in band gap changes the excitation process from two-photon absorption to three-photon absorption which is less efficient than the former. As a result, once the oxide forms, it will be more robust to intense optical excitation than the pristine MoS_2 film, requiring either a higher fluence or slower scan rate to deposit enough energy to remove the material.

A.6 Optical Contrast Measurements

As previously mentioned, when the MoS_2 film is oxidized, there is a visible change in contrast which can be used to identify the material without AFM measurements. The optical contrast used in this work is defined by

$$\text{OM Contrast} = \frac{C - C_{film}}{C_{film}} \tag{A.16}$$

where C is the value of the pixel of interest and C_{film} is the pixel value of the MoS_2 film. In order to measure the contrast, the image had to be converted to a grayscale image or into its individual red, green, and blue (RGB) color channels as shown in Figure A.9a. Since each software has its own algorithm to convert a color image to grayscale, the grayscale images presented here were created by simply averaging the pixel values of the RGB channels. Line profiles of the pixel values as shown in Figure A.9b are then taken and substituted in Equation (A.16) to generate the contrast profile. The optical contrast plotted in Figure A.9c represents the minimum value in the contrast profile. The contrast profiles presented Figure A.7d were based on the grayscale images.

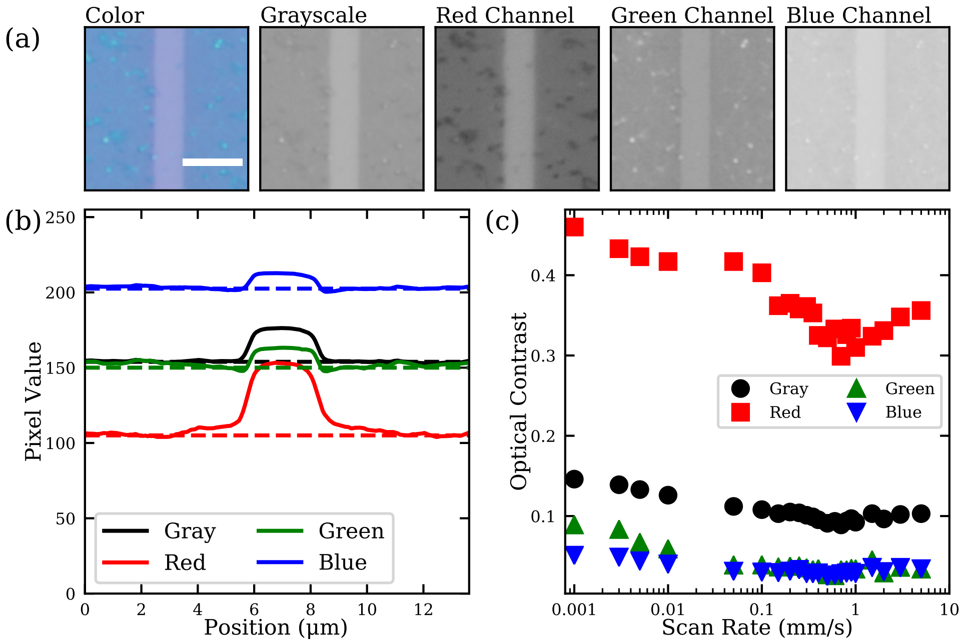

Figure A.9: (a) Example OM image and its RGB channels of a line patterned into an MoS_2 film on a 90 nm SiO_2/Si substrate. (b) Pixel cross-section of the above component images. The dashed line represents C_{film}. (c) Measured optical contrast based on the component images.

APPENDIX B: SUPPORTING INFORMATION FOR FEMTOSECOND LASER-INDUCED BREAKDOWN AND THE ROLE OF AVALANCHE IONIZATION IN MOLYBDENUM DISULFIDE

B.1 Experimental Setup for One-Photon Absorption Measurements

When modeling the ablation of materials, a critieria has to be set that marks the onset of ablation. The two most common criteria are a critical electron density or a critical energy density, both of which are closely related [39]. The critical electron density is commonly adopted since much research shows that the response of a material changes for high population inversions. As such, if a sufficient number of valence electrons, which are responsible for bonds within a solid, are excited, the lattice will become unstable and breakdown. Determining the critical carrier density for ablation though is challenging. Many have adopted the plasma criteria which says says that ablation occurs when plasma frequency ω_p due to excited carriers equals the laser frequency ω given by

$$\omega_p^2 = \frac{Ne^2}{m_0 \epsilon_0}. \tag{B.1}$$

The rationale for this plasma critical carrier density follows from the fact absorption will dramatically increase once the plasma frequency matches the laser frequency. As a result, any small increase in pulse energy will be entirely deposited into the material and cause ablation. Although the plasma criteria is simple and easy to adopt, the above equation implies the critical carrier density then depends on wavelength and is not a material dependent parameter. This property can be considered unphysical when free carrier absorption is already accounted within the model [176]. As a result many choose a flat percentage of the total electron density as their critical electron density which typically ranges between 2% and 10% [122, 123, 176]. Often times these percentages are based on the plasma criteria for one wavelength and applied to all wavelengths equally. The drawback to this approach is that the modeling results can be strongly dependent on the chosen critical carrier density.

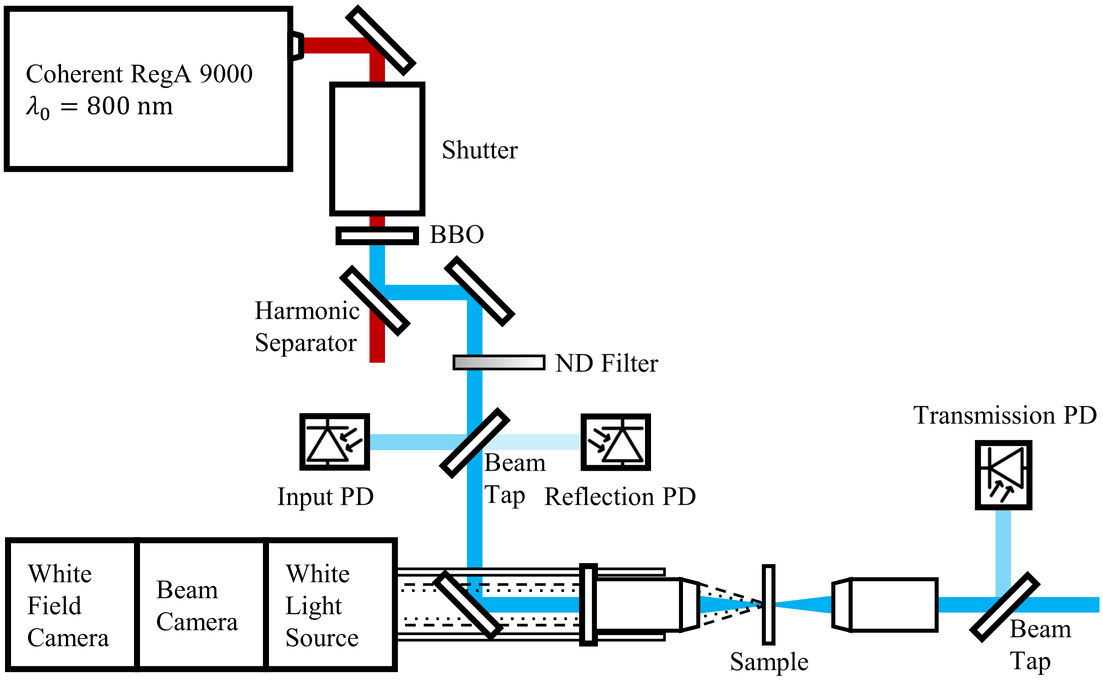

Figure B.1: Schematic for measuring absorption of single-shot ablation at 400 nm.

To avoid using an arbitrary critical carrier density, absorption measurements were conducted to obtain an experimental value. Monolayer MoS_2 offers a unique opportunity to directly measure the critical carrier density since spatial propagation effects can be ignored due to its atomic thickness. As a result, the absorption is assumed to take place at a single point in the monolayer, allowing for direct measure of the absorbed energy density at the surface of the TMD. Literature has shown that MoS_2 exhibits strong 1PA at 400 nm with minimal saturation even at breakdown [7]. Therefore, by directly measuring the absorption and incident fluence, the critical carrier density can be easily calculated assuming every absorbed photon generates one free electron. In order to estimate the critical energy density for ablation, 800 nm pulses were frequency doubled to 400 nm using a Barium borate (BBO) crystal and exposed to monolayer MoS_2. As shown in Figure B.1, both the reflection and transmission were simultaneously recorded for a single pulse exposure in order to obtain an accurate measurement of the absorbed energy density. The absorption was recorded for several fluences near the ablation threshold as shown in Figure 3.7.

B.2 Band Gap Scaling for Avalanche Ionization

For bulk materials, there have been multiple methods to model carrier generation and dynamics during intense excitation. Such approaches include a single rate equation, multiple rate equations, and two-temperature models. As a preliminary approach to understand how the ablation threshold scales with the band gap in the MPI regime, a single rate equation is adopted. As a first order approximation, the total carrier density N can be described by

$$\frac{dN}{dt} = W_{PI}(t) + \gamma_{AI} I(t) N \tag{B.2}$$

where W_{PI} is the photoionization rate as describing both MPI and TI and $\gamma_{AI} I(t) N$ describes the ionization rate due to avalanche. Assuming sufficient seed carriers have been generated and AI is the dominant process, we can approximate the single rate equation as

$$\frac{dN}{dt} \approx \gamma_{AI} I(t) N \tag{B.3}$$

which yields the simple solution

$$N(t) = N_0 \exp\left[\int_{-\infty}^{t} \gamma_{AI} I(t')\, dt'\right]. \tag{B.4}$$

If the "flux-doubling" condition is considered and the input pulse is at the ablation fluence, a critical carrier density N_{crit} will be generated and the term $\alpha I(t)$ can be described in terms of the free carrier conductivity σ_c as

$$\gamma_{AI} I(t) = \frac{\sigma_c |\mathcal{E}(t)|^2}{2U_{crit}} \tag{B.5}$$

where $\mathcal{E}(t)$ is the electric field strength and U_{crit} is the energy that a free electron needs for impact ionization. This critical energy can be expressed as

$$U_{crit} = \left(2 - \frac{m_r}{m_{cb}}\right)\left(E_g + \frac{e^2|\mathcal{E}(t)|^2}{4m_r\omega^2}\right) \tag{B.6}$$

where m_r and m_{cb} are the reduced mass and effective mass of a conduction band electron, respectively, and E_g is the band gap. The coefficient in front accounts for momentum conservation during the impact process [40]. The second term that modifies E_g is the pondermotive energy. Equations (B.5) and (B.6) can be substituted into Equation (B.4) to give

$$N_{crit} = N_0 \exp\left[\frac{\sigma_c}{2(2 - m_r/m_{cb})}\int_{-\infty}^{\infty}\frac{|\mathcal{E}(t)|^2}{E_g + e^2|\mathcal{E}(t)|^2/4m_r\omega^2}\,dt\right]. \tag{B.7}$$

Now, if a Gaussian pulse described by $\mathcal{E}(t) = \mathcal{E}_0 \exp\left(-t^2/2\Delta t^2\right)$ is considered, the previous equation can be expressed as

$$N_{crit} = N_0 \exp\left[\frac{2\sigma_c\gamma^2}{(2 - m_r/m_{cb})}\frac{\mathcal{E}_0^2}{E_g}\int_{-\infty}^{\infty}\frac{\exp\left(t^2/\Delta t^2\right)}{4\gamma^2 + \exp\left(t^2/\Delta t^2\right)}\,dt\right] \tag{B.8}$$

where $\gamma = \omega\sqrt{m_r E_g}/e\mathcal{E}_0$ is the adiabaticity parameter for solids as defined in Equation (1.14). For the fluences near threshold for MoS_2 and WS_2, $\gamma \sim 2$ which suggests seed electrons are generated by MPI. Additionally, we can approximate $4\gamma^2 \gg 1$ which allows the above equation to be approximated as

$$N_{crit} = N_0 \exp\left[\frac{\sigma_c\Delta t\sqrt{\pi}}{2(2 - m_r/m_{cb})}\frac{\mathcal{E}_0^2}{E_g}\right] \tag{B.9}$$

where $\Delta t = \tau/2\sqrt{2\ln 2}$ with τ being the pulse duration defined by the FWHM of the intensity profile. The free carrier conductivity σ_c is given by the Drude model and is

$$\sigma_c = \frac{e^2\Gamma}{m_{cb}\left(\omega^2 + \Gamma^2\right)} \tag{B.10}$$

where Γ is the total electron scattering rate. We can substitute for σ_c in Equation (B.9) to obtain

$$N_{crit} = N_0 \exp\left[\frac{e^2\Gamma\Delta t\sqrt{\pi}}{2(\omega^2+\Gamma^2)(2m_{cb}-m_r)}\frac{\mathcal{E}_0^2}{E_g}\right]. \tag{B.11}$$

For MoS$_2$ and WS$_2$, many band structure calculations show that the ratio of m_{cb}/m_{vb} varies between 0.7 and 1.2 [108, 177–182]. Based on this, it is reasonable to approximate $m_{cb} \approx m_{vb}$. With this approximation, the field at the the ablation threshold is found to be

$$\mathcal{E}_0 = \left[\frac{3\left(\omega^2+\Gamma^2\right)}{e^2\Gamma\Delta t\sqrt{\pi}}\ln\left(\frac{N_{crit}}{N_0}\right)\right]^{1/2}\left(m_{vb}E_g\right)^{1/2}. \tag{B.12}$$

The above relationship demonstrates how the critical carrier density at ablation depends on the electric field strength and band gap when AI dominates. To highlight this relationship, one can write

$$\mathcal{E}_0 \propto \left(m_{vb}E_g\right)^{1/2}. \tag{B.13}$$

Many approximations were made to reach this conclusion and does not represent a complete picture of the carrier dynamics that occur inside the TMDs at large excitation fluences. Further work is being performed to develop a multiple rate equation model to better understand the complete carrier dynamics of these TMDs at high excitation conditions.

B.3 Numerical Modeling of Ablation with a Single Rate Equation

The results of the numerical modeling for the AI coefficient γ_{AI} regarding MoS$_2$ were summarized and reported in Chapter 3.4. The details regarding the the calculations are presented here with all the equations used to describe the carrier generation processes. As reported before, the carrier density N in the conduction band is described by a SRE given by

$$\frac{dN}{dt} = \left(W_{PI}(t) + \gamma_{AI} I(t) N\right) \left(1 - \frac{N}{N_{tot}}\right), \tag{3.4 revisted}$$

where $W_{PI}(t)$ represents the photoionization rate and N_{tot} is the total valence electron density. The internal optical intensity $I(t)$ is described by

$$I(t) = \mathrm{Re}\left[\tilde{n}(t)\right] \xi_{ZTA} I_0(t) \tag{3.6 revisited}$$

where ξ_{ZTA} is the enhancement factor due to the etalon effect as discussed in Chapter 2. The terms $\tilde{n}(t)$ and $I_0(t)$ are given by

$$\tilde{n}(t) = \left[1 + \frac{3\left(N_{tot} - N(t)\right)\chi}{N_{tot} - \left(N_{tot} - N(t)\right)} - \frac{N(t)e^2}{m_{cb}\epsilon_0\omega\left(\omega + i\Gamma\right)}\right]^{1/2} \tag{B.14}$$

$$\chi = \frac{\tilde{n}_1^2 - 1}{\tilde{n}_1^2 + 2} \tag{B.15}$$

$$I_0(t) = \frac{1}{2} c\epsilon_0 \mathcal{E}_0^2 \exp\left(\frac{-t^2}{2\tau_p^2}\right) \tag{B.16}$$

where Γ is the scattering rate for conduction band electrons, $\tilde{n}_1$ is the refractive index of MoS_2 at 800 nm, and τ_p is related to the pulse duration τ_{FWHM} by $\tau_p = \tau_{FWHM}/\left(2\sqrt{2\ln 2}\right)$. Equation (B.14) is based on the Drude model and accounts for the effect of carrier generation on the refractive index of the material. Specifically, the second term represents the Clausius-Mossotti correction and the second term accounts for free carrier absorption due to plasma generation [39]. Equation (3.4) was numerically integrated to solve for the AI coefficient γ_{AI} when the generated carrier density reached N_{crit} as defined by the single-shot absorption measurements in Chapter 3.3. The values used to solve Equation (3.4) are summarized in Table B.1.

Table B.1: Values of the parameters used to evaluate Equation (3.4). The thickness of a monolayer MoS_2 flake is 0.65 nm.

Parameter	**Value**
λ	800 nm
τ_{FWHM}	170 fs
F_{th}	$69.2\,\mathrm{mJ/cm^2}$
$\tilde{n}_1$	5.05
ξ_{ZTA}	1.14
σ_2	$8.03 \times 10^{25}\,\mathrm{cm\,fs/J^2}$
E_g	$2.4\,\mathrm{eV}$
m_{cb}	$0.43m_e$
m_{vb}	$0.43m_e$
N_{crit}	$4.20 \times 10^{15}\,\mathrm{cm^2}$
N_{tot}	$1.39 \times 10^{16}\,\mathrm{cm^2}$

As mentioned in Chapter 3.4, the PI rate was modeled following four different methods: 2PA based on experimental coefficients (Ji's Exp.) [56], the Keldysh expression for PI of bulk materials (3D KLD) [26], the Keldysh expression for PI of 2D materials (2D KLD) [126], and the Keldysh expression for 2D materials considering quantum interference (2D KLD wQI) [126]. The AI coefficient for each of the PI rates were found to be 20.4, 33.2, 29.2, and 27.8 $\mathrm{cm^2/J}$, respectively. The predicted carrier densities for all four PI rates are summarized in Figure B.2. Moreover, given the AI coefficient and the spot size of the pulse, a spatial-temporal carrier map can be calculated to predict the ablation area for any incident fluence. Figure B.3a shows the measured ablation area for MoS_2 from Figure 3.1 along with the fit from Equation (3.1). The SRE model from Equation (3.4) was used to predict the ablation area for fluences above F_{th} based on Ji's Exp. as shown with the dotted green line in Figure B.3a given a laser spot radius of 2.26 μm. The SRE model perfectly agrees with the fit and matches the experimental data, validating that the SRE model is self-consistent with the experimental results.

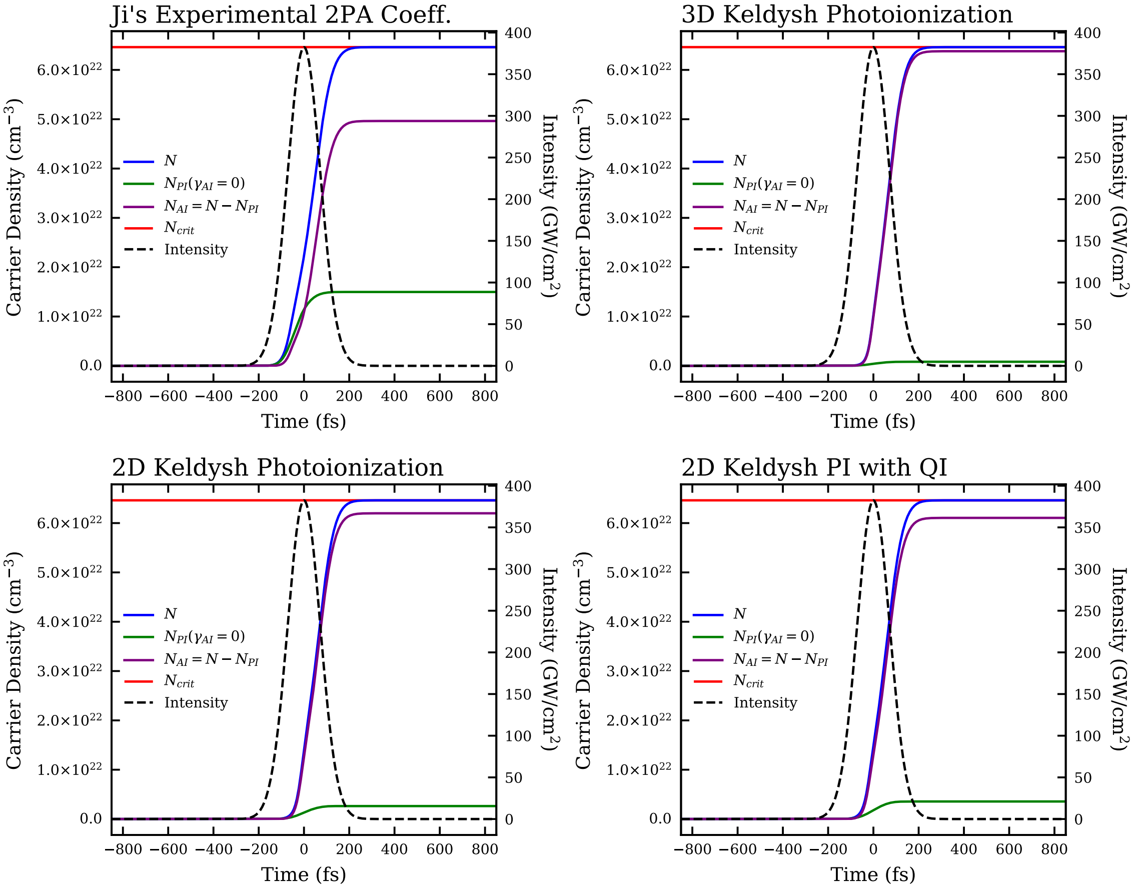

Ji's Experimental 2PA Coeff.

3D Keldysh Photoionization

2D Keldysh Photoionization

2D Keldysh PI with QI

Figure B.2: Predicted carrier densities for monolayer MoS_2 when excited by a 170 fs pulse at the ablation threshold. The photoionization rate was modeled following four different methods.

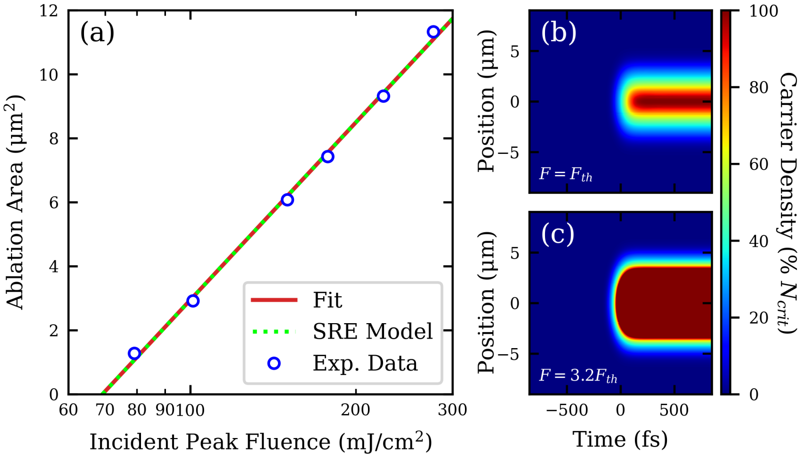

Figure B.3: (a) Measured ablation area as a function of the incident peak fluence for monolayer MoS_2. The red line represents the fit using Equation (3.1). The dotted green line represents the predicted ablation are based on the SRE in Equation (3.4). (b) Spatial-temporal carrier map for MoS_2 excited by a pulse with a fluence of F_{th}. (c) Spatial-temporal carrier map for MoS_2 excited by a pulse with a fluence of $3.2F_{th}$. The laser spot radius was 2.26 μm. The AI coefficient and the PI rate was based on Ji's Exp.

APPENDIX C: SUPPORTING INFORMATION FOR ULTRAFAST MULTI-SHOT ABLATION AND DEFECT GENERATION IN MONOLAYER MOLYBDENUM DISULFIDE

C.1 Modeling Multi-Shot Ablation

Multiple models have been developed to quantify and predict the incubation behavior of materials exposed to multiple pulses. One of the first, and most commonly used models was developed by Jee *et al.* [183, 184]. This phenomenological model is a simple power law given by

$$F_{th}(N) = F_{th}(1)N^{S-1} \tag{C.1}$$

where N is the number of pulses, S is known as the incubation coefficient, and $F_{th}(N)$ and $F_{th}(1)$ are the N-shot and single-shot ablation thresholds, respectively. This model has been used to fit results from several multi-shot studies on a wide range materials including metals, semiconductors, and dielectrics [136, 185–190]. The important parameter here is the incubation coefficient S which describes the degree of incubation. For $S = 1$, there are no incubation effects and the threshold is independent of the number of pulses. For $S < 1$, the material is susceptible to incubation effects where smaller S values indicate a higher likely hood a material will develop defects after exposure to each subsequent pulse.

The measured ablation thresholds for MoS_2 and WS_2 from Chapter 4 were fitted to Equation (C.1) and presented in Figure C.1. Multishot results for other materials found in literature were also included with their fits to Equation (C.1) for comparitive purposes [83, 137, 186–188]. The ablation thresholds were all normalized to the single shot ablation threshold as determined from their fits which allows for easy comparison of their slopes. The slopes for the 2D materials are shallower compared to all of the other included bulk materials which means they are more robust against incubation

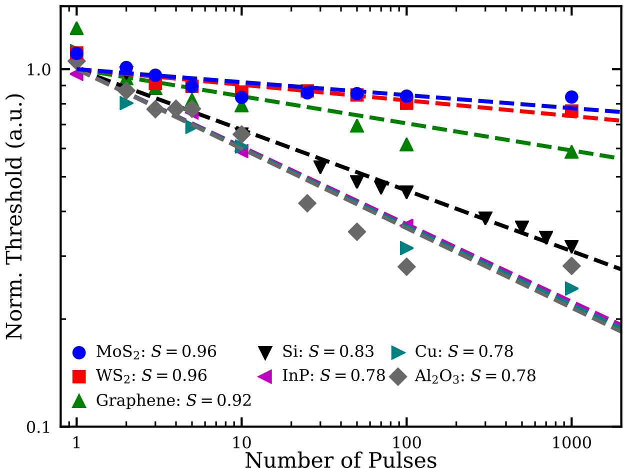

Figure C.1: Normalized multi-shot ablation thresholds for multiple materials found in literature [83, 137, 186–188]. The single-shot threshold is normalized to 1 based on the fit to Equation (C.1).

effects, which agree with the results presented in Table 4.1.

Although Equation (C.1) is simple and commonly used in literature, it is unable to describe the saturation in the threshold observed for the 2D materials here and several bulk materials in literature such as Al_2O_3 and SiO_2. To account for saturation effects, multiple groups have proposed modifications or new models. Di Niso *et al.* suggested adding $F_{th}(\infty)$ to Equation (C.1) to account for saturation effects [191]. Ashkenasi *et al.* proposed a new empirical model given by

$$F_{th}(N) = F_{th}(\infty) + [F_{th}(1) - F_{th}(\infty)]\, e^{-k(N-1)} \tag{C.2}$$

where k describes the strength of defect accumulation [192]. While this model can successfully fit the the multi-shot ablation thresholds of several materials that exhibit saturation, it lacks any physical backing and fails to describe materials that exhibit multiple different decay rates. Other models based on rigorous rate equations have also been proposed and successfully used to model multi-shot ablation [129, 193]. Although these models provide dynamic rate equations that account for both native and laser-induced defect states, extensive knowledge of the material's defect characteristics (such as lifetimes, densities, energy levels, and ionization cross-sections) and nonlinear optical properties (such as multi-photon and avalanche ionization rates) is required to accurately apply the model, many of which are currently not known for 2D materials. Alternatively, a phenomenological model was introduced by Sun *et al.* where they consider two major processes of incubation: laser-induced change of both the absorption coefficient α and critical energy density G [133]. Even though this model is still empirical in nature, it does provide some physical insight into the incubation process where the laser-induced change in absorption and critical energy density are used as fitting parameters. The model can also account for multiple decay mechanisms seen in multi-shot such as for WS_2 and graphene. For this reason, this model is used to describe the multi-shot data of 2D materials in this work.

C.2 Above Threshold Damage

While Chapter 4.3 provides evidence and discussion regarding sub-threshold damage, similar characterization including HR-TEM and SH spectroscopy was also conducted for above threshold excitation that result in holes in the MoS_2 film. Figure C.4 shows a SH line scan and corresponding polar profile of a hole created in a MoS_2 film by a single pulse with $F = 2.0F_{th}$. The SH intensity for the line scan does not go to zero since the probe pulse spot size is larger than the hole size. Nevertheless, the SH polar profile shows strong depolarization effects similar to those seen in amorphous silicon [8]. This depolarization is due to the strong crystalline disorder observed at the edges of the hole as shown in the HR-TEM images in Figure C.3. Ablation experiments on suspended films revealed that the MoS_2 readily folds once a hole is created when compared to supported MoS_2, though nanofolds are still present as shown in Figure 3.4. Nevertheless, several interesting properties are observed excluding the macroscopic folds. Higher magnification images reveal nano-voids, nano-folds, and amorphous MoS_2 at the edges of the hole, all of which can strongly contribute to

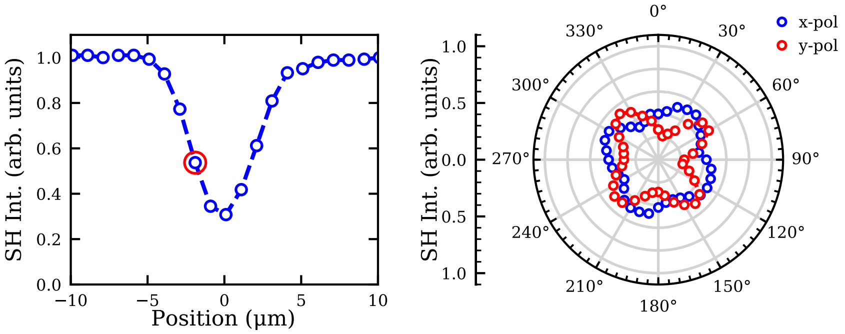

Figure C.2: (left) SH line scan across a hole in a MoS_2 film caused by a single pulse with $F = 2.0F_{th}(1)$. (right) the SH polar profile recorded at the spot marked with a the red circle in the line scan. The MoS_2 film was supported by a borosilicate glass substrate.

the depolarization of the SH profile. Similarly, amorphous MoS_2 was also verified by TEM images in CW laser thinning studies where nearly the entire rim of the hole was amorphous [86]. Their result is not surprising given the thermal nature of breakdown due to CW excitation. The presence of amorphous MoS_2 due to ultrafast excitation supports the possibility that MoS_2 can undergo ultrafast melting in addition to sublimation as claimed by Paradisanos *et al.* [65]. Additional HR-TEM images are also shown in Figure C.4 at the ablation threshold for MoS_2. These images reveal nano-voids along with strong disordering around these voids, similar to the results in Figure 4.4 but with a much higher density. These defects are expected to have a much stronger effect on the SH, PL, and Raman intensities than those observed in Figure 4.4.

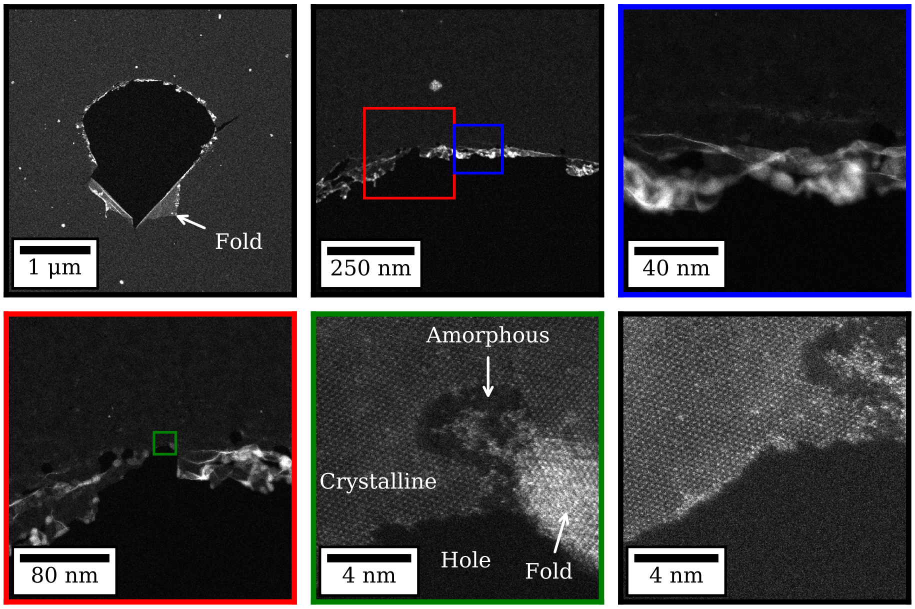

Figure C.3: HR-TEM images of a hole created in a suspended monolayer MoS_2 film by a single ultrafast pulse with $F = 2.0F_{th}(1)$.

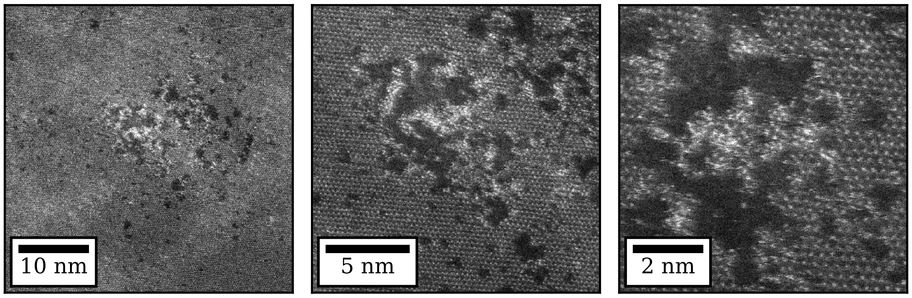

Figure C.4: HR-TEM images of a MoS_2 film excited by single pulse with $F = F_{th}(1)$.

APPENDIX D: GENERAL EXPERIMENTAL SETUP

Figure D.1 shows a schematic of the general experimental setup for femtosecond ablation of 2D materials. The Coherent RegA 9000 is a titanium:sapphire (Ti:S) regenerative amplifier capable of producing pulse widths around 160∼170 fs at a center wavelength of 800 nm. Typically, the RegA 9000 operates at a repetition rate of 100-250 kHz, producing pulse energies of 3-4 μJ. In order to select a single pulse for experiments, the RegA 9000 was externally triggered to a repetition rate of about 307 Hz. At this repetition rate, some mechanical shutters are quick enough to select out a single pulse. The shutter used for this purpose was a NM Laser Products, Inc. LS200NOIR high power, laser shutter which is capable of selecting a single pulse from a 1 kHz pulse train. In order to take full advantage of the numerical aperture of the objective to focus the pulse, a telescope was added after the shutter to expand the beam to the size of the input aperture of the objective. A continuous, variable neutral density (ND) filter was used to adjust the energy of the pulse which was measured using a beam tap and a calibrated photodiode. For polarization sensitive experiments, a half-wave plate (HWP) or quarter-wave plate (QWP) was placed before the objective to control the incident polarization of the pulse. During laser patterning experiments, the amplifier was replaced by a Spectra-Physics Tsunami which is a Ti:S oscillator that only produces pulse energies as large as 10 nJ but at a repetition rate of about 80 MHz.

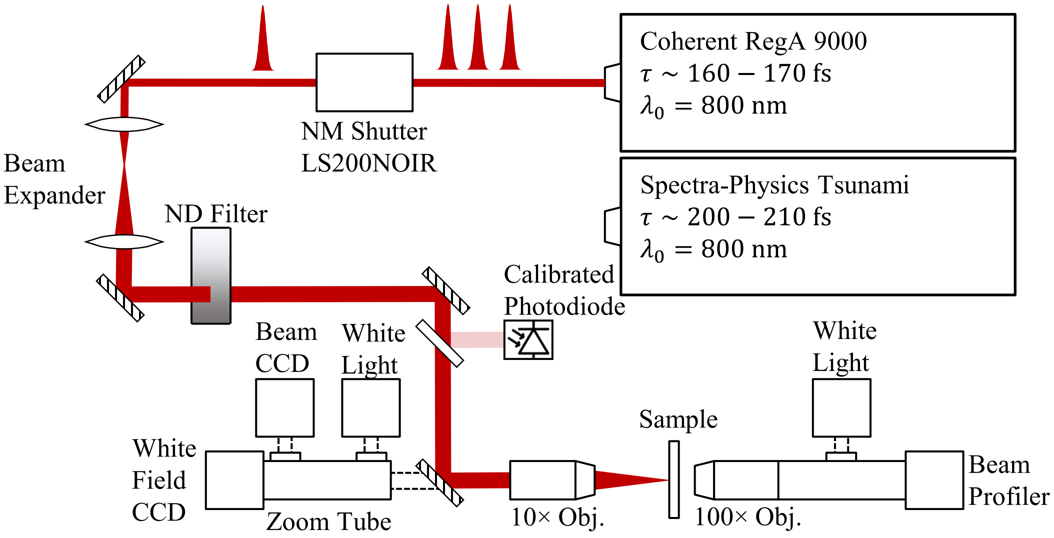

Figure D.1: Schematic of the experimental setup for femtosecond laser ablation.